UNIVERSITY
OF OSLO

Sigurd Eide

RIMFAX-modeling for Martian subsurface exploration

Ground-penetrating radar studies for the Mars 2020 Perseverance rover mission, during exploration of Jezero Crater Floor

Thesis submitted for the degree of Philosophiae Doctor

Department of Technology Systems
Faculty of Mathematics and Natural Sciences

2023

© Sigurd Eide, 2023

Series of dissertations submitted to the
Faculty of Mathematics and Natural Sciences, University of Oslo
No. 2612

ISSN 1501-7710

All rights reserved. No part of this publication may be
reproduced or transmitted, in any form or by any means, without permission.

Cover: UiO.
Print production: Graphic Center, University of Oslo.

Preface

It has been a truly exciting time working with novel instrumentation on a planetary mission to Mars. RIMFAX was the very first ground-penetrating radar to be operating form the Martian surface, sounding the shallow subsurface and opening up a new window into the planet's past and present-day environmental conditions and geological processes. This thesis was timely placed, spanning from pre-landing assessments to first results, and is documenting crucial periods of instrument acquisition and initial analyses. It covers periods of both anticipation and frantic work, as well as realizations and surprises. With no beaten path to analyse the data or even knowing what information it would contain, it has felt like taking part in true frontier exploration. Still, more intriguing discoveries are awaiting to be made as the Perseverance rover continue its journey over new terrain, and from looking at already acquired data with new eyes.

Acknowledgements

There have been many contributions during the course of this thesis. First and foremost, I would like to thank my supervisors Svein-Erik Hamran, Henning Dypvik and Hans E. F. Amundsen. It has been an excellent collaboration through four years and I have appreciated the expert guidance along the way. I would also like to acknowledge and thank all my coauthors for their help and contributions to the papers of this thesis.

It has been an engaging and interesting period as part of the RIMFAX Science Team with highly skilled colleagues from several fields of studies, located at research departments around the world. In addition to the University of Oslo, cooperation has been with the Norwegian Defence Research Establishment; University of California, Los Angeles; NASA's Jet Propulsion Laboratory; University of Arizona; among others. In particular, I would like to thank David Paige and Jessica Ban for hosting me the University of California, Los Angeles in 2021, despite all the difficulties posed by the Covid pandemic. The research stay was financed and facilitated by the Fulbright foundation, and I am grateful of their support. I am also thankful for additional support from Norwegian Research School for Dynamics and Evolution of Earth and Planets (DEEP) at the University of Oslo.

Taking part in the Mars 2020 Science Team has been both an enriching and exciting experience. The team is orchestrated by NASA's Jet Propulsion Laboratory, but with hundreds of additional members from various research institutions around the world. Working with tactical surface operations, staffed as a uplink/downlink payload lead, has really opened my eyes to the complexity of commanding a spacecraft, as well as the devotion and proficiency that is

required by everyone involved. Moreover, participating in the science discussions has been fascinating, starting with selecting the landing site in 2018 and later in 2021 evolving into addressing activities and results on Mars. With grand mission objectives as (i) seeking signs of ancient extraterrestrial life, (ii) returning Martian rock samples to Earth, and (iii) preparing for human activity on Mars, being a part of the Mars 2020 mission has both expanded my horizons and thought me how to approach big endeavours in a rational way.

This thesis was conducted in the period 2018 to 2022 at the University of Oslo, Department of Technology Systems (ITS), and from 2020 in cooperation with Centre for Space Sensors and Systems (CENSSS). Additionally, I have also had the privilege of being connected the Department of Geosciences and the DEEP research school, as well as being enrolled in courses at Simula Research Laboratory and European Space Agency. During the four years long engagement as a Ph.D. research fellow, 25 percent was dedicated to departmental work at ITS. In 2020 and 2021 I was a teaching assistant in the course TEK5160/9160 – Radar Remote Sensing. In 2021 and 2022, some of the departmental work was carried out at the RIMFAX Science Operation Center as a payload lead during tactical Mars 2020 surface operations.

I would like to acknowledge Anders Moe and Erlend Kvinnesland at Geocap AS, for letting me test and use commercial 3D geospatial and geophysical software during the course of this thesis (Geocap; Ground Model plug-in for ArcGIS). The open source project gprMax has been a central part in most of this research, and I am grateful for the open access that has been provided to this capable simulation code. Computations were performed on the Norwegian Research and Education Cloud (NREC), using resources provided by the University of Bergen and the University of Oslo.

At last, I have really appreciated the company of my colleagues and office-mates that made the last years a fun time. And to my dazzling Natasha, I truly cherish your support and cheerfulness.

Sigurd Eide
Oslo, November 2022

Summary of Thesis

Main findings of this thesis involves quantitative analysis of RIMFAX data from NASA's Perseverance rover mission on Mars and the exploration of Jezero Crater Floor. Numerical modeling of radar wave propagation in subsurface media is a central part of the work, which is used to assess imaging prior to acquisition and to ensure adequate implementation of analysis techniques. The synopsis provides background information of planetary radar investigations and the Perseverance rover mission. Theory of signal acquisition as relevant for RIMFAX is addressed in greater detail, together with theory of electromagnetic wave propagation in realistic subsurface media, and numerical modeling methods. The papers study selected topics related to Mars subsurface properties, RIMFAX modeling, and quantitative analysis. First results from Mars are also presented.

Norwegian Language Summary | Oppsummering av avhandling

Hovedfunnene i denne avhandlingen involverer kvantitativ analyse av RIMFAX data fra NASAs Perseverance rover-oppdrag på Mars og utforskningen av Jezero Crater Floor. Numerisk modellering av radarbølger i geologisk materiale er en sentral del av arbeidet, brukt til å vurdere avbildning i forkant av datafangst og sikre korrekt implementering av analyseteknikker. Kappen gir bakgrunnsinformasjon om planetær utforskning med radar og Perseverance rover-oppdraget. Teori om datafangst relevant for RIMFAX er beskrevet nærmere, sammen med teori om elektromagnetisk bølgeutbredelse i realistisk geologisk materiale, og numeriske modelleringsmetoder. Artiklene fokuserer på utvalgte temaer innen geologisk materiale på Mars, numerisk modellering av RIMFAX-instrumentet, og kvantitativ analyse. De første resultatene fra Mars blir også presentert.

List of Papers

Paper I

Eide, S., Hamran, S. E., Dypvik, H., and Amundsen, H. E. F. "Ground-Penetrating Radar Modeling Across the Jezero Crater Floor". In: *IEEE Journal of Selected Topics in Applied Earth Observations and Remote Sensing*. Vol. 14, (2021), pp. 2484–2493. DOI: 10.1109/JSTARS.2021.3055944.

Paper II

Eide, S., Casademont, T., Aardal, Ø. L., and Hamran, S. E. "Modeling FMCW Radar for Subsurface Analysis". In: *IEEE Journal of Selected Topics in Applied Earth Observations and Remote Sensing*. Vol. 15, (2022), pp. 2998–3007. DOI: 10.1109/JSTARS.2022.3165135.

Paper III

Eide, S., Casademont, T., Berger, T., Dypvik, H, Shoemaker, E., and Hamran, S. E. "Radar Attenuation in the Shallow Martian Subsurface: RIMFAX Time-Frequency Analysis and Constant-Q Characterization over Jezero Crater Floor". In: *Geophysical Research Letters*. Vol. 50, (2022), pp. e2022GL101429. DOI: 10.1029/2022GL101429.

Paper IV

Eide, S., Dypvik, H., Amundsen, H. E. F., Page, D., and Hamran, S. E. "RIMFAX Dip Attribute Analysis: Unconformity Detection and True Dip in the Martian Subsurface". In: *19th International Conference on Ground Penetrating Radar*. Society of Exploration Geophysicists, (2022), pp. 159–162. DOI: 10.1190/gpr2022-018.1.

Additional Contributions

Casademont, T. M., **Eide, S.**, Shoemaker, E. S., Liu, Y., Nunes, D., Russell, P., Dypvik, H., Amundsen, H. E. F., Berger, T., and Hamran, S. E., "RIMFAX Ground Penetrating Radar Reveals Dielectric Permittivity and Rock Density of Shallow Martian Subsurface". In: *Journal of Geophysical Research: Planets*. Vol. 128, (2023), pp. e2022JE007598. DOI: https://doi.org/10.1029/2022JE007598.

Hamran, S. E., Paige, D. A., Allwood, A., Amundsen, H. E., Berger, T., Brovoll, S., Carter, L., Casademont, T. M., Damsgård, L., Dypvik, H., **Eide, S.**, Fairén, A. G., Ghent, R., Kohler, J., Mellon, M., Nunes, D. C., Plettemeier, D., Russell, P., Siegler, M., and Øyan, M. J. "Ground penetrating radar observations of subsurface structures in the floor of Jezero crater, Mars". In: *Science Advances*. Vol. 8, no. 34 (2022), pp. eabp8564. DOI: https://doi.org/10.1126/sciadv.abp8564.

Stack, K. M., Williams, N. R., Calef, F., Sun, V. Z., Williford, K. H., Farley, K. A., **Eide, S.**, Flannery, D., Hughes, C., Jacob, S. R., Kah, L. C., Meyen, F., Molina, A., Nataf, C. Q., Rice, M., Russell, P., Scheller, E., Seeger, C. H., and others "Photogeologic map of the perseverance rover field site in Jezero Crater constructed by the Mars 2020 Science Team". In: *Space Science Reviews*. Vol. 216, no. 8 (2020), pp. 1-47. DOI: https://doi.org/10.1007/s11214-020-00739-x.

Hamran, S. E., Paige, D. A., Amundsen, H. E., Berger, T., Brovoll, S., Carter, L., Damsgård, L., Dypvik, H., Eide, J., **Eide, S.**, Ghent, R., Helleren, Ø., Kohler, J., Mellon, M., Nunes, D. C., Plettemeier, D., Rowe, K., Russell, P., and Øyan, M. J. "Radar imager for Mars' subsurface experiment—RIMFAX". In: *Space Science Reviews*. Vol. 216, no. 8 (2020), pp. 1-39. DOI: https://doi.org/10.1007/s11214-020-00740-4.

Eide, S. "Kappløpet om Mars" In: *GEO Energi og Ressurser*. (2019), pp. 18–20.

Eide, S., Hamran, S., Dypvik, H., and Amundsen, H. E. F. "RIMFAX Ground Penetrating Radar Modelling: Imaging the Subsurface of the Jezero Western Delta". In: *Ninth International Conference on Mars*. (2019), Abstract #6070.

Contents

Preface i

Summary of Thesis iii

List of Papers v

Additional Contributions vii

Contents ix

List of Tables xi

List of Figures xi

List of Abbreviations xiii

1 Introduction 1
1.1 Thesis topics and objectives . . . 1
1.2 Outline of thesis . . . 2
1.3 Ground-penetrating radar in planetary exploration . . . 3
1.4 Modeling studies for planetary subsurface sounding . . . 7
References . . . 10

2 The Mars 2020 Perseverance Rover Mission 13
2.1 Mission overview . . . 13
2.2 Jezero Crater landing site . . . 14
2.3 Summary of Crater Floor exploration, first 414 sols . . . 18
References . . . 21

3 Radar Imager for Mars' subsurFAce eXperiment (RIMFAX) 25
3.1 Signal acquisition . . . 25
3.2 Radargram generation . . . 30
3.3 Monostatic 2D-imaging . . . 30
3.4 Displaying radargram profiles . . . 34
3.5 Quantitative analysis . . . 36
References . . . 40

4 Subsurface Properties and Ground-Penetrating Radar Modeling 43
4.1 Subsurface media properties . . . 43

4.2 Computational electromagnetic methods 51
References 56

5 Summary of Papers and Future Work 59
References 62

Papers 64

I Ground-Penetrating Radar Modeling Across the Jezero Crater Floor 65

II Modeling FMCW Radar for Subsurface Analysis 77

III Radar Attenuation in the Shallow Martian Subsurface: RIMFAX Time-Frequency Analysis and Constant-Q Characterization over Jezero Crater Floor 89

IV RIMFAX Dip Attribute Analysis: Unconformity Detection and True Dip in the Martian Subsurface 101

Appendices 107

A BGS Groundhog Desktop GSIS as Model Builder for gprMax, for Assessment of Subsurface Hypotheses 109

B RIMFAX Dip Attribute Analysis: Extended Results 121

List of Tables

1.1 Overview of radar science and in-situ dielectric measurements on Mars 8

3.1 Nominal RIMFAX acquisition modes while driving 29
3.2 Radar equation variables 37

4.1 Comparison of computational electromagnetic methods 52

List of Figures

1.1 RIMFAX electronics box and antenna on the Perseverance rover 2
1.2 Apollo 17 Surface Electrical Properties Experiment 4
1.3 Lunar Penetrating Radar results from the Chang'E-4 mission . . 6
1.4 Modeling of Lunar Penetrating Radar response 9

2.1 Image of Perseverance rover and Ingenuity helicopter 14
2.2 Regional map of Jezero Crater and surroundings 16
2.3 Map of Jezero Crater 17
2.4 Map overview of the Crater Floor campaign 19

3.1 Artistic illustration of RIMFAX operation 25
3.2 Block diagram of RIMFAX instrument design 26
3.3 FMCW deramped signal 27
3.4 FMCW target response 28
3.5 FMCW gating 29
3.6 Central processing steps for radargram generation 31
3.7 Topography correction processing step 32
3.8 Illustration of monostatic 2D imaging and migration 33
3.9 Improved RIMFAX imaging with migration 34
3.10 RIMFAX 3D GIS view in Ground Model plug-in for ArcGIS . . 35
3.11 Radar system dynamic range 38
3.12 RIMFAX system dynamic range 38
3.13 RIMFAX returned power analysis 40
3.14 RIMFAX spectral analysis 41

4.1 Electromagnetic propagation velocity and attenuation 45
4.2 Rock permittivity dependency on water content and density . . 46

4.3 Dielectric models 48
4.4 Volume scattering loss models 49
4.5 Reflectivity as a function of surface roughness 51
4.6 FDTD discretized Yee cell 54

List of Abbreviations

ABC : Absorbing Boundary Condition
ALSE : Apollo Lunar Sounder Experiment
ATLO : Assembly, Test, and Launch Operations
BGR / BG REM : Background Removal
BGS : British Geological Survey
C-band : Microwave band covering frequencies from 4 to 8 GHz
CEM : Computational Electromagnetics
Cf-f-1/2 : Crater floor fractured 1/2 (geological map unit)
Cf-fr : Crater floor fractured rough (geological map unit)
CFL : Courant–Friedrichs–Lewy condition
CNSA : China National Space Administration
com. : Communication
CONSERT : Comet Nucleus Sounding Experiment by Radio wave Transmission
DEM : Digital Elevation Model
EM : Electromagnetic
ESA : European Space Agency
FDTD : Finite-Difference Time-Domain
FEM : Finite Element Method
FFT : Fast Fourier Transform
FMCW : Freuency Modulated Continous Wave
GIS : Geographical Information System
GPR : Ground Penetrating Radar
GPU : Graphics Processing Unit
GSIS : Geo-Scientific Information System
HF : High Frequency, covering the frequency band from 3 to 30 MHz
HiRISE : High Resolution Imaging Science Experiment
HPC : High-Performance Computing
IEEE : Institute of Electrical and Electronics Engineers
JPL : Jet Propulsion Laboratory
JUICE : The Jupiter Icy Moons Explorer
L-band : Microwave band covering frequencies from 1 to 2 GHz
LPF : Low-pass filter
MARSIS : Mars Advanced Radar for Subsurface and Ionosphere Sounding
MEX : Mars Express
MoM : Method-of-Moments
MOSIR : The Mars Orbiter Subsurface Investigation Radar
MPI : Message Passing Interface
MRO : Mars Reconnaissance Orbiter
NASA : National Aeronautics and Space Administration

OEB : Octavia E. Butler landing site
PML : Perfectly Matched Layer
RCS : Radar Cross Section
RGB : Red, Green and Blue
RIME : Radar for Icy Moon Exploration
RIMFAX : Radar Imager for Mars' Subsurface Experiment
RMS : Root-mean-square
RoPeR : Mars Rover Penetrating Radar
RSC : Roscosmos
S-band : Microwave band covering frequencies from 2 to 4 GHz
SAR : Synthetic-Aperture Radar
SDR : System Dynamic Range
SEG : Society of Exploration Geophysicists
SHARAD : Mars Shallow Radar sounder
SNR : Signal-to-Noise Ratio
SVD : Singular Value Decomposition
TECP : The Thermal and Electrical Conductivity Probe
TWT : Two-way travel time
UHF : Ultra High Frequency, covering frequency band from 0.3 to 1 GHz
Us : Undifferentiated smooth (geological map unit)
UWB : Ulta-wideband
VHF : Very High Frequency, covering the frequency band from 30 to 300 MHz
VNIR : Visible-to-near-infrared
WISDOM : Water Ice and Subsurface Deposit Observation on Mars
X-band : Microwave band covering frequencies from 8 to 12 GHz

Chapter 1

Introduction

1.1 Thesis topics and objectives

This thesis was compiled during the period 2018 - 2022 and covers a number of significant phases of the Mars 2020 Perseverance rover mission. The first two and a half years coincided with preparatory work prior to surface operations, comprising the landing site selection in October 2018, launch on 30th of July 2020, and the anticipatory six and a half month in-flight towards Mars. After successful landing on 18th of February 2021, about a year and a half was dedicated to surface operation and exploration of Jezero Crater Floor. The content of the synopsis and the peer-reviewed papers clearly reflects that the first half of the thesis work was done during preparatory stages, with conjecture of future data acquisition, while the second half was done during initial mission operation and is focused on principal analyses of data acquired on Mars.

The main topics of this thesis are modeling and quantitative analysis related the Radar Imager for Mars' subsurFAce eXperiment (RIMFAX). RIMFAX is a ground-penetrating radar (GPR) included as a scientific payload instrument on the NASA Perseverance rover mission to Mars, Figure 1.1. There are two main objectives of this thesis, where GPR modeling is employed for

(i) preliminary assessment prior to acquisition, and

(ii) assisting interpretation and analysis of data acquired on Mars.

In particular is quantitative analysis of RIMFAX data studied in detail, attempting to disclose Martian subsurface properties and structures.

It is a multidisciplinary approach that needs to take into account several aspects of remote sensing in a frontier exploration mission. For subsurface studies, an understanding of the geology at a global and local scale is a prerequisite for studying formation and properties of the media of investigation. As no subsurface measurement comes with a clear and decisive interpretation, it is moreover imperative with thorough knowledge about the instrument and signal acquisition, as well as data processing and analysis. Computational science is another key topic in this thesis, as resource demanding numerical simulations are conducted to model electromagnetic wave propagation in realistic media. Lastly, as the positioning of measurements acquired on Mars are relevant when relating to orbital and surface imagery, or e.g. a geological model, effort was put into finding and configuring suitable software technology with geographical information capability.

Subsurface measurements are conducted in order to disclose some facts about the geology to support mission operations, or – on its own – for gaining some greater understanding of the local geological setting or planetary formation. In

Figure 1.1: Photo taken during Assembly, Test, and Launch Operations (ATLO) at NASA Jet Propulsion Laboratory (JPL), highlighting where RIMFAX is mounted on the Perseverance rover spacecraft. Location of electronics box within left aft tower (red highlight) and antenna at lower aft. Figure from Hamran et al. (2020). Image credit: NASA/JPL-Caltech.

both cases, a thorough understanding of which information could be extracted from the RIMFAX measurements is paramount. Therefore, considerable effort is put into reviewing available information about rock properties that could be relevant for acquisition, in parallel with investigating instrument functionality and techniques of data analysis. Numerical modeling experiments are in turn used to assess hypotheses and verify analysis techniques. A large part of the synopsis is therefore dedicated to reviewing GPR studies in planetary exploration and investigate how they have analysed data, and how modeling has been used to support acquisition, interpretation, processing and analysis. To put this research about RIMFAX into context, the Mars 2020 mission and initial results are also given considerable attention.

1.2 Outline of thesis

The synopsis provide the background for the four peer-reviewed papers of this thesis, and it is divided into five chapters. To begin with, the remaining of this chapter will address the history of GPR in planetary exploration. How modeling has been employed to support acquisition, processing and analysis will be given special attention. For RIMFAX' pioneering mapping of the shallow

Martian subsurface, it is important to gain knowledge from similar endeavours. A substantial part of the early thesis work was figuring out how modeling could be used to meet the thesis' objectives, so it was beneficial to review former work for inspiration. Chapter 2 will embark on the Perseverance rover mission, outlining mission objectives and reviewing the Jezero Crater landing site geology. A section is dedicated to major discoveries and achievements during exploration of the Crater Floor, covering the first year and a half of surface operation. The RIMFAX instrument is described in Chapter 3, reviewing the GPR technique and emphasizing characteristics of the instrument. This is important for understanding what information can be retrieved from the data and which modeling approach is appropriate. Chapter 4 starts with describing media properties relevant for radar sounding, before reflecting on suitability of various modeling techniques. The finite-difference time-domain (FDTD) method was selected for this thesis work and is therefore reviewed in more detail. At last, Chapter 5 briefly summarizes the four peer-reviewed papers and provide some reflection on how the thesis objectives have been met and what would be the natural continuation for future work. The thesis has furthermore attached the four peer-reviewed science papers, in addition to two appendices describing certain topics in greater detail.

1.3 Ground-penetrating radar in planetary exploration

GPR is a well-proven remote sensing technique with an increasing use in space missions. It has become a popular payload instrument due to a combination of light-weight, durable and easily manoeuvrable hardware, in addition to low energy consumption and low data rate. Principal uses in planetary exploration is related geology and measuring electrical properties at the surface and in the subsurface. Looking ahead, with the emerging interest in subsurface science (Stamenković et al., 2019), and especially with regards to water detection and in-situ resource utilization for future manned missions to the Moon and Mars, the role of GPR is expected to increase in the time ahead.

Mapping the surfaces of the Moon and planets started with radio astronomy and sounding from radio telescopes on Earth (e.g., Evans, 1969), determining electrical properties by measuring power in the backscattered signal. With emergence of the space age in the 1960s and -70s, bistatic experiments begun with transmitters mounted on orbiters or flyby spacecrafts, and receivers on Earth measuring reflections off the surfaces of the Moon and Mars (e.g., Fjeldbo, 1964; Simpson et al., 2009). Bistatic radar experiments were eventually also conducted between landing modules and orbiters, like when using the lander-to-orbiter relay links on the Viking missions to perform measurements of the electric surface properties on Mars (Tang et al., 1977).

It was during NASA's Apollo 17 mission in 1972, however, that a third dimension was introduced to planetary exploration. First, on the command and service module orbiting the Moon was the Apollo Lunar Sounder Experiment (ALSE; Phillips et al., 1973). Sounding was conducted with VHF and HF

radars, mapping the surface and subsurface down to ∼1.5 km, providing the first recorded reflections from the Moon's interior. Second, the start of shallow near-surface measurements in planetary exploration began while the Apollo astronauts were on the surface, carrying out the Surface Electrical Properties experiment (Simmons et al., 1973). It had a bistatic configuration with the transmitter deployed on the lunar surface and the receiver mounted on the lunar roving vehicle, Figure 1.2. With transmission done at discrete frequencies in the HF range, the vehicle with the receiver would drive off and measure the interference pattern of one or more waves. Inversion of the composite signal gives an estimate of electrical properties in the lunar subsurface.

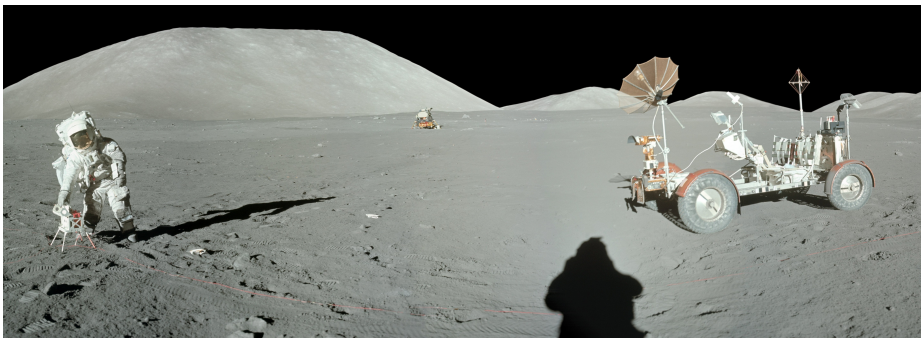

Figure 1.2: Photo taken during deployment of the Apollo 17 Surface Electrical Properties experiment, cropped from frames A17-134-20440 to A17-134-20446. Image credit: NASA.

Building on the experience from ALSE, a new era began in the first decade of the twenty first century with orbiting spacecrafts equipped with HF radars, surveying subsurface structures from tens of meters down to a few km depth. First out was the European Space Agency (ESA) with MARSIS in 2003 (Picardi et al., 2004), set out to map subsurface structures and the distribution of liquid and frozen water in the Martian crust. MARSIS can operate at center frequencies between 1.8 and 5 MHz, with high penetration (up to 5 km) and a relatively coarse vertical resolution (150 m in free-space and 50 m in the subsurface[1]). Moreover, using telecommunication onboard the spacecraft and receivers on Earth, bistatic radar experiments were also conducted to measure surface properties at X-band and S-band frequencies (Simpson et al., 2006). NASA's SHARAD radar followed in 2005 (Seu et al., 2007), conducting soundings at 20-MHz center frequency and 10 MHz bandwidth, mapping structures down to some hundred meters depths and with fine vertical resolution (15 m in free-space and 5 m in the subsurface[1]). It has made several discoveries including layering in the South Polar ice cap, buried craters and thickness of volcanic layering. On the Moon, the Lunar Radar Sounder (Ono et al., 2010) was put into orbit in 2007 by the Japanese space agency. It detected basalt and regolith layering down to several hundred

[1]For an assumed subsurface velocity of 0.1 m/ns.

meters, sounding at 5 MHz center frequency with a vertical resolution of 150 m in free-space and 50 in the subsurface[1]. To improve along-track resolution, all the orbiting radars employ the synthetic-aperture radar (SAR) principle.

An orbital mounted VHF radar with a truly exotic destination was the bistatic radar experiment CONSERT on ESA's ROSETTA mission (Kofman et al., 2015). Set out to investigate a comet in 2004 and 10 years later arriving at its destination, a transmitter on the orbiter was used to probe the comet while a receiver attached to a landing module had been deployed at the comet surface. Through several revolutions and performing a tomographic inversion of the recorded data, it was possible to constrain the comet's inner structures. Another frontier mission, JUICE, is bound for Jupyter and planned for launch in mid 2020s. The HF RIME radar onboard (Bruzzone & Croci, 2019) is aimed at studying the subsurface of the Jovian moons, with expected penetration depths in the range 1-9 km with a vertical resolution of 30–90 m in ice.

In 2013, the Chinese Chang'E-3 mission was the first to conduct a soft landing on the Moon since the mid-1970s and the Luna missions by the Soviet Union. Yet again, a few years later in 2019, the Chang'E-4 mission became the first to land on the Moon's farside. Both landers deployed a rover equipped with the same payload instrument named Lunar Penetrating Radar (Fang et al., 2014; Li et al., 2020). Compared to orbital sounding, the radars are operated at 60 MHz and 500 MHz center frequencies and enable detailed imaging of the shallow subsurface in a much higher resolution (3 m and 20 cm, for the two channels). Result have given insights to the composition of the regolith in the upper tens of meters; Figure 1.3 is an example of interpreted results from data acquired on the farside of the Moon.

In the third decade of the twenty first century, attention is towards Mars. After a series of successful NASA rover missions to the planet during the preceding decades (Spirit and Opportunity in 2006, and Curiosity in 2013), a new generation of Mars rovers are ready to start exploring. All are equipped with GPRs for mapping subsurface structures. RIMFAX was first out and started conducting soundings in the beginning of 2021, when NASA's Perseverance rover began traversing over the Martian surface. Operating in the frequency range 150-1200 MHz, it is a ultra-wideband radar for both surface, shallow (<1m) and deep (>10m) sounding (as described in-detail in Chapter 3). Some months after, the Chinese Tianwen-1 mission arrived, consisting of an orbiter, landing module and rover. GPRs are included on both the rover (Zhou et al., 2020) and orbiter (Fan et al., 2021). The rover-mounted radar RoPeR consists of two channels operating at 35-75 MHz and 0.8-1.8 GHz. The low frequency channel will provide penetrating depths of 10-100 m with a resolution of a few meters within the Martian soil, and the higher frequency channel will penetrate to depths of 3-10 m with a resolution of a few centimeters. The orbiting radar MOSIR will operate in discrete bands between 10 and 50 MHz and employ the SAR technique similarly to other orbiting systems. The ExoMars European-Russian collaboration was originally planned for launch in 2020 with yet another GPR-equipped rover. Its WISDOM radar is operating in the 0.5-3 GHz frequency range, and is designed to explore the first ∼3 m of the subsurface with a vertical resolution of a few cm

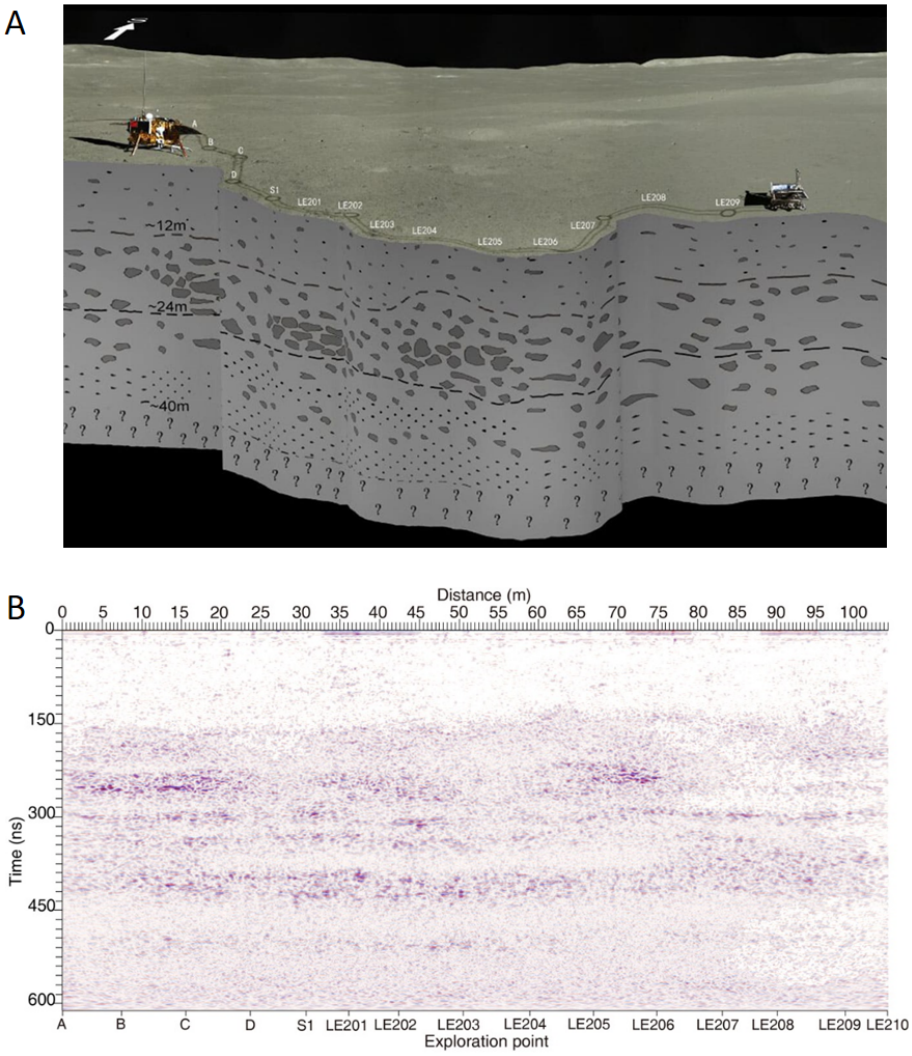

Figure 1.3: Lunar Penetrating Radar results from the Chang'E-4 mission the farside of the Moon. (A) Interpreted subsurface structures beneath the rover path. Image credits: CLEP/GRAS/NAOC. (B) Corresponding 500-MHz channel radargram. Figure from Li et al. (2020).

(Ciarletti et al., 2011). Unfortunately, the mission has suffered several delays and as of 2022 the launch date is unknown.

Having provided an historical context for RIMFAX' pioneering near-surface mapping on Mars, it will enable measurements to be related to previously acquired data. For example, the Martian surface and subsurface has already been investigated through radio astronomy and by orbital radars, but at a much larger spatial scale. Morgan et al. (2018) investigated if shallow subsurface detections by SHARAD at the Mars 2020 landing site could potentially also be seen by RIMFAX. However, due to SHARAD's large spatial footprint and the topographic variation around the landing site, clutter obscure subsurface reflections and make such correlation problematic. Paper I provides an overview of in-situ geophysical investigations done on Mars and how they can be related to RIMFAX measurements and the geology of the Mars 2020 landing site. A summary of radar soundings and dielectric measurements conducted on Mars, is also provided in Table 1.1.

1.4 Modeling studies for planetary subsurface sounding

The relatively low constraint on GPR subsurface imaging has made modeling popular among the GPR community, with increasing interest through availability of open source software (Warren et al., 2016). In planetary exploration in particular, the remote and unfamiliar terrain demands for extra support when analyzing the results. This is further augmented by monostatic or simple bistatic acquisition design for spacecraft mounted antennas, which makes interpretation of results non-unique.

There have been principally three usages in planetary exploration: (1) pre-acquisition assessment, (2) interpretation support, and (3) enhancement of processing and analysis techniques. All use-cases employ forward modeling, that is, where the radar response is generated from a predefined model. Depending on the aim of the study, distinct modeling methods are employed. Ray-tracing can be useful for investigating a narrow-band radar, e.g. for studying CONSERT on the ROSETTA mission (Kofman et al., 2020), while for ultra-wideband (UWB) radars and near-surface imaging, 'full-wave' modeling solving Maxwell's equations directly is more suitable (Davidson, 2010). Modeling techniques are addressed in more detail in Section 4.2. An example of a typical forward modeling application in planetary exploration in presented in Figure 1.4, where the Lunar Penetrating Radar response has been acquired over a generic subsurface model for supporting both processing and interpretation.

Inversion modeling, where the subsurface model is obtained directly from the GPR measurements, is a less common approach. There is increasing interest for inversion of GPR data for terrestrial surveys (van der Kruk et al., 2018), with e.g. multichannel acquisition that enables enhanced imaging by applying migration techniques (Binningsbo et al., 2000). The typical low constraint on acquisition geometry in planetary exploration, makes inversion an ill-posed problem with non-unique inversion results.

Period	Instrument	Mission	Type	Description
Past				
1969	com.	Mariner 6,7	flyby-Earth	Flyby-to-Earth S-band relay link bistatic radar experiment.
1976	com.	Viking	lander-orbiter	Lander-to-orbiter VHF relay link bistatic radar experiment.
2005	com.	Odyssey	orbiter-Earth	UHF bistatic radar experiment between Earth and orbiter.
2008	TECP	Phoenix	lander	Electrical conductivity probe.
Present				
2005 -	MARSIS	MEX	orbiter	HF GPR
2005 -	com.	MEX	orbiter-Earth	Orbiter-to-Earth S- and X-band bistatic radar experiment.
2006 -	SHARAD	MRO	orbiter	HF GPR
2021 -	RIMFAX	Mars 2020	rover	UHF GPR
2021 -	RoPeR	Tianwen-1	rover	VHF and L-band GPR
2021 -	MOSIR	Tianwen-1	orbiter	HF - VHF GPR
Future				
	WISDOM	ExoMars	rover	UHF - S-band GPR

Table 1.1: Overview of radar soundings and dielectric measurements conducted in-situ, from Mars orbit or during flyby.

Several studies have been done to assess acquisition prior to mission start and data gathering. A range of modeling techniques have been used, e.g. ray-tracing for hypothesized geometric imaging and assessment of penetration depths (Fa, 2012), and full-wave modeling for more realistic propagation (Heggy et al., 2017). Forward modeling is typically conducted over a subsurface model constructed based on the available information and educated guesses. Drawing on the experience from the orbiting radars on Mars, however, quantifying specific measures like e.g. penetration depths in front of data acquisition can be very difficult due to the unknown subsurface environment (Stillman & Grimm, 2011). Therefore, pre-acquisition modeling is likely more useful for making general considerations, than for specific quantified predictions. Paper I of this thesis uses forward modeling to assess imaging at the Mars 2020 landing site based on orbital imagery and best-guess rock parameters.

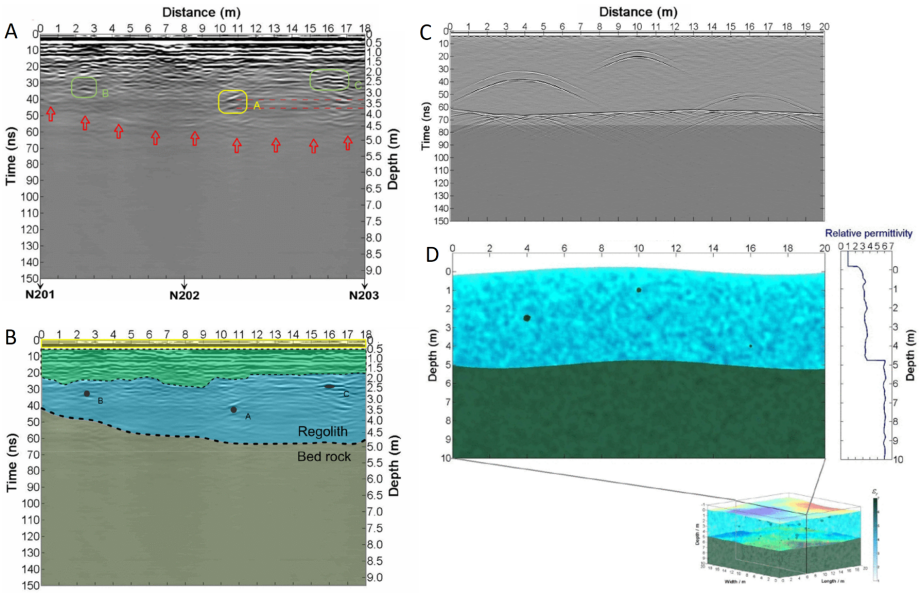

Figure 1.4: Example of Lunar Penetrating Radar data and modeling over a generic subsurface model. A) Lunar Penetrating Radar data with annotations, B) interpreted geology, C) synthetic radargram modeled to support interpretation, and D) generic subsurface model used for modeling. The authors were in this study i.a. investigating what the synthetic response would be from modeling with realistic heterogeneous subsurface conditions, and then using this to support processing of the acquired GPR data and their geologic interpretation. Figure modified from Zhang et al. (2018).

After data acquisition, non-unique interpretation of radar sounding from unfamiliar terrain has raised modeling as an useful tool to e.g. assess hypotheses of subsurface structures and properties. There are examples of both 1D synthetic trace generation (Zhu et al., 2021) and full-wave modeling (Lai et al., 2020) for the Lunar Penetrating Radars on the Moon. Several studies have also used modeling to compare generic subsurface scenarios by forward modeling over e.g. heterogeneous subsurface models thought to represent the lunar regolith (Lai et al., 2017; Lv et al., 2020; Zhang et al., 2018).

Analyzing data from frontier exploration can be controversial, with examples of system noise having possibly been misunderstood for subsurface structures (Li, Xing, et al., 2017; Pettinelli et al., 2021). For this reason, modeling has also been employed to assess processing (Li & Zhang, 2021; Zhang et al., 2018) and developing analysis methods (Giannakis et al., 2021; Li, Zeng, et al., 2017). Central in both Paper III and IV of this thesis are generation of synthetic radargrams with the purpose of developing and testing analysis techniques.

References

Binningsbo, J., Eide, E. S., & Hjelmstad, J. F. (2000). 3d migration of GPR array-antenna data. *Eighth International Conference on Ground Penetrating Radar*, vol. 4084, 459–463.

Bruzzone, L., & Croci, R. (2019). Radar for icy moon exploration (RIME). *2019 IEEE 5th International Workshop on Metrology for AeroSpace (MetroAeroSpace)*, 330–333.

Ciarletti, V., Corbel, C., Plettemeier, D., Cais, P., Clifford, S. M., & Hamran, S.-E. (2011). WISDOM GPR designed for shallow and high-resolution sounding of the Martian subsurface. *Proceedings of the IEEE*, vol. 99no. 5, 824–836.

Davidson, D. B. (2010). *Computational electromagnetics for RF and microwave engineering* (2nd ed.). Cambridge University Press.

Evans, J. (1969). Radar studies of planetary surfaces. *Annual Review of Astronomy and Astrophysics*, vol. 7no. 1, 201–248.

Fa, W. (2012). Modeling and simulation for ground penetrating radar study of the subsurface structure of the moon. *2012 14th International Conference on Ground Penetrating Radar (GPR)*, 922–926.

Fan, M., Lyu, P., Su, Y., et al. (2021). The Mars Orbiter Subsurface Investigation Radar (MOSIR) on China's Tianwen-1 Mission. *Space science reviews*, vol. 217no. 1, 1–17.

Fang, G.-Y., Zhou, B., Ji, Y.-C., et al. (2014). Lunar Penetrating Radar onboard the Chang'e-3 mission. *Research in astronomy and astrophysics*, vol. 14no. 12, 1607.

Fjeldbo, G. (1964). *Bistatic-radar methods for studying planetary ionospheres and surfaces*. Radioscience Laboratory, Stanford Electronics Laboratories, Stanford University.

Giannakis, I., Zhou, F., Warren, C., & Giannopoulos, A. (2021). Inferring the shallow layered structure at the Chang'E-4 landing site: A novel interpretation approach using Lunar Penetrating Radar. *Geophysical Research Letters*, vol. 48no. 16, e2021GL092866.

Hamran, S.-E., Paige, D. A., Amundsen, H. E., et al. (2020). Radar imager for Mars' subsurface experiment—RIMFAX. *Space Science Reviews*, vol. 216no. 8, 1–39.

Heggy, E., Scabbia, G., Bruzzone, L., & Pappalardo, R. T. (2017). Radar probing of Jovian icy moons: Understanding subsurface water and structure detectability in the JUICE and Europa missions. *Icarus*, vol. 285, 237–251.

Kofman, W., Herique, A., Barbin, Y., et al. (2015). Properties of the 67p/churyumov-gerasimenko interior revealed by consert radar. *Science*, vol. 349no. 6247, aab0639.

Kofman, W., Zine, S., Herique, A., et al. (2020). The interior of Comet 67P/C–G; revisiting CONSERT results with the exact position of the Philae lander. *Monthly Notices of the Royal Astronomical Society*, vol. 497no. 3, 2616–2622.

Lai, J., Xu, Y., Bugiolacchi, R., et al. (2020). First look by the Yutu-2 rover at the deep subsurface structure at the lunar farside. *Nature communications*, vol. 11no. 1, 1–9.

Lai, J., Xu, Y., Zhang, X., & Tang, Z. (2017). Lunar regolith stratigraphy analysis based on the simulation of lunar penetrating radar signals. *Advances in Space Research*, vol. 60no. 9, 2099–2107.

Li, C., & Zhang, J. (2021). Velocity analysis using separated diffractions for lunar penetrating radar obtained by Yutu-2 rover. *Remote Sensing*, vol. 13no. 7, 1387.

Li, C., Su, Y., Pettinelli, E., et al. (2020). The Moon's farside shallow subsurface structure unveiled by Chang'E-4 Lunar Penetrating Radar. *Science advances*, vol. 6no. 9, eaay6898.

Li, C., Xing, S., Lauro, S. E., et al. (2017). Pitfalls in GPR data interpretation: False reflectors detected in Lunar radar cross sections by Chang'e-3. *IEEE Transactions on Geoscience and Remote Sensing*, vol. 56no. 3, 1325–1335.

Li, J., Zeng, Z., Liu, C., Huai, N., & Wang, K. (2017). A study on lunar regolith quantitative random model and lunar penetrating radar parameter inversion. *IEEE Geoscience and Remote Sensing Letters*, vol. 14no. 11, 1953–1957.

Lv, W., Li, C., Song, H., Zhang, J., & Lin, Y. (2020). Comparative analysis of reflection characteristics of lunar penetrating radar data using numerical simulations. *Icarus*, vol. 350, 113896.

Morgan, G., Carter, L., & Putzig, N. (2018). Radar investigations of the Mars 2020 rover landing sites. *Lunar and Planetary Science Conference*, no. 2083, 1404.

Ono, T., Kumamoto, A., & Kasahara, Y. o. (2010). The lunar radar sounder (LRS) onboard the KAGUYA (SELENE) spacecraft. *Space Science Reviews*, vol. 154no. 1, 145–192.

Pettinelli, E., Lauro, S. E., Mattei, E., Cosciotti, B., & Soldovieri, F. (2021). Stratigraphy versus artefacts in the Chang'e-4 low-frequency radar. *Nature Astronomy*, vol. 5no. 9, 890–893.

Phillips, R., Adams, G., Brown Jr, W., et al. (1973). Apollo lunar sounder experiment. *NASA. Johnson Space Center Apollo 17 Prelim. Sci. Rept.*

Picardi, G., Biccari, D., Seu, R., et al. (2004). MARSIS: Mars advanced radar for subsurface and ionosphere sounding. *Mars Express: The Scientific Payload*, vol. 1240, 51–69.

Seu, R., Phillips, R. J., Biccari, D., et al. (2007). SHARAD sounding radar on the Mars Reconnaissance Orbiter. *Journal of Geophysical Research: Planets*, vol. 112no. E5.

Simmons, G., Strangway, D., Annan, P., et al. (1973). 15. surface electrical properties experiment. *Apollo 17: Preliminary Science Report*, vol. 330.

Simpson, R. A., Tyler, G. L., Hausler, B., Patzold, M., & Asmar, S. (2009). Bistatic radar probing of planetary surfaces. *2009 IEEE Radar Conference*, 1–4.

Simpson, R. A., Tyler, G. L., Pätzold, M., & Häusler, B. (2006). Determination of local surface properties using Mars Express bistatic radar. *Journal of Geophysical Research: Planets*, vol. 111no. E6.

Stamenković, V., Beegle, L., Zacny, K., et al. (2019). The next frontier for planetary and human exploration. *Nature Astronomy*, vol. 3no. 2, 116–120.

Stillman, D. E., & Grimm, R. E. (2011). Radar penetrates only the youngest geological units on Mars. *Journal of Geophysical Research: Planets*, vol. 116no. E3.

Tang, C., Boak III, T., & Grossi, M. (1977). Bistatic radar measurements of electrical properties of the Martian surface. *Journal of Geophysical Research*, vol. 82no. 28, 4305–4315.

van der Kruk, J., Liu, T., Mozaffari, A., et al. (2018). Gpr full-waveform inversion, recent developments, and future opportunities. *2018 17th International Conference on Ground Penetrating Radar (GPR)*, 1–6.

Warren, C., Giannopoulos, A., & Giannakis, I. (2016). gprMax: Open source software to simulate electromagnetic wave propagation for Ground Penetrating Radar. *Computer Physics Communications*, vol. 209, 163–170.

Zhang, L., Zeng, Z., Li, J., et al. (2018). Simulation of the lunar regolith and Lunar-Penetrating Radar data processing. *IEEE Journal of Selected Topics in Applied Earth Observations and Remote Sensing*, vol. 11no. 2, 655–663.

Zhou, B., Shen, S., Lu, W., et al. (2020). The Mars rover subsurface penetrating radar onboard China's Mars 2020 mission. *Earth and Planetary Physics*, vol. 4no. 4, 345–354.

Zhu, T., Zhang, J., & Lin, Y. (2021). Ultra-thick paleoregolith layer detected by Lunar Penetrating Radar: Implication for fast regolith formation between 3.6 and 2.35 Ga. *Geophysical Research Letters*, vol. 48no. 20, e2021GL095282.

Chapter 2

The Mars 2020 Perseverance Rover Mission

RIMFAX measurements are acquired as part of the large-scale effort of the Mars 2020 mission, and objectives of this thesis are also related the broader perspective of the mission. Therefore, a brief review of mission science objectives, spacecraft, the Jezero Crater landing site, etc., is necessary for providing the right context. This chapter will also provide a general geological overview of the Jezero Crater Floor, which was the exploration region during the first year and an half of surface operations. Both pre-landing geological interpretations and initial results from the first 414 sols[1] on Mars will be addressed.

2.1 Mission overview

The Mars 2020 mission is NASA's most recent of a series of robotic exploration missions to the surface of Mars. Bellow follows a brief and high-level overview, but for more detailed descriptions of mission concept, objectives, spacecraft and instruments, see Farley et al. (2020) and references therein. The main science objective "seeking signs of ancient life" builds upon previous exploration successes and discoveries from preceding decades. Starting with "follow the water" strategy in early 2000s, with the two twin Mars Exploration Rovers Spirit and Opportunity that together made a series of stunning discoveries about the planets water-rich past (e.g., Arvidson, 2016). An understanding of Mars' present condition and past geological history has emerged in parallel with growing global coverage by orbiting spacecrafts, having mapped the surface in increasing detail. A decade later, in 2013 the Mars Science Laboratory landed in Gale Crater to explore a potential "ancient habitable environment". Findings indicate that the ancient, extinct lake in Gale Crater could possibly have had favourable conditions for hosting biological life (Grotzinger et al., 2014). Now, with an increased astrobiological focus, Mars 2020 will take the next step and investigate if signs of ancient microbial life can be detected in the rock record.

A cache of ∼35 rock and regolith samples from the surface of Mars will be acquired in order to assess whether traces of life can be found. Return to Earth is planned towards the end of 2020s by a series of follow-up missions. Bringing the samples to Earth will not limit analysis by the highly capable – but yet constrained – rover payload, but will open up infinite possibilities of examination by state of the art present day and future technologies. On Mars, a suite of payload instruments will be used to characterize the geological composition by interpreting colour, texture, chemistry and mineralogy from

[1]The term 'sol' refers to a Martian day, referenced to the day of landing.

meter to submillimetre scale, all the while locating and studying areas from which the most interesting samples can be retrieved.

The design and other engineering aspects of the Perseverance rover has a high heritage from its predecessor Curiosity. Figure 2.1 shows one the first full-view image of the rover taken from the surface of Mars, acquired on sol 46. In the image is also the first rotor driven flying spacecraft on Mars, named Ingenuity (Balaram et al., 2021). It was included as a 3-month long technology demonstration, but after successful tests its operation got extended and it continued as a scout for the rover during surface operation. The 1.8 kg helicopter can easily fly over rugged terrain and image the ground, while the ∼1 tonnage rover with all scientific and engineering instruments on board needs to navigate safely around obstacles on the surface.

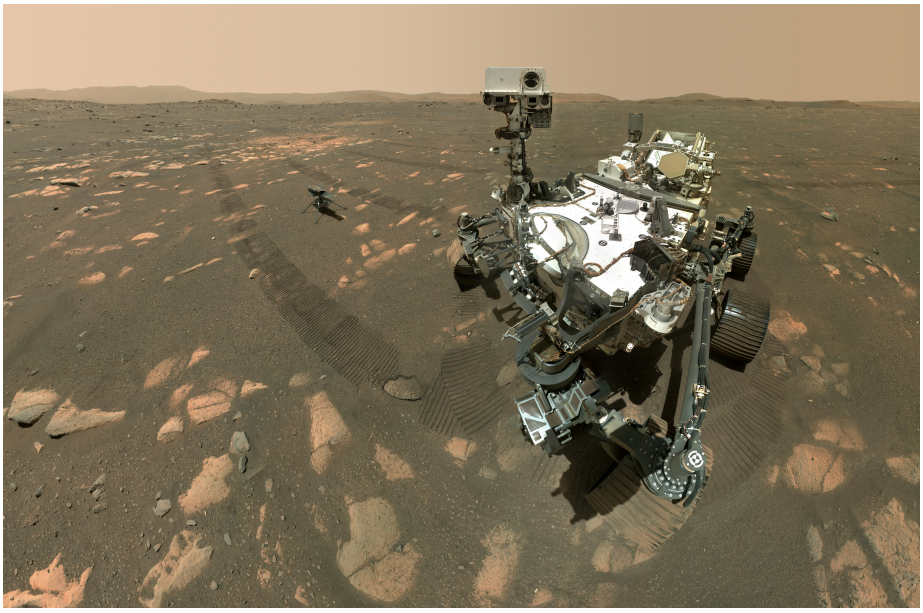

Figure 2.1: Image of Perseverance rover taken on sol 46 (06/04/2021) with the WATSON camera on the rover's robotic arm (Bhartia et al., 2021) . To the left in the image is the Ingenuity helicopter. Image credit: NASA/JPL-Caltech/MSSS.

2.2 Jezero Crater landing site

Over the time span of 5 years, a selection process worked on narrowing down an initial 28 proposed candidate landing sites for the Mars 2020 mission. With aspirations to explore an ancient habitable environment where posterior conditions may have preserved traces of biological activity, targeted sites should preferably contain old lithologies form the Noachian era (older than 3.5 Ga).

At this time, Mars may have had an active water cycle and thick atmosphere (e.g., Fassett & Head, 2008), presumably coinciding with an active magnetic field (Lillis et al., 2013). On Earth, the bulk evidence of ancient life has been found in the sedimentary record, deposited in shallow subaqueous settings. Therefore the major approach has been to search for geomorphological evidences of persistent water activity, together with mineralogical evidences of water-rock interaction as indicated in visible-to-near-infrared (VNIR) spectral mapping from orbit (Farley et al., 2020). Geological diversity among retrieved samples was also a criteria for the landing site selection; igneous rocks are though to be important for understating nature and timing of planetary formation, and sedimentary rocks may have recorded climatic conditions. In October 2018, Jezero Crater was selected as the primary mission, with Midway targeted for a extended mission scenario. Midway is located only ∼28 km from Jezero, in an area within Northeast Syrtis region that has exposures of very ancient crust and mineralogical indications of water-rock interaction.

The 45 km wide Jezero Crater is situated at mid-latitudes (18.4°N, 77.7°E) in the Nili Fossae region, Figure 2.2. It is on the Northwestern edge of the 1900 km wide and ∼3.9 Ga Noachian-aged Isidis impact basin (Fassett & Head, 2011; Werner, 2008). Nili Fossae is a region with a variety of geomorphological features interpreted to be extensive breccias and impact melts (Mustard et al., 2009; Mustard et al., 2007), younger fluvial channels (Fassett & Head, 2005), and possible lava flows extending from the Hesperian aged volcanic complex of Syrtis Major Planum to the west (Hiesinger & Head, 2004). Mineralogical composition in the region, detected from orbital observations in VNIR data, indicating early aqueous alteration (Ehlmann, Mustard, Murchie, et al., 2008; Ehlmann et al., 2009; Poulet et al., 2005).

Jezero Crater was possibly formed as a complex impact crater with a central peak that have later been eroded (Barlow et al., 2005), while based on general depth/diameter ratios for complex craters (Garvin et al., 2003), an infill of ∼1 km thick succession proceeding the timing of the impact is likely (Ehlmann, Mustard, Fassett, et al., 2008; Schon et al., 2012). Large amounts of scree, mass flows, density current, and melt rock most likely formed during the crater excavation and various stages of modification, comparable to terrestrial impacts where the aqueous origin is still discussed (Dypvik & Kalleson, 2010; Dypvik et al., 2018). Presumptuously in late Noachian time, a closed basin with standing water was contained within the crater, which later developed into a hydrologically open lake (Fassett & Head, 2005). Two possible inlet valleys entering the crater through the northern and western rims were feeding the lake system, while a breach in the eastern rim formed the major outlet. Located at the mouth of each inlet valley are deeply eroded deltaic deposits with morphology reminding of fluvial-dominated deltas (Fassett & Head, 2005; Schon et al., 2012).

Jezero is an appealing exploration target with mineralogical indications of water-rock interactions; phyllosilicates and carbonaceous material detected in VNIR data indicate early aqueous alteration (Ehlmann, Mustard, Fassett, et al., 2008), likely due to detrital deposited material sourced from the nearby Noachian terrain (Goudge et al., 2015). There are also geomorphological evidences of

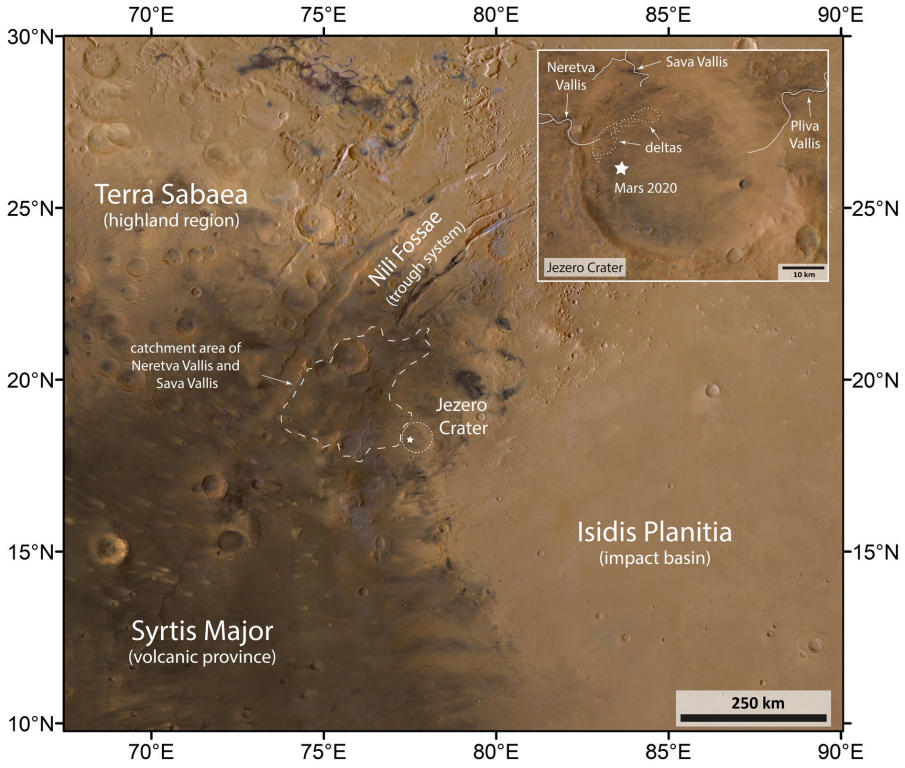

Figure 2.2: Regional map showing Jezero Crater's location between highlands, an impact basin, a volcanic province and ancient river systems. Inset figure highlights geomorphological features inside Jezero Crater like delta deposits and river valleys. Image credit: ESA/DLR/FU Berlin, CC BY-SA 3.0 IGO.

multiple depositional phases in the delta with, e.g., curvilinear scrollbars and layer dip indicating transition from foresets to bottomsets at the erosional scarp (Goudge et al., 2017; Goudge et al., 2015; Schon et al., 2012). A valley network feeding the Jezero Crater lake was estimated to be active between 3.74-3.83 Ga (Fassett & Head, 2008) suggesting Jezero Crater could contain old sedimentary lithologies.

2.2.1 Early understanding of the Crater Floor

After detailed geological mapping of Jezero Crater on orbital imagery prior to landing, stratigraphic and age relationships were still debated (Stack et al., 2020). The age of the main delta could not be determined with certainty, as with the relationship to the Crater Floor units. Figure 2.3 displays the map containing the geological units mapped prior to landing. Following the nomenclature in Stack et al. (2020), the Crater floor fractured (Cf-f-1/-2), has a light-toned high

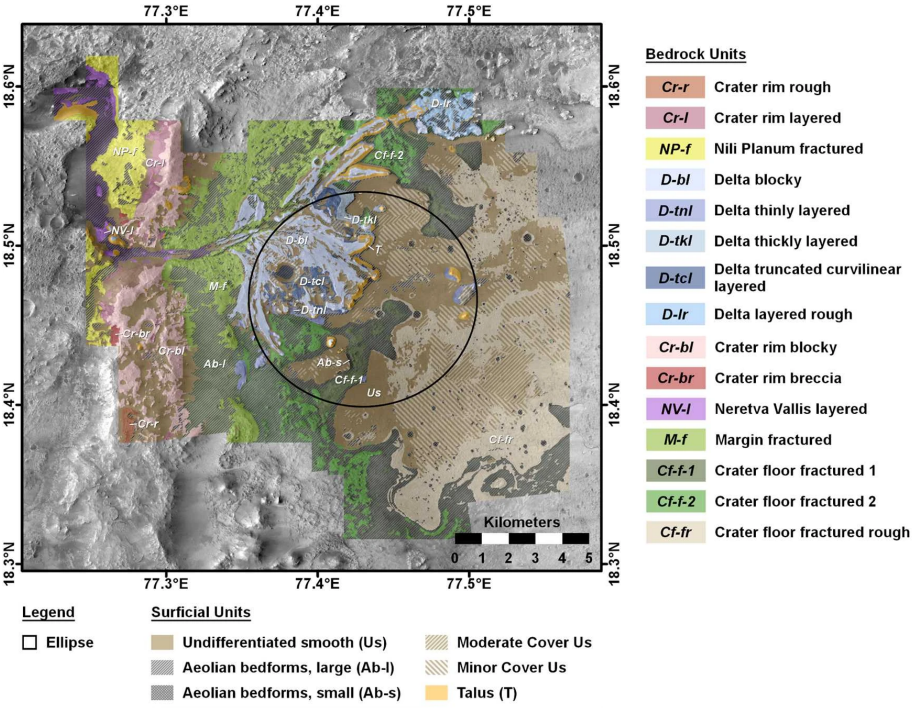

Figure 2.3: Map with geological units surrounding Jezero Western Delta and the landing ellipse, area where the Perseverance rover were estimated to land within. Geological map units in Jezero Crater defined from orbital imagery prior to landing. Figure from Stack et al. (2020).

albedo surface expression in HiRISE imagery. Exposures have a rough surface expression and polygonal fractures at a variety of scales, which is in contrast to the flatter and smoother-appearing surrounding terrain. Cf-f-1/-2 appear as meter-high topographic features on the Crater Floor. From orbital observations, this lithology was interpreted as the lowest visible unit among the post-impact deposits in Jezero Crater (Goudge et al., 2015; Schon et al., 2012). Olivine and Mg-carbonate signatures are detected in VNIR reflectance spectra (Ehlmann, Mustard, Fassett, et al., 2008; Goudge et al., 2015), which lead some authors to propose a possible relation to regional carbonate-bearing exposures observed more broadly in the Nili Fossae region (Goudge et al., 2015; Sun & Stack, 2019). A pre-landing assessment summarizing formation hypotheses is given in Brown et al. (2020).

The darker toned terrain consists of two subunits named Crater floor fractured rough (Cf-fr) and Undifferentiated smooth (Us), following the nomenclature in Stack et al. (2020). These were interpreted to be volcanic in origin from looking at geomorphology (Schon et al., 2012) and mineralogical signatures

(Goudge et al., 2015). 'Us' could likely be a non-uniform surficial mantle covering the underlying and more cratered surface lithology of Cf-fr, which gives the dark-toned terrain a varying morphological expression from smooth to rough (Stack et al., 2020). Interpreted to be the youngest consolidated lithology in Jezero, the relatively flat Cf-fr/Us terrain appears to onlap older strata within Jezero crater (Goudge et al., 2015; Schon et al., 2012).

VNIR-spectra of Cf-fr/Us shows mafic mineralogy (olivine and pyroxene content) indicative of a possible volcanic origin (Goudge et al., 2015; Horgan et al., 2020). Morphological observations supporting a low-viscous lava flow origin are a relative smooth and flat crater-retaining surface and lobating margins embaying neighbouring outcrops (Goudge et al., 2015; Schon et al., 2012). As noted by several authors (Horgan et al., 2020; Sun & Stack, 2019), however, alternative formational hypothesizes as a tephra or volcanoclastic deposit cannot be ruled out based on orbital observations alone; in particular, due to similarities to a regional unit on the rim and outside of Jezero crater.

Based on crater counting, estimated ages for the Cf-fr/Us range from 3.45 Ga in the Neukum system (Goudge et al., 2012), to 2.6 Ga (Shahrzad et al., 2019) and 1.4 Ga (Schon et al., 2012) in the Hartmann system. However, Stack et al. (2020) emphasize that caution needs to be applied in case 'Us' is a thin mantle covering underlying features so age estimates may only be correct in certain areas.

Schon et al. (2012) proposed emplacement of the Cf-fr/Us after cessation of fluvial activity, suggesting the delta was partially eroded prior to possible volcanic emplacement. This is consistent with Goudge et al. (2012) who studied volcanic resurfacing in Martian open-basin lakes and found no geomorphological evidence of lava-water interaction during emplacement in Jezero crater. Contrarily, Ruff (2017) suggested inverse stratigraphic relationships due to the lack of erosional contact in Cf-fr/Us towards the delta deposits. Alternatively, Ruff (2017) also indicated that this could be caused by a delta unit less prone to erosion than the CF-fr/Us material. Explaining this discrepancy, Horgan et al. (2020) advocated a more interfingered relationship, where parts of the delta could have been deposited after emplacement of the Cf-fr/Us.

2.3 Summary of Crater Floor exploration, first 414 sols

This section summarizes key data and findings from the first year and a half of the mission (first 414 sols) that was dedicated to investigating the Jezero Crater Floor. The rover had driven just above 10 km, the longest so far on another planet, and with its autonomous navigation had conducted a series of record breaking longest daily traverse lengths. Successful sampling had acquired a total of 8 rock cores, 1 atmospheric sample, and 1 witness tube. The Ingenuity helicopter got its operation time extended from the initial commissioning phase after landing, and conducted a total of 26 flights with 2950 seconds flight time, amounting to a accumulated distance of 6180 m. An overview map is presented in Figure 2.4.

Following a successful touch down on Mars the 18th of February 2021, having employed autonomous terrain-relative decent navigation to a locate a safe area within the predefined landing ellipse, the rover found it self on the Crater Floor. The landing site would soon be named after the American writer Octavia E. Butler (OEB), and initial system checks were conducted. The first three months was allocated to commissioning and initial Ingenuity helicopter activities, before embarking on The Crater Floor science campaign on sol 99. For the following three quarter of a year, the Perseverance rover and Ingenuity helicopter explored the geological units in the area and sampled the different lithologies. The Preseverance rover drove along the boundary between Cf-fr/Us and Cf-f-1, and onto the Cf-f-1 exposures from the Western side, before finally returning back to OEB. Afterwards on sol 382, the Rapid Traverse campaign started that took the rover from OEB and towards the Western Delta deposits where it arrived on sol 414.

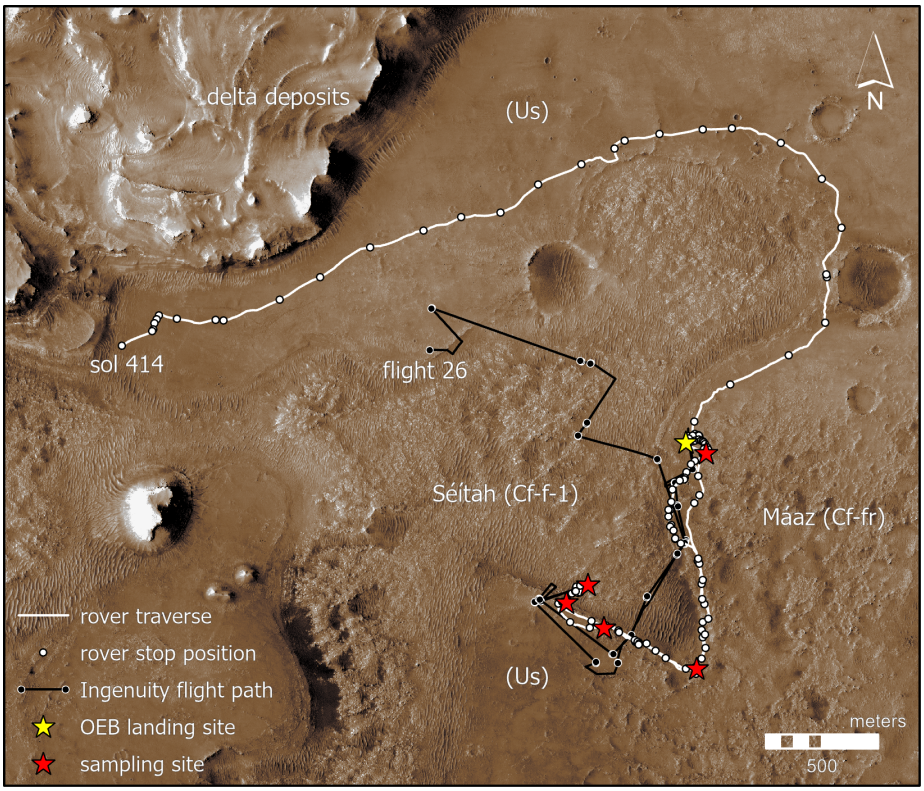

Figure 2.4: Map overview of the Perseverance rover traverse and the Ingenuity flight path during Crater Floor exploration. Mission features plotted on top of a false-colored HiRISE-imagery basemap.

After completion of the Crater Floor exploration, it is still some debate

regarding the origin and geological relationships between the surface exposures. A special issue covers a wide range of instrument observations and studies from this part of the mission (Hand et al., 2022). Some key findings has also been synthesized in Farley et al. (2022), and the remaining of this section will address these. First, it appear that the delta formation is located stratigraphically above the Crater Floor units. This is contrary to the prevailing understanding prior to landing, and it is based on revised interpretation of orbital imagery (Mangold et al., 2020) and initial observations of the contact in rover imagery (Farley et al., 2022). RIMFAX soundings supports this view and do not indicate the presence of the delta deposits below the Crater Floor units (Paige et al., 2022). Furthermore, interpretation of rover high resolution imagery of outcrops along the delta front and on erosional delta remnants, indicate a late stage deposition that initially took place in a steady fluvial regime before transitioning into intermittent floods as the lake system dried out (Mangold et al., 2021).

On the Crater Floor, the Séítah formation (previously called Cf-f-1 in Stack et al. (2020) and Figure 2.3) was confirmed to be the lowest exposed stratigraphic unit, succeeded by the Máaz formation (Cf-fr/Us). From geological surface observations, and detailed geochemical and textural analysis of sample sites with rover payload instruments, the Séítah area was interpreted to be an igneous and coarsely crystalline olivine cumulate (Farley et al., 2022). The orbital carbonaceous signature detected in VNIR imagery (Ehlmann, Mustard, Fassett, et al., 2008; Goudge et al., 2015) was confirmed by in-situ rover observations and hypothesized to be formed by differentiation in a slowly cooling magma or lava. Séítah is finely layered as observed both in surface outcrops and as interpreted in RIMFAX radargrams. However, the stratigraphically highest outcrop in the Séítah exposures that was investigated through remote sensing by the rover (the Content member), is distinct and shows little internal layering and an olivine-poor geochemical signature. The Content member is only exposed over lateral distances of some meters compared to the prevalent layered Séítah outcrops (which belong to the more extensive Bastide member).

Geochemically, the Maaz formation is dominated by augite and plagioclase, and differs from Séítah in being olivine poor. Yet, geochemical and textural analysis are inconclusive in distinguishing the two formations. The Máaz formation is hypotesized to be either (I) a upper less olivine-rich section of the Séítah magma, or (II) a sequence of younger basaltic lava that embayed and partially overtopped the Séítah formation after removal of the putative less mafic complement. The stratigraphically upper Content member of Séítah formation is chemically and textually comparable with the Máaz formation, but its presence can be rationalized just as well in both formation scenarios. Determining the source of the Crater Floor hypothesized lavas or impact melts has not been possible by the surface observations, though the proposed link between Séítah and regional carbonate-exposures is less favorable after in-situ investigation of the Séítah lithologies (Farley et al., 2022).

Based on RIMFAX data, it appears to be an unconformity in the contact on the Eastern side of the Séítah exposure (e.g., Paper IV). This could imply that Máaz is a distinct sequence in accordance with hypothesis II. However,

such a subsurface contact is not apparent on the west side of the exposure (Hamran et al., 2022) and, consequently, the true nature of the contact is not well understood from radar data alone. Therefore, the exact relationship between Séítah and Máaz still remains to be disclosed.

Séítah contain prominent layering at centimeter to meter scale, which may be of magmatic origin. Yet, based on geometries in the radargram along the bondaries of Séítah, Hamran et al. (2022) advocates for not precluding a sedimentary origin, keeping in mind that the chemical and textural analysis are not conclusive. However, the majority of observations and in-detail analysis at sampling sites displays igneous lithologies.

Both Séítah and Máaz appear altered by aqueous solutions, inferred by the geochemical alteration of minerals and precipitation of salts. For example, the orbital VNIR carbonate signature of Séítah was interpreted to be caused by Fe-Mg carbonate along grain boundaries, which suggests in-situ carbonation under low water/rock ratio conditions. However, there is no geochemical or mineralogical indication of extensive open-system aqueous alteration as both formations are consistent with near-pristine igneous composition.

References

Arvidson, R. E. (2016). Aqueous history of mars as inferred from landed mission measurements of rocks, soils, and water ice. *Journal of Geophysical Research: Planets*, vol. 121no. 9, 1602–1626.

Balaram, J., Aung, M., & Golombek, M. P. (2021). The Ingenuity helicopter on the Perseverance rover. *Space Science Reviews*, vol. 217no. 4, 1–11.

Barlow, N. G. et al. (2005). A review of martian impact crater ejecta structures and their implications for target properties. *Large meteorite impacts III*, vol. 384, 433–442.

Bhartia, R., Beegle, L. W., DeFlores, L., et al. (2021). Perseverance's scanning habitable environments with raman and luminescence for organics and chemicals (SHERLOC) investigation. *Space Science Reviews*, vol. 217no. 4, 1–115.

Brown, A. J., Viviano, C. E., & Goudge, T. A. (2020). Olivine-carbonate mineralogy of the Jezero crater region. *Journal of Geophysical Research: Planets*, vol. 125no. 3, e2019JE006011.

Dypvik, H., & Kalleson, E. (2010). Mechanisms of late synimpact to early postimpact crater sedimentation in marine-target impact structures.

Dypvik, H., Gohn, G. S., Edwards, L. E., Horton, J. W., Powars, D. S., & Litwin, R. J. (2018). Chesapeake Bay impact structure—development of "brim" sedimentation in a multilayered marine target.

Ehlmann, B. L., Mustard, J. F., Fassett, C. I., Schon, S. C., Head III, J. W., Des Marais, D. J., Grant, J. A., & Murchie, S. L. (2008). Clay minerals in delta deposits and organic preservation potential on Mars. *Nature Geoscience*, vol. 1no. 6, 355–358.

Ehlmann, B. L., Mustard, J. F., Murchie, S. L., Poulet, F., Bishop, J. L., Brown, A. J., Calvin, W. M., Clark, R. N., Marais, D. J. D., Milliken, R. E., et al. (2008). Orbital identification of carbonate-bearing rocks on Mars. *Science*, vol. 322no. 5909, 1828–1832.

Ehlmann, B. L., Mustard, J. F., Swayze, G. A., Clark, R. N., Bishop, J. L., Poulet, F., Des Marais, D. J., Roach, L. H., Milliken, R. E., Wray, J. J., et al. (2009). Identification of hydrated silicate minerals on Mars using MRO-CRISM: Geologic context near Nili Fossae and implications for aqueous alteration. *Journal of Geophysical Research: Planets*, vol. 114no. E2.

Farley, K. A., Stack, K. M., Shuster, D. L., et al. (2022). Aqueously altered igneous rocks sampled on the floor of Jezero crater, Mars. *Science*, vol. 0no. 0, eabo2196.

Farley, K. A., Williford, K. H., Stack, K. M., et al. (2020). Mars 2020 mission overview. *Space Science Reviews*, vol. 216no. 8, 1–41.

Fassett, C. I., & Head, J. W. (2005). Fluvial sedimentary deposits on Mars: Ancient deltas in a crater lake in the Nili Fossae region. *Geophysical Research Letters*, vol. 32no. 14.

Fassett, C. I., & Head, J. W. (2008). The timing of Martian valley network activity: Constraints from buffered crater counting. *Icarus*, vol. 195no. 1, 61–89.

Fassett, C. I., & Head, J. W. (2011). Sequence and timing of conditions on early Mars. *Icarus*, vol. 211no. 2, 1204–1214.

Garvin, J., Sakimoto, S., & Frawley, J. (2003). Craters on Mars: Global geometric properties from gridded MOLA topography. *Sixth International Conference on Mars*.

Goudge, T. A., Milliken, R. E., Head, J. W., Mustard, J. F., & Fassett, C. I. (2017). Sedimentological evidence for a deltaic origin of the western fan deposit in Jezero crater, Mars and implications for future exploration. *Earth and Planetary Science Letters*, vol. 458, 357–365.

Goudge, T. A., Mustard, J. F., Head, J. W., & Fassett, C. I. (2012). Constraints on the history of open-basin lakes on Mars from the composition and timing of volcanic resurfacing. *Journal of Geophysical Research: Planets*, vol. 117no. E12.

Goudge, T. A., Mustard, J. F., Head, J. W., Fassett, C. I., & Wiseman, S. M. (2015). Assessing the mineralogy of the watershed and fan deposits of the Jezero crater paleolake system, Mars. *Journal of Geophysical Research: Planets*, vol. 120no. 4, 775–808.

Grotzinger, J. P., Sumner, D. Y., Kah, L., et al. (2014). A habitable fluvio-lacustrine environment at yellowknife bay, gale crater, mars. *Science*, vol. 343no. 6169, 1242777.

Hamran, S.-E., Paige, D. A., Allwood, A., et al. (2022). Ground penetrating radar observations of subsurface structures in the floor of jezero crater, mars. *Science Advances*, vol. 8no. 34, eabp8564.

Hand, K., Sun, V. Z., Simon, J. I., Cohen, B. A., Hickman-Lewis, K., Guzewich, S., & Spiga, A. (Eds.). (2022). The Mars Perseverance Rover Jezero Crater Floor Campaign [Special issue]. American Geophysical Union.

Hiesinger, H., & Head, J. (2004). The Syrtis Major volcanic province, Mars: Synthesis from Mars global surveyor data. *Journal of Geophysical Research: Planets*, vol. 109no. E1.

Horgan, B. H., Anderson, R. B., Dromart, G., Amador, E. S., & Rice, M. S. (2020). The mineral diversity of Jezero crater: Evidence for possible lacustrine carbonates on Mars. *Icarus*, vol. 339, 113526.

Lillis, R. J., Robbins, S., Manga, M., Halekas, J. S., & Frey, H. V. (2013). Time history of the Martian dynamo from crater magnetic field analysis. *Journal of Geophysical Research: Planets*, vol. 118no. 7, 1488–1511.

Mangold, N., Gupta, S., Gasnault, O., Dromart, G., Tarnas, J., Sholes, S., Horgan, B., Quantin-Nataf, C., Brown, A., Le Mouélic, S., et al. (2021). Perseverance rover reveals an ancient delta-lake system and flood deposits at Jezero crater, Mars. *Science*, vol. 374no. 6568, 711–717.

Mangold, N., Dromart, G., Ansan, V., Salese, F., Kleinhans, M. G., Massé, M., Quantin-Nataf, C., & Stack, K. M. (2020). Fluvial regimes, morphometry, and age of Jezero crater paleolake inlet valleys and their exobiological significance for the 2020 rover mission landing site. *Astrobiology*, vol. 20no. 8, 994–1013.

Mustard, J., Ehlmann, B., Murchie, S., Poulet, F., Mangold, N., Head, J., Bibring, J.-P., & Roach, L. (2009). Composition, morphology, and stratigraphy of Noachian crust around the Isidis basin. *Journal of Geophysical Research: Planets*, vol. 114no. E2.

Mustard, J., Poulet, F., Head, J., Mangold, N., Bibring, J.-P., Pelkey, S., Fassett, C., Langevin, Y., & Neukum, G. (2007). Mineralogy of the Nili Fossae region with OMEGA/MarsExpress data: 1. Ancient impact melt in the Isidis Basin and implications for the transition from the Noachian to Hesperian. *Journal of Geophysical Research: Planets*, vol. 112no. E8.

Paige, D. A., Hamran, S.-E., Amundsen, H. E. F., & other. (2022). Mars Perseverance RIMFAX Ground Penetrating Radar Stratigraphy of the Jezero Crater Delta / Crater Floor Contact. *Presented at AGU Fall Meeting 2022, Chicago, IL, USA*.

Poulet, F., Bibring, J.-P., Mustard, J., Gendrin, A., Mangold, N., Langevin, Y., Arvidson, R., Gondet, B., & Gomez, C. (2005). Phyllosilicates on Mars and implications for early Martian climate. *Nature*, vol. 438no. 7068, 623–627.

Ruff, S. (2017). Investigating the floor of paleolake Jezero by way of Gusev crater. *Fourth International Conference on Early Mars: Geologic, Hydrologic, and Climatic Evolution and the Implications for Life*, vol. 2014, 3076.

Schon, S. C., Head, J. W., & Fassett, C. I. (2012). An overfilled lacustrine system and progradational delta in Jezero crater, Mars: Implications for Noachian climate. *Planetary and Space Science*, vol. 67no. 1, 28–45.

Shahrzad, S., Kinch, K. M., Goudge, T. A., Fassett, C. I., Needham, D. H., Quantin-Nataf, C., & Knudsen, C. P. (2019). Crater statistics on the dark-toned, mafic floor unit in Jezero crater, Mars. *Geophysical Research Letters*, vol. 46no. 5, 2408–2416.

Stack, K. M., Williams, N. R., Calef, F., Sun, V. Z., Williford, K. H., Farley, K. A., Eide, S., Flannery, D., Hughes, C., Jacob, S. R., et al. (2020). Photogeologic map of the perseverance rover field site in Jezero crater constructed by the Mars 2020 Science Team. *Space science reviews*, vol. 216no. 8, 1–47.

Sun, V., & Stack, K. (2019). Understanding the continuity of regional units in the Mars 2020 Jezero and Northeast Syrtis regions: Implications for the origin of the mafic unit (s). *50th Annual Lunar and Planetary Science Conference*, no. 2132, 2271.

Werner, S. (2008). The early Martian evolution—constraints from basin formation ages. *Icarus*, vol. 195no. 1, 45–60.

Chapter 3

Radar Imager for Mars' subsurFAce eXperiment (RIMFAX)

Concepts and theory regarding ground-penetrating radar (GPR) data acquisition with RIMFAX is reviewed in this chapter. These are fundamental topics of the peer-reviewed papers in this thesis, and consequently require some attention. See Hamran et al. (2020) for a detailed description of the RIMFAX instrument, its operation and scientific objectives. On Mars, a variety of measurements are conducted, but the present thesis is focused on sounding while traversing to generate 2D-images, i.e. radargrams, along the rover path. Figure 3.1 is an artistic illustration of instrument operation while the Perseverance rover is driving. First results from imaging the Martian subsurface are presented in Hamran et al. (2022).

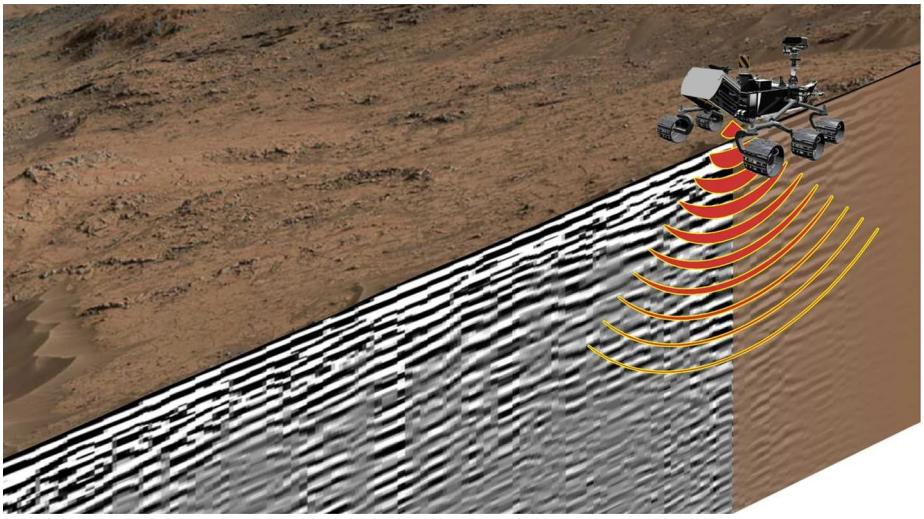

Figure 3.1: Artistic illustration of RIMFAX data acquisition while the Perseverance rover is driving (Hamran et al., 2020). The subsurface is imaged by consecutive radar soundings in order to generate a 2D radargram profile.

3.1 Signal acquisition

RIMFAX is an ultra-wideband (UWB), gated, and frequency modulated continuous wave (FMCW) radar. UWB essentially means a large bandwidth

compared to the center frequency that has proven useful for GPR imaging (e.g., Hamran, 2010). RIMFAX' bandwidth span the 150 - 1200 MHz frequency range, and enable imaging and detection of subsurface features at meter to centimeter scales. Gating describes the monostatic instrument design for alternating, simultaneous transmission and reception with a single antenna. FMCW is a standard radar sounding technique, where a continuous wave is transmitted while the instantaneous frequency is being modulated over time. This technique enables a combination of high power output for increased range detection and wide bandwidth for fine range resolution. Figure 3.2 displays a schematic block diagram of the RIMFAX instrument.

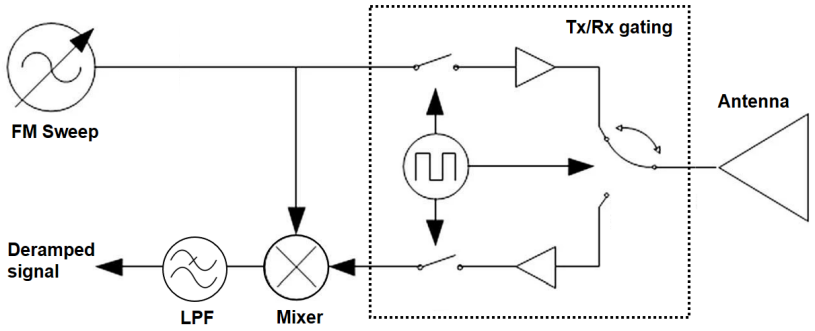

Figure 3.2: Block diagram of the RIMFAX instrument design. The resultant deramped signal is equal a low-pass filtered mixer output. Figure modified from Hamran et al. (2020).

RIMFAX employs a stretch processing receiver which ideally approximates the response of a matched filter receiver (Keel et al., 2012), but obtained through a series of operations to output the compressed results. Paper II gives a thorough review of the signal acquisition and processing steps involved. Put briefly: at reception, a received signal is multiplied with a copy of the transmitted waveform in the mixer, and subsequently passed through a low-pass filter (LPF) to obtain the deramped signal. In RIMFAX, the LPF is implemented digitally in the electronics unit. The frequency content of this signal F_B is denoted beat-frequency and can be linearly related to a target's range R:

$$F_B = \frac{2B}{v\tau} R\,, \tag{3.1}$$

where v is the propagation velocity, B the signal bandwidth, and τ the sweep time duration. This principle is illustrated in Figure 3.3 for a single reflection.

By conducting, e.g., a Fast Fourier Transform (FFT) on the deramped signal, a complex-valued signal is obtained that is effectively the compressed response in two-way travel time or range. For products of the sweep-length and bandwidth larger than 10 ($\tau B > 10$), a single target response would approximate a sinc-function after transformation for an ideal boxcar frequency spectra (Cook & Bernfeld, 1993).

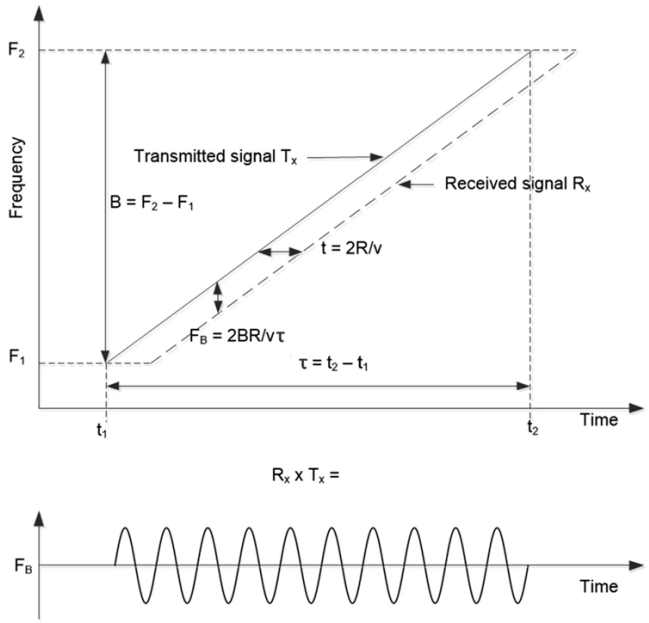

Figure 3.3: Illustration of stretch processing and beat-frequency for a single reflection, where the reflected signal is a time-delayed copy of the transmitted waveform (Hamran et al., 2020).

An amplitude taper window function is commonly used to reduce sidelobes in the target response at the cost of a wider main lobe and reduced range resolution, in addition to reduction in signal-to-noise ratio (SNR). Depending on the desired imaging qualities or aim of the analysis, an appropriate amplitude taper is selected. Due to the stretch processing receiver only approximates a matched filter response, sidelobe-response can be degraded for low τB-products. However, Cook and Bernfeld (1993) states that for $\tau B > 100$, the sidelobes are close to that of the taper's expected performance. A comparison between an untapered and tapered target response is presented in Figure 3.4. For RIMFAX, the τB-product ranges between 10^5-10^8, depending on the operation mode (Hamran et al., 2020).

The range resolution δR describes the finest resolution in a radar image. For a rectangular pulse, the effective length of the received signal at its -3dB level can be expressed as:

$$\delta R = \frac{v}{2B}\,, \tag{3.2}$$

where v is the propagation velocity and B the radar bandwidth. In practice, the exact range resolution, e.g. defined as the mainlobe width at -3dB or -6dB, is a bit more complicated and also depends on the amplitude taper used in processing. Furthermore, as noted by Daniels (1999), detection and resolution in GPR sounding is highly affected by the conductive subsurface media; sidelobes

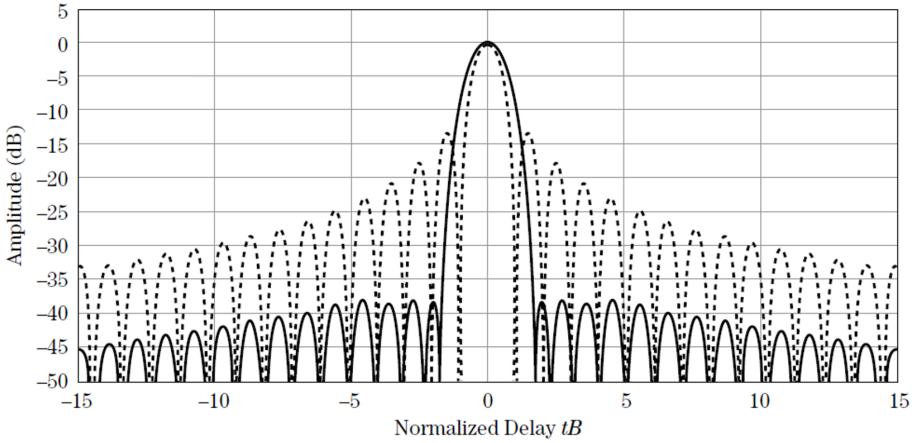

Figure 3.4: Ideal target responses of for a untapered (dashed line) and tapered (solid line) matched filter FMCW signal. Figure from Keel et al. (2010).

of stronger reflections can conceal weaker ones and waveforms broadens with propagation distance due to attenuation.

For monostatic sounding with a single antenna, gating is used to switch connection to the antenna between the transmission and reception circuits. The choice of waveform sweep length and gating window will determine the instrumented range, i.e. at what range the radar will be imaging. Gating is also an efficient way to remove unwanted strong reflections and corresponding sidelobes, like e.g. the surface reflection for an air-coupled GPR (Hamran et al., 1995). Another application can be found in through-the-wall imaging where gating is beneficial for removing the dominant wall reflections that enables detection of weaker reflections from targets in the neighbouring room (Fioranelli et al., 2015). The response of the gating results in a triangular output, Figure 3.5. Though this will alter the power in the recorded signal, the true power can be recovered by multiplying with the reciprocal triangular-shaped window at the cost of reduced signal-to-noise ratio where the signal is amplified.

3.1.1 Modes of operation

There are three nominal modes of operation used during rover traverses, which are the focus of Paper I-IV. RIMFAX conducts multiple soundings in groups at 10 cm intervals, giving separate 2D-images along track. Each mode has a different receiver window and instrumented range, designed to capture data from different depths. It is also possible to configure radar parameters in order to optimize data collection for different subsurface conditions, but that is not within the scope of this thesis. The 3 nominal modes are summarized in Table 3.1:

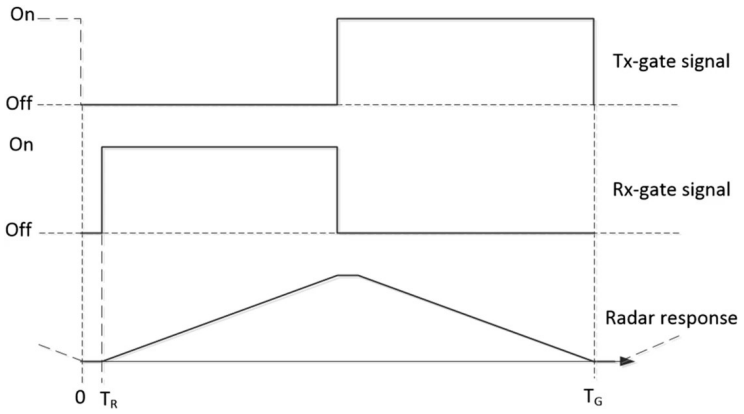

Figure 3.5: Radar response from gating in RIMFAX (Hamran et al., 2020).

Mode	Bandwidth	Receiver window
Surface	150-1200 MHz	The antenna reflection, surface reflection and very upper subsurface (down to ∼6m depth).
Shallow	150-1200 MHz	The surface reflection and shallow subsurface (down to ∼8m depth).
Deep	150-600 MHz	Reflections from the upper subsurface (∼1m depth) through the instrumented range. Depending on configured sweep time, instrumented range vary from 5.4 m to 974 m in free space (0.3 m/ns) and 1.7 m to 308 m in subsurface with propagation velocity of 0.1 m/ns. The deep mode was designed to image down to depths of beyond 10 m, but actual penetration depends on propagation velocity and attenuation in the subsurface media.

Table 3.1: List of nominal RIMFAX acquisition modes while driving.

3.2 Radargram generation

After signal acquisition, consecutive recordings are subsequently stacked horizontally and a series of additional operations are applied in order to obtain a fully processed radargram. Background removal (BGR) is among the more central processing steps, and can be applied on either the deramped signal before FFT, or afterwards on the radargram. BGR attempts to eliminate ringing in the recordings, a dominant type of coherent noise in GPR data that can completely mask geological structures in the radargram. For RIMFAX it can typically come from reflections between antenna and ground, or antenna and rover body. But the noise can also come from, e.g. reflections between electronics box and calibration cable or from other electromagnetic rover noise (Gonzales et al., 2017). Typical BGR techniques include subtracting the average or moving-average trace value from each individual trace in the deramped signal or radargram. There are also more sophisticated methods based on singular value decomposition (Kim et al., 2007) or wavelet transform filtering (Tronicke et al., 2020).

Figure 3.6 displays a shallow mode recording and the central processing steps in order to generate a 2D radargram. The BGR causes a -10 dB drop in the signal power from (a, b) to (c, d), showing how the recorded data is heavily dominated by ringing. The effect of amplitude tapering is shown in (e, f), and after a FFT the 2D radargram is generated in (e). Noise appears at 175 ns ($\sim$7.5 m depth) around the instrumented range of the recording. Additional techniques for enhancing RIMFAX' deramped recording is discussed in Paper III. There are also several additional steps that can be included in radargram generation depending on the aim of the analysis or imaging task.

The elevation difference along track can be substantial over a radargram profile, and lead to geometrical distortion of subsurface reflections. To account for this, traces are adjusted vertically according to the elevation. If the vertical axis of the radargram is in two-way travel time (TWT), a subsurface velocity needs to be assumed in order for the elevation (in meter) to be consistent with subsurface structures (in TWT). In GPR data, the subsurface velocity is usually assumed a constant in lack of more accurate estimates. Figure 3.7 shows the RIMFAX radargram after applied time-zero and topography corrections.

3.3 Monostatic 2D-imaging

A fundamental challenge with monostatic subsurface imaging, utilizing the same antenna for both transmission and reception, is the lack of geometric constraint on subsurface layering and features. Back-scattered reflections from the surface and subsurface in 3D will be collapsed into a single time series, considered to be representative of the 1D-subsurface in nadir direction. By stacking consecutive soundings next to one-another, a 2D profile is generated. A simple scenario is illustrated in Figure 3.8 (a, b) where the along-track geometric effects of collapsing 2D measurements into 1D is apparent. For real world sounding, 3D effects would also include variations in cross-track direction.

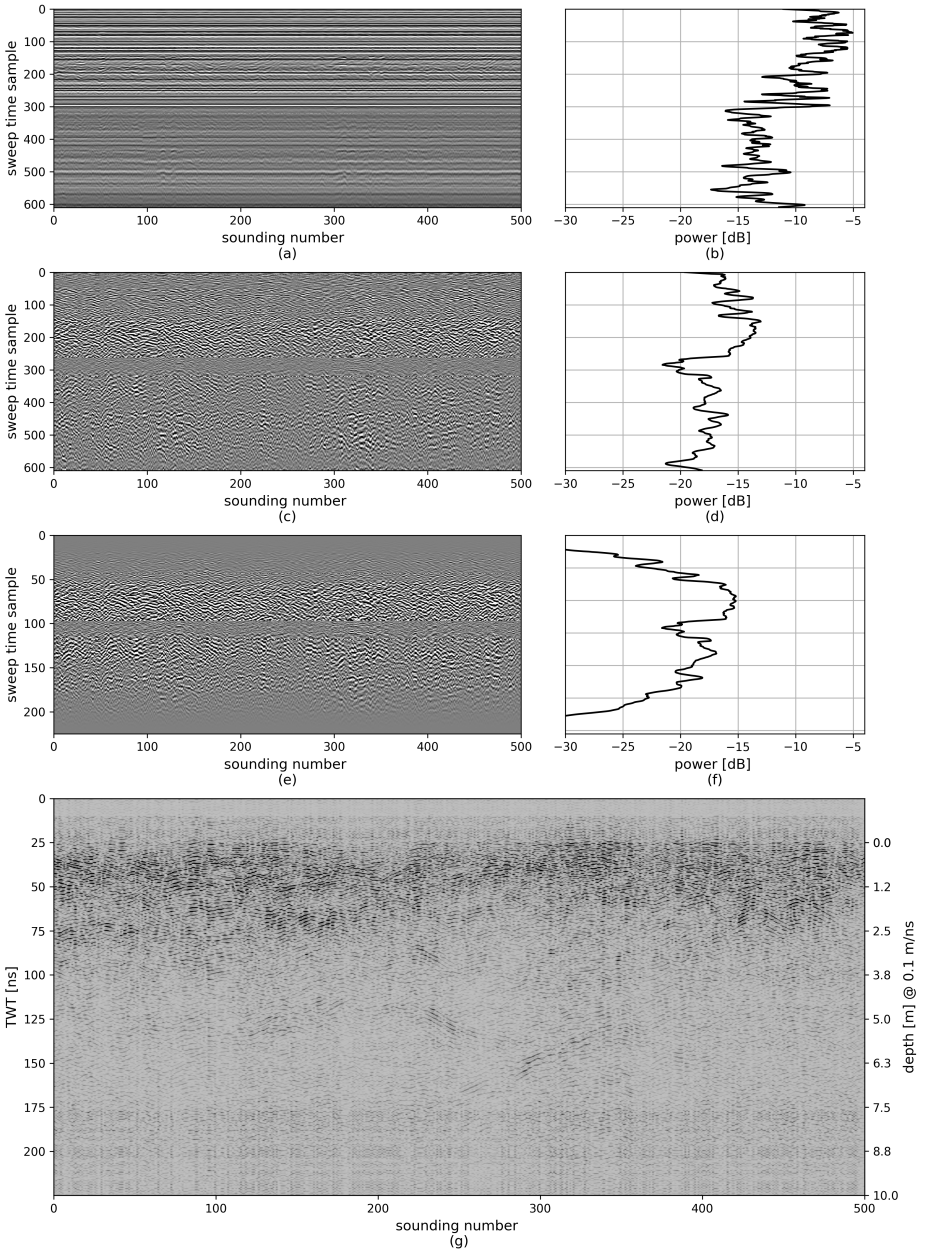

Figure 3.6: Central processing steps of RIMFAX' shallow mode from the last 50 m (500 soundings) from sol 135. (a) Deramped signal and (b) average power. (c) Deramped signal after BGR and (d) average power. (e) Deramped signal after BGR and amplitude tapering, and (f) average power. In (a-f) the vertical axis show the 'sweep time sample' number, i.e. the samples from recording the deramped signal at the output of the stretch-processing receiver. (g) Radargam after FFT. Gain added for visualization.

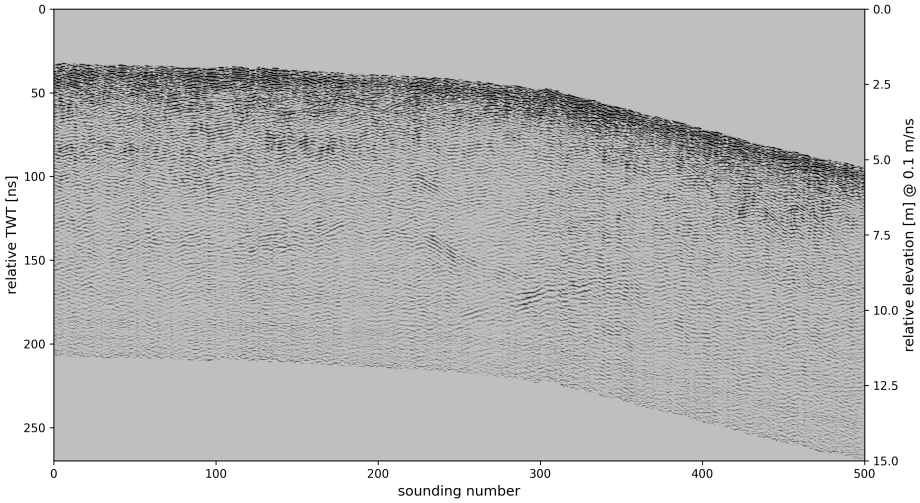

Figure 3.7: Radargram from last 50 meters of sol 135, after time-zero and topography corrections. Gain added for visualization.

Inversion studies are in general not well suited for analysing monostatic radar systems. Due to low geometrical constraint on the subsurface, inversion is an ill-posed problem with non-unique results. Despite a monostatic radar's relatively simple imaging capacity of geometric structures compared to e.g. GPR array systems, manual interpretation can still be very insightful (Hamran et al., 2022) and certain kinematic aspects like subsurface velocity by hyperbola detection is possible (Casademont et al., 2023). Monostatic radars are also very suitable for analysing the spectral response (Paper II and III), and it can also be possible to retrieve returned power estimates (Section 3.5.1).

In an unmigrated 2D radargram, dip of reflections will be underestimated while syncline and anticline features will be out of focus. Monostatic imaging can be improved by applying time-domain 'zero-offset' migration techniques by moving reflections to their correct place in a 2D-sense along the profile, and collapsing diffraction hyperbolas to points.

There are numerous migration techniques available for distinct applications (Yilmaz, 2001); for example, Kirchhoff diffraction-stack migration where summation of equal travel times is done for each point in the radargram, and Stolt migration based on frequency-wavenumber transformation and manipulation. These techniques assumes a constant velocity in the subsurface, and trace back reflection or diffraction energy to the source location along the profile. For RIMFAX with a air-coupled antenna elevated off the ground, the migration algorithm also needs to incorporate a layered velocity model to account for the air-layer and refraction at the surface. This can be achieved by, e.g., a downward continuation migration scheme (Claerbout & Doherty, 1972). Figure 3.8 (c) shows improved imaging of the synthetic data from downward continuation by

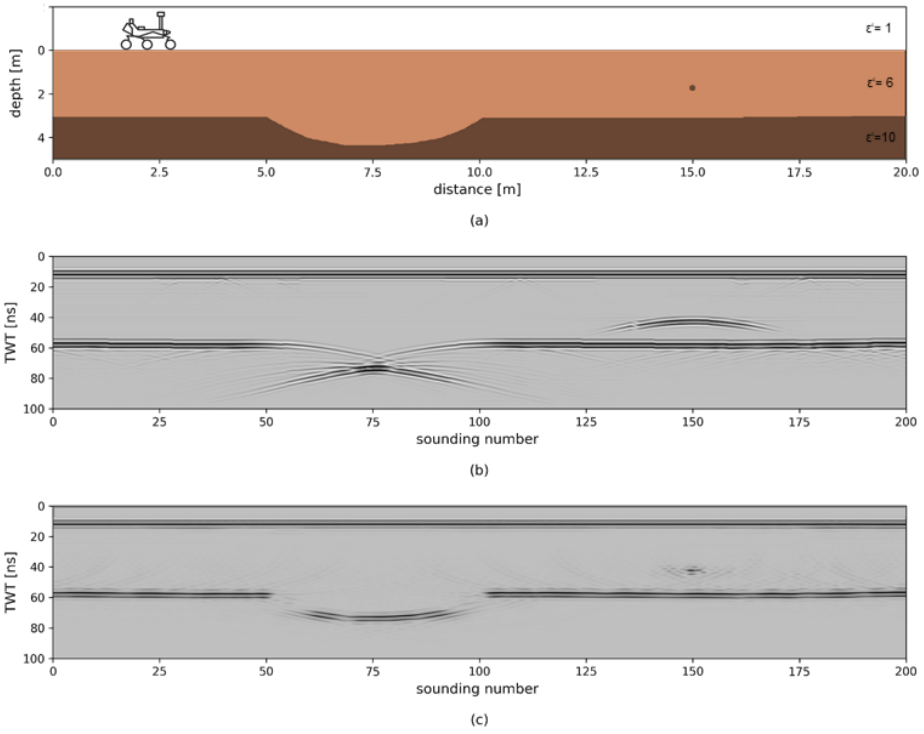

Figure 3.8: Illustration of monostatic sounding and 2D imaging of subsurface structures. (a) Subsurface is a 2-layered model with a concave structure at 3-4 m depth, 5-10 m along the profile, and a point scatterer at 2 m depth, at 15 m along the profile. Upper layer resembles air, from where the air-coupled antenna is located. (b) Synthetic radargram, where distortion of geometry in the radar image is apparent. Simulations were conducted with gprMax (Warren et al., 2016) and waveform compression equals RIMFAX' deep mode with a hamming window amplitude taper (Paper II). (c) Image enhancement of synthetic radargram after applied migration.

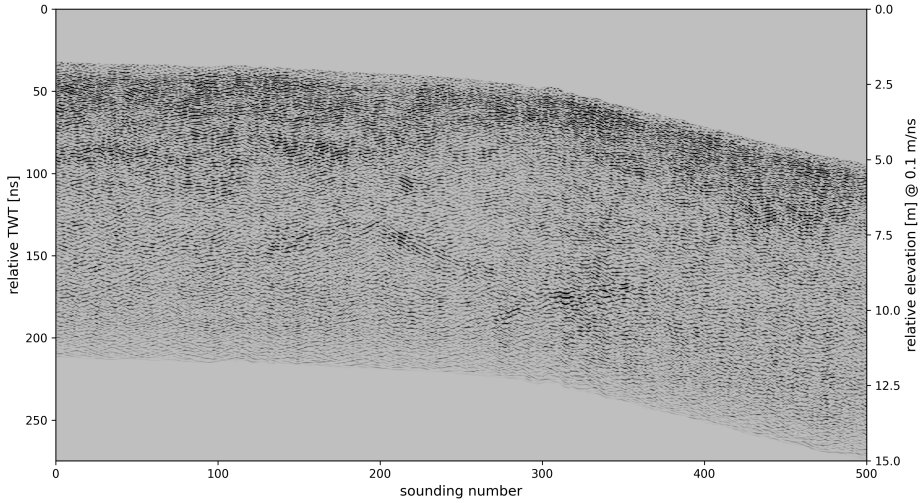

Figure 3.9: Improved imaging of RIMFAX shallow mode from sol 135 with zero-offset radargram migration.

finite-difference for solving the one-way scalar wave equation. Alternatively, this could also be obtained by, e.g., wave equation migration with the Phase-Shift Method (Gazdag, 1978), where downward continuation is achieved by applying a phase-shift operator at vertical steps over the radargram. In Figure 3.9, migration has been applied to the shallow mode RIMFAX radargram from sol 135. Even after applied migration only subtle changes are observed, illustrating some of the challenges with interpreting subsurface structures in RIMFAX data acquired during the Crater Floor campaign. The data do not contain meter-long individual and coherent reflections as in, e.g., the idealized synthetic example in Figure 3.8.

3.4 Displaying radargram profiles

Prior to landing, it was recognized beneficial to link RIMFAX soundings with orbital and rover imagery of the surface. Later, after surface operation had started, the wiggly rover path with both abrupt turning at decimeter scale and windy curves over 10s of meters, made the need for such correlation even more apparent.

In this thesis, a major effort was done in order to achieve a good 3D GIS display of RIMFAX radargrams together with imagery of the surface. RIMFAX data need to be reformatted, e.g. into SEG-Y data format, for import into external software. Ground Model plug-in for ArcGIS[1] is one geophysical software able to display radargram in 3D together with imagery of the surface. In

[1]Ground Model plug-in for ArcGIS is proprietary software provided by Geocap AS.

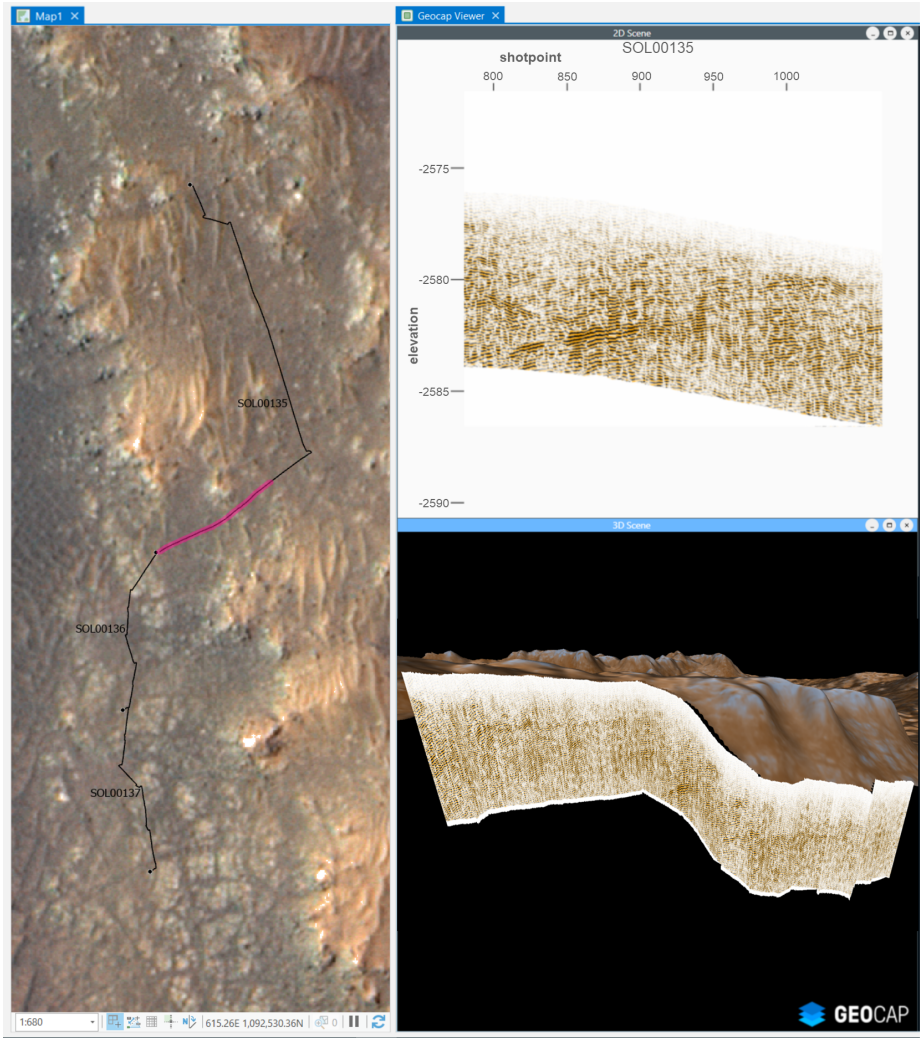

Figure 3.10: RIMFAX 3D GIS view from sols 135 to 137, displayed with Ground Model plug-in for ArcGIS. Left window frame is a 2D GIS map with rover navigation in black. Basemap is a Mars 2020 Science Team RGB-colored HiRISE mosaic. A 2D radargram profile with data from RIMFAX deep mode is displayed in the upper right window frame, according to highlighted (purple) selection in the map (last 25 meters of sol 135). Lower right window frame shows sols 135 to 137 radargram projected in 3D together with the DEM and HiRISE false-colored mosaic. Vertical exaggeration = 10.

Figure 3.10, radargram are displayed together with a digital elevation model (DEM) and imagery of the surface. With such display capabilities, it is possible to visually correlate reflections in the radargram with surface outcrops. For example, as the rover descended down the slope from a couple of meters tall escarpment, RIMFAX imaged strong dipping reflections in the subsurface (towards the end of sol 135) that are likely cropping out in the lower lying parts of the terrain.

3.5 Quantitative analysis

Interpretation of radargram features can can be done by mapping laterally extent reflections and patterns of smaller-scale radargram facies. Quantitative analysis, on the contrary, evaluates the recorded signal with a number of techniques in order to extract certain medium parameters. So even with a relatively low geometric constraint on imaging due to monostatic sounding, the data still contain a wealth of information. For example, in Casademont et al. (2023) the permittivity is determined from diffraction hyperbola fitting, and related to subsurface parameters. In Paper IV reflection geometry is analyzed for quantification of reflector orientation. This section will review RIMFAX power analysis and spectral time-frequency analysis of attenuation in subsurface media.

3.5.1 Returned power analysis

Returned power estimates for radar sounding is obtained through the well-established radar equation. This can be adapted for detection of plane surface targets with Fresnel reflectivity, by assuming a plane wave approximation for a nadir looking radar with a narrow beam (Ulaby & Long, 2014, pp. 325–336):

$$\frac{P_r}{P_t} = \frac{G^2\lambda^2}{(4\pi)^2\, 4(h_0+\tilde{z})^2}\Upsilon^2\, e^{-4(\alpha+\kappa)z}\,\Gamma\,. \tag{3.3}$$

The equation is written in terms of a monostatic GPR with an air-coupled antenna elevated off the ground, and assumes plane-wave, far-field propagation. Variables are listed in Table 3.2. Though GPR-sounding is typically not narrow-beam, the approximation has shown to work well for evaluating the returned power at the center frequency of a UWB waveform (Paper I).

Also accounted for in Equation (3.3) is refraction at the surface for an air-coupled GPR antenna elevated off the ground. The high permittivity contrast between air and the surface refracts wave-fronts inwards and concentrates the power density in nadir direction, and consequentially generates a depth dependent gain. The geometrical spreading loss will therefore be altered, which is accounted for by correction to the depth of target, $\tilde{z}$. For a negligible refraction gain, $\tilde{z} = z$. Based on optical theory, Bogorodsky et al. (1985) provides an expression for this effect in nadir direction, which results in $\tilde{z} = z/\sqrt{\epsilon'}$ for a homogeneous subsurface velocity. ε' is the permittivity in the subsurface. This is effectively the same as used to account for divergence loss for outwards refracting acoustic waves in marine seismic acquisition (Newman, 1973). However, seismic often

Variable	Description
P_r	Received power
P_t	Transmitted power
λ	Wavelength (according to center frequency)
G	Antenna gain in nadir direction
h_0	Antenna elevation
z	Target depth
$\tilde{z}$	Apparent target depth from geometrical correction
ε'	Subsurface dielectric constant
Υ	Surface transmissivity
α	Intrinsic (dielectric) attenuation
κ	Volume scattering attenuation
Γ	The target's Fresnel reflectivity

Table 3.2: List of radar equation variables.

employ an empirical geometrical correction term that deviates slightly from the optical solution (Yilmaz, 2001). For RIMFAX and the geometrically corrected apparent depth $\tilde{z}$, it is still necessary to determine whether the optical far-field solution is applicable, or if near-field effects are dominating in the region below the 0.6-0.7 m antenna elevation.

There are numerous parameters involved in describing a radar system. So far, the antenna gain has been considered a single scalar quantity, but there are several additional factors contributing the the radar system's gain. For example, pulse compression of FMCW signals leads to a pulse compression gain τB (Keel et al., 2010), where τ is the sweep length and B is the bandwidth. Integrating several identical soundings will increase signal-to-noise ratio (SNR) and consequently increase the dynamic range of the radar system.

Hamran (2010) presents a simple way of separating the radar system from media dependent propagation effects, by introducing the system dynamic range (SDR) parameter in the radar equation. SDR describes the total range of a system, i.e. the lowest signal strength a received signal can have and still be detected (Figure 3.11). We then rewrite Equation (3.3) in more general terms with the help of the SNR and SDR:

$$SNR \approx SDR \times \frac{\lambda^2}{(4\pi)^2\, 4(h_0 + \tilde{z})^2} \times \Upsilon^2\, e^{-4(\alpha+\kappa)z}\, \Gamma\,. \tag{3.4}$$

The equation can now be used to calculate the received power for a radar system by including a single estimate of the total SDR. An illustration of the SDR for each RIMFAX mode is presented in Figure 3.12. For RIMFAX' deep mode, the approximate total SDR is 160 dB including all antenna, receiver and processing gains (Hamran et al., 2020). Employing the equation can then facilitate analysis to focus exclusively on subsurface parameters like Υ, α, κ and Γ. For example, detection limits can be studied by setting SNR=1 and estimating maximum penetration depths of a radar system (Paper I).

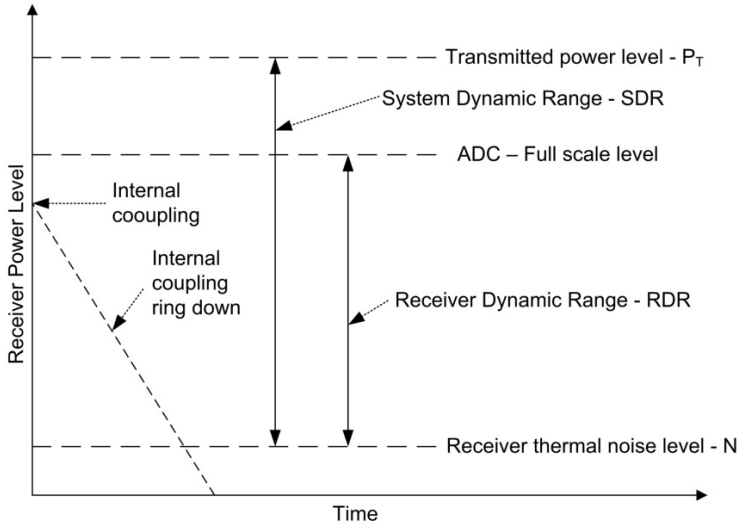

Figure 3.11: Schematic illustration of a radar's SDR. Figure from Hamran (2010).

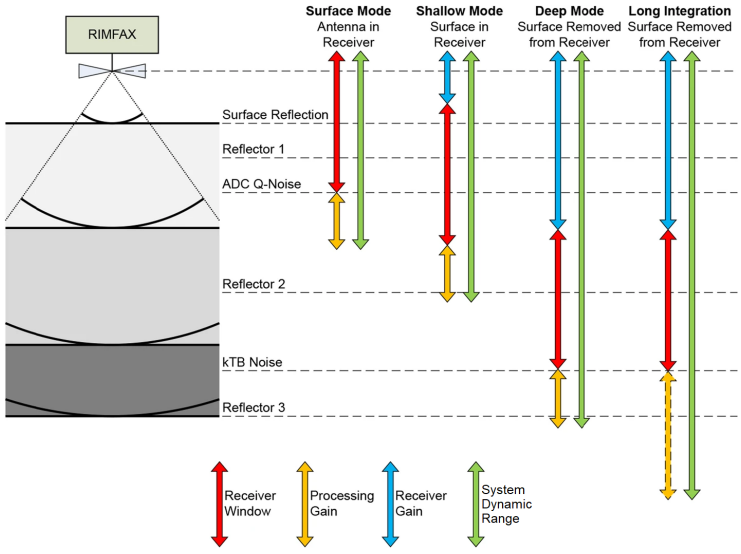

Figure 3.12: Schematic illustration of a RIMFAX' SDR for the different modes. Figure from Hamran et al. (2020).

In order to analyse returned power in acquired RIMFAX data, the gain effects due to gating needs to be accounted for (see Figure 3.5). In Figure 3.13 (a) the gating function is displayed and in (b) is the integrated power estimates of the radargram from sol 135. Gating corrections are done by multiplication with the reciprocal of the gating response. Since RIMFAX is presently not a calibrated radar, with neither the transmitted signal or surface reflection well constrained, it is not possibly to study the whole SDR. However, relative differences can be analysed over an interval, approximating the combined dielectric and scattering attenuation ($\alpha + \kappa$) by a constant-Q model (see also Section 4.1).

There are numerous analysis techniques that can be used to retrieve the Q-parameter when characterizing subsurface attenuation (e.g., Tonn, 1991). Employing the 'amplitude decay' method, the Q-value is determined in the following manner:

$$Q = \pi f_c \Delta t_{twt} \left[\ln \frac{A_1}{A_2} \right]^{-1} . \tag{3.5}$$

f_c is the central frequency and Δt_{twt} is the TWT interval. A_1 and A_2 are the amplitudes at times t_1 and t_2, corresponding to the start and end of the interval. Amplitudes have been corrected for geometrical spreading, in addition to gating. In Figure 3.13 (c) the amplitudes are plotted in dotted line before geometrical correction, and solid line after. In this example, $1/(2\tilde{z})$ was used with $\tilde{z}$=z, assuming the refraction gain is negligible. The returned power analysis quantifies the attenuation to Q=70.3.

3.5.2 Spectral analysis

The spectral content of a received signal $Y(\omega)$ is determined by the emitted waveform $W(\omega)$, instrument characteristics $I(\omega)$, and the ground response $R(\omega)$. The variables are in frequency domain and ω is the angular frequency. In attenuating media, the ground response can be described as the product of the ground's attenuation filter $H(\omega, t_i)$ and the reflectivity series $R_\delta(\omega)$ (Margrave, 1998).

$$Y(\omega) = W(\omega)I(\omega)R(\omega) = W(\omega)I(\omega)R_\delta(\omega)H(\omega, t_i) . \tag{3.6}$$

The amount of attenuation by $H(\omega, t_i)$ depends on the travel time in the medium, represented by t_i for the i-th reflection. For practical purposes, the reflectivity series can be considered constant according to geometrical spreading and the reflectivity of the target, $R_\delta(\omega) = R_\delta$. Spectral analysis then aims at determining the ground's attenuation filter which also can be described in terms of the Q-factor:

$$H(\omega, t_i) = \exp\Big(- \frac{\omega t_i}{2Q} \Big) . \tag{3.7}$$

Figure 3.14 presents the time-frequency response from RIMFAX soundings over the last 50 m of sol 135, where constant-Q has been quantified to Q=72.0 according to the 'centroid frequency-shift' method (Quan & Harris, 1997). Based

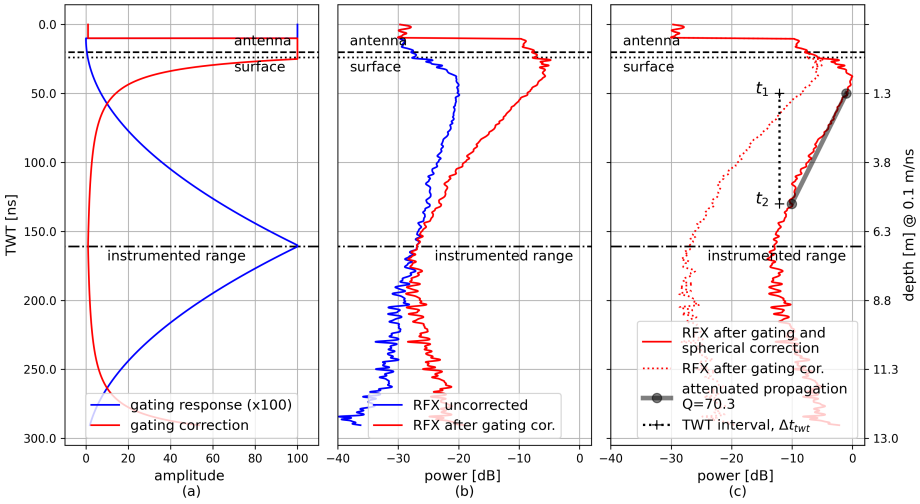

Figure 3.13: Returned power analysis for RIMFAX shallow mode from sol 135. (a) The gating response and the reciprocal correction function. Correction function has a cut off gain at +20dB. (b) Comparison of power in radargram before and after gating correction. (c) Returned power before and after correction of geometrical spreading. Best fit of attenuation for range between t_1 and t_2 equals to a constant-Q media with Q=70.3. The instrumented range is indicated by a dashed-dotted black line.

on analytical relations, the Q-factor is obtained from the slope $\Delta f_c/\Delta t_{twt}$:

$$Q = -C\pi \left[\frac{\Delta f_c}{\Delta t_{twt}} \right]^{-1}, \tag{3.8}$$

where the constant C depends on the waveform shape and bandwidth. For a Gaussian waveform, C equals its variance (in Hz). A thorough study of this technique and quantified attenuation in acquired RIMFAX data, is presented in Paper III.

References

Bogorodsky, V. V., Bentley, C. R., & Gudmandsen, P. (1985). *Radioglaciology* (Vol. 1). Springer Science & Business Media.

Casademont, T. M., Eide, S., Shoemaker, E. S., Liu, Y., Nunes, D. C., Russell, P., Dypvik, H., Amundsen, H. E. F., Berger, T., & Hamran, S.-E. (2023). RIMFAX Ground Penetrating Radar Reveals Dielectric Permittivity and Rock Density of Shallow Martian Subsurface. *Journal of Geophysical Research: Planets*, vol. 128, e2022JE007598.

Claerbout, J. F., & Doherty, S. M. (1972). Downward continuation of moveout-corrected seismograms. *Geophysics*, vol. 37no. 5, 741–768.

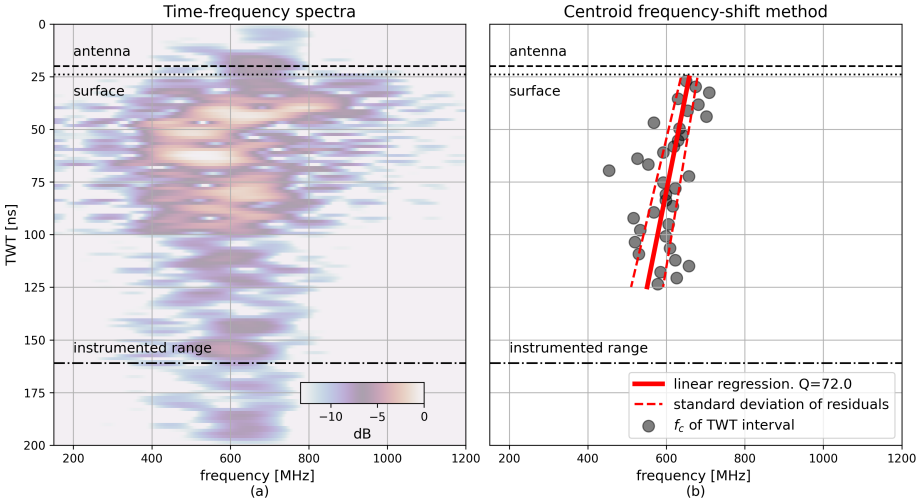

Figure 3.14: (a) Time-frequency plot of RIMFAX shallow mode, integrated over soundings from last 50 m of sol 135. (b) Estimates of centroid frequency shift, with Q=72.0 from linear regression.

Cook, C. E., & Bernfeld, M. (1993). Radar signals. an introduction to theory and application, artech house. *Inc., Boston*.

Daniels, D. (1999). Resolution of ultra-wideband radar signals. *IEE Proceedings-Radar, Sonar and Navigation*, vol. 146no. 4, 189–194.

Fioranelli, F., Salous, S., Ndip, I., & Raimundo, X. (2015). Through-the-wall detection with gated FMCW signals using optimized patch-like and Vivaldi antennas. *IEEE transactions on antennas and propagation*, vol. 63no. 3, 1106–1117.

Gazdag, J. (1978). Wave equation migration with the phase-shift method. *Geophysics*, vol. 43no. 7, 1342–1351.

Gonzales, E., Cordoba, E., & Hamran, S.-E. (2017). Compatibility tests between the mars vehicle system test bed and RIMFAX radar antenna prototype for the Mars 2020 mission. *2017 IEEE International Symposium on Electromagnetic Compatibility & Signal/Power Integrity (EMCSI)*, 44–50.

Hamran, S.-E., Gjessing, D., Hjelmstad, J., & Aarholt, E. (1995). Ground penetrating synthetic pulse radar: Dynamic range and modes of operation. *Journal of Applied Geophysics*, vol. 33no. 1-3, 7–14.

Hamran, S.-E. (2010). Radar performance of ultra wideband waveforms. In G. Kouemou (Ed.), *Radar technology*. IntechOpen.

Hamran, S.-E., Paige, D. A., Allwood, A., et al. (2022). Ground penetrating radar observations of subsurface structures in the floor of jezero crater, mars. *Science Advances*, vol. 8no. 34, eabp8564.

Hamran, S.-E., Paige, D. A., Amundsen, H. E., et al. (2020). Radar imager for Mars' subsurface experiment—RIMFAX. *Space Science Reviews*, vol. 216no. 8, 1–39.

Keel, B., Baden, J., Melvin, W., & Scheer, J. (2012). Advanced pulse compression waveform modulations and techniques. *Principles of modern radar: Advanced techniques* (pp. 19–85). SciTech Publishing.

Keel, B., Richards, M., Scheer, J., & Holm, W. (2010). Fundamentals of pulse compression waveforms. *Principles of modern radar: Basic principles* (pp. 783–793). Scitech publishing.

Kim, J.-H., Cho, S.-J., & Yi, M.-J. (2007). Removal of ringing noise in GPR data by signal processing. *Geosciences Journal*, vol. 11no. 1, 75–81.

Margrave, G. F. (1998). Theory of nonstationary linear filtering in the fourier domain with application to time-variant filtering. *Geophysics*, vol. 63no. 1, 244–259.

Newman, P. (1973). Divergence effects in a layered earth. *Geophysics*, vol. 38no. 3, 481–488.

Quan, Y., & Harris, J. M. (1997). Seismic attenuation tomography using the frequency shift method. *Geophysics*, vol. 62no. 3, 895–905.

Tonn, R. (1991). The determination of the seismic quality factor Q from VSP data: A comparison of different computational methods. *Geophysical Prospecting*, vol. 39no. 1, 1–27.

Tronicke, J., Koyan, P., & Allroggen, N. (2020). The redundant wavelet transform to process and interpret GPR data. *18th International Conference on Ground Penetrating Radar*, 400–403.

Ulaby, F. T., & Long, D. G. (2014). *Microwave radar and radiometric remote sensing* (Vol. 4). University of Michigan Press Ann Arbor, MI, USA.

Warren, C., Giannopoulos, A., & Giannakis, I. (2016). gprMax: Open source software to simulate electromagnetic wave propagation for Ground Penetrating Radar. *Computer Physics Communications*, vol. 209, 163–170.

Yilmaz, Ö. (2001). *Seismic data analysis: Processing, inversion, and interpretation of seismic data*. Society of exploration geophysicists.

Chapter 4

Subsurface Properties and Ground-Penetrating Radar Modeling

This chapter begins with general theoretical and empirical results relevant for GPR sounding in natural terrain, describing the physics of electromagnetic wave propagation in realistic media. The review will help outline which media parameters and insights are possible to extract from RIMFAX measurements, which is at the core of the peer-reviewed papers in this thesis. Thereafter applicability of various computational electromagnetic methods is assessed, based on relevant medium properties and instrument characteristics. Towards the end, the selected modeling approach with finite-difference time-domain is described in more detail.

4.1 Subsurface media properties

Natural media properties relevant for GPR sounding in the ultra high frequency (UHF) range can be divided into dielectric properties, volume scattering losses, and geologic target characteristics. Dielectric effects decide both electromagnetic propagation velocity and energy loss due to water content and chemical constituents in the subsurface. Volume scattering losses accounts for energy reduction in the wavefront by scattering at inhomogeneities in the media, which depends on their size relative to the wavelength. In addition to these propagation effects, reflection at a natural interface is furthermore influenced by change in dielectric properties and the geometry. This section will review theory of related topics as relevant for GPR sounding and modeling.

4.1.1 Dielectric properties

Based on Maxwell's equations, we can derive the homogenous wave equation for the electric field intensity $\mathbf{E}$:

$$\nabla^2 \mathbf{E} - \gamma^2 \mathbf{E} = 0\,, \tag{4.1}$$

where the propagation constant is defined as

$$\gamma^2 = -\omega^2 \mu\, \varepsilon(\omega)\, \varepsilon_0\,. \tag{4.2}$$

ω is the angular frequency, μ the magnetic permeability, $\varepsilon(\omega)$ the complex dielectric constant, and ε_0 the permittivity of free space. A similar expression

can be obtained for the magnetic field intensity, but for brevity we will focus on the electric field intensity.

Since $\varepsilon(\omega)$ is a complex quantity, and therefore also γ, we define the propagation constant in terms of its real and imaginary part:

$$\gamma^2 = \alpha + j\beta\,, \tag{4.3}$$

where

$$\begin{aligned} \alpha &= -\omega\sqrt{\mu\varepsilon_0}\,\Im\Big\{\sqrt{\varepsilon(\omega)}\Big\}\,, \\ \beta &= \omega\sqrt{\mu\varepsilon_0}\,\Re\Big\{\sqrt{\varepsilon(\omega)}\Big\}\,. \end{aligned} \tag{4.4}$$

α and β are denoted the attenuation constant and phase constant, respectively. Magnetic permeability μ is for non-magnetic materials considered a non-dispersive real quantity equal that of free space. In theory, it is a complex quantity that might affect wave propagation in magnetic materials.

An enrichment in magnetic material (magnetite) has indeed been detected on Mars (approximately 2% in the global dust layer and 0.2-0.4% in the crust), which gets Stillman and Olhoeft (2008) to measure the permeability of highly enriched magnetite in the laboratory. They detect a complex permeability, but conclude that the effect on Mars would be negligible for radar soundings because of the relatively low concentrations found there.

Then, for a wave traveling in, e.g., the $\hat{\mathbf{z}}$-direction, a solution to Equation (4.1) is:

$$\mathbf{E}(z) = \hat{\mathbf{x}}E_0 e^{-\gamma z} \;= \hat{\mathbf{x}}E_0 e^{-\alpha z} e^{-j\beta z}\,. \tag{4.5}$$

It appears that the propagation velocity is described by β and the real part of $\varepsilon(\omega)$, while dielectric loss is described by α and the imaginary part of $\varepsilon(\omega)$.

The real part of the complex dielectric constant is called permittivity, and for geological radar studies it is often presumed constant over the frequency range of investigation (Campbell & Ulrichs, 1969). In the lossless case, propagation velocity v is described in terms of ε' and the speed of light c

$$v = \frac{c}{\sqrt{\varepsilon'}}\,. \tag{4.6}$$

Figure 4.1 (a) show how the velocity, and hence permittivity, is approximately constant for low conductivities over the 'GPR plateau' (0.01-1GHz).

With regards to the imaginary part, volume charge densities in a medium can be assumed negligible, so the only current that may exist is due to conduction σ. Then the complex dielectric constant can be expressed as:

$$\varepsilon(\omega) = \varepsilon' - j\varepsilon''(\omega) = \varepsilon' - j\frac{\sigma}{\omega\varepsilon_0}\,. \tag{4.7}$$

Figure 4.1 (b) show how conduction dominate attenuation over the GPR frequency range, and hence the imaginary part of the dielectric constant. Above ∼1 GHz, water relaxation and dipolar effects become dominating. However,

water-related dipolar polarization of bound water in rocks can also become apparent at the lower end of the GPR plateau (e.g., Stillman & Olhoeft, 2008). This can be associated with interfacial Maxwell-Wagner polarization effects. Way above the GPR plateau and not considered in this text, atomic polarization occur.

In general, GPR sounding is particular sensitive to water content (e.g., Ulaby & Long, 2014). For dry rocks though, the permittivity has a large spread in values but there is a strong correlation with density (Campbell & Ulrichs, 1969; Olhoeft & Strangway, 1975; Ulaby et al., 1990). Empirical results from laboratory measurements describing these effects are presented in Figure 4.2.

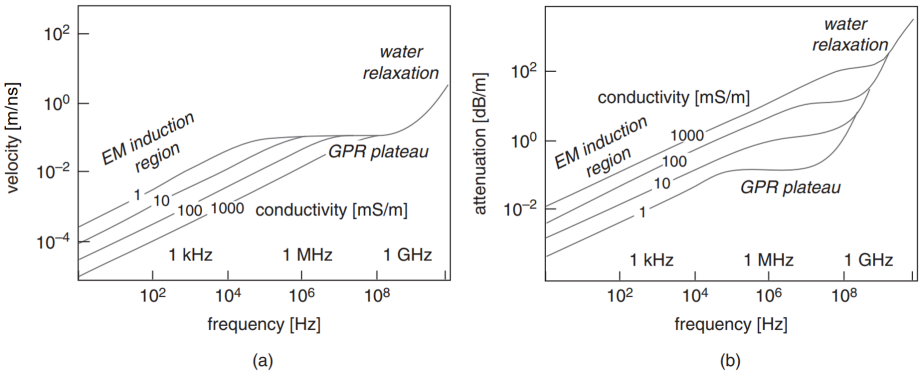

Figure 4.1: General description of the (a) real and (b) imaginary part of the complex dielectric constant, highlighting polarization mechanisms at different frequencies. GPR typically operate in the UHF-range denoted 'GPR plateau' between 1 MHz and 1 GHz. Figure modified from Everett (2013).

Rock physics, as employed in seismic exploration, can predict certain parameters in sedimentary successions based on lithology compaction, including porosity and density (Bjørlykke et al., 2017). This approach is interesting for GPR analysis and discussed in Paper I, with focus on how lower gravity on Mars is expected to influence permittivity and lithological properties. Watters et al. (2017) has also studied this effect in relation to SHARAD sounding.

For the dielectric loss in dry soil and rocks, a less clear correlation is found with lithological properties. However, mineralogy like the oxide constituents Fe_2O_3 and TiO_2, will in general increase the loss of microwaves (Ulaby et al., 1990). This has been widely used for, e.g., interpreting radar losses in the lunar regolith (Carrier et al., 1991; Ding et al., 2020; Xing et al., 2017).

The complex dielectric constant is typically a frequency dependent quantity for both the real and imaginary part. There are several dielectric models used to describe attenuating and dispersive properties in soil and rocks, and two examples are the Cole-Cole and constant-Q models.

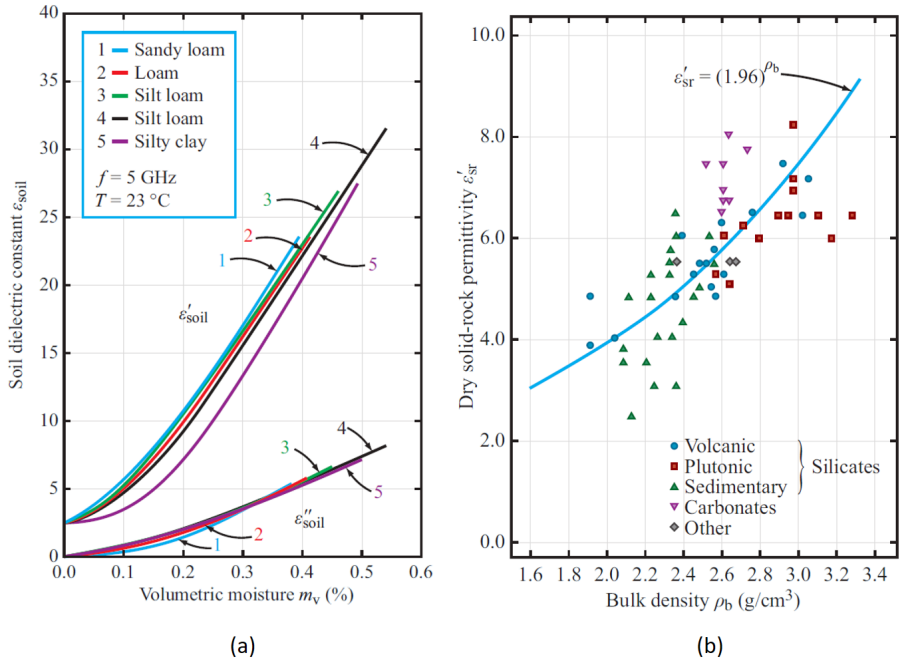

Figure 4.2: (a) Water content's effect on the complex dielectric constant. Measurements for five soils at 5 GHz. (b) Correlation between the permittivity and density for dry rocks. Figures from Ulaby and Long (2014).

4.1.1.1 Cole-Cole Dielectric Model

Cole-Cole models are the most commonly used to describe dielectric relaxation effects in soil and rocks over the UHF range (e.g., Brouet et al., 2019; Stillman & Olhoeft, 2008). There are a variety of other models suitable for specific materials, whereas to describe the dielectric properties of pure freshwater, a single-relaxation Debye model is appropriate, and for saline water, a double-relaxation Debye model (e.g., Ulaby & Long, 2014). A Cole-Cole model, however, accounts for an increased relaxation time of the bound water molecules in the rock mineral matrix, in response to an applied electric field:

$$\varepsilon(\omega) = \varepsilon_\infty + \frac{\varepsilon_s - \varepsilon_\infty}{1 + (i\omega\tau)^{1-\alpha}} \,. \tag{4.8}$$

The relaxation time is represented by τ, while ε_s and ε_∞ are the 'static' and 'infinite frequency' permittivities. The parameter α takes a value between 0 and 1 and describes different spectral shapes, with α=0 reduces the Cole-Cole model to a single-relaxation Debye model. Figure 4.3 (a) presents a couple of Cole-Cole models based on laboratory measurements of rocks.

4.1.1.2 Constant-Q Dielectric Model

Constant-Q was originally used to describe the cumulative attenuating effects for seismic waves (Richards & Aki, 1980), but it has also been found applicable for describing electromagnetic propagation in natural soils and rocks over the GPR frequency range (0.1-1.0 GHz) (Irving & Knight, 2003; Turner & Siggins, 1994). Rather than being an accurate dielectric model for a specific type of medium, constant-Q is a simple description of the approximate bulk attenuating and dispersive effects in natural media, assuming a linear relationship between attenuation and frequency:

$$|\mathbf{E}(z)| = \frac{E_0}{z} \exp\Big(- \frac{\pi z}{\lambda Q} \Big) . \tag{4.9}$$

$|\mathbf{E}(z)|$ is the magnitude of the electric field intensity as a function of propagation distance, z. E_0 is the reference at z=0. λ is the wavelength and Q the Q-factor. Therefore, constant-Q can be used to describe the combined dielectric and scattering losses. The latter will be addressed in Section 4.1.2.

In the purely dielectric case, Bano (1996) demonstrates that the 'universal' power-law (Jonscher, 1977) corresponds to a constant-Q model

$$\frac{\Im}{\Re}\Big\{ \varepsilon(\omega) - \varepsilon_\infty \Big\} = \frac{\varepsilon''(\omega)}{\varepsilon'(\omega) - \varepsilon_\infty} \approx \frac{1}{Q} , \tag{4.10}$$

for permittivities above the relaxation frequency, expressed as

$$\varepsilon(\omega) = \varepsilon'(\omega) + j\varepsilon''(\omega) = \varepsilon_{ref} \left(-j \frac{\omega}{\omega_{ref}} \right)^{n-1} + \varepsilon_\infty . \tag{4.11}$$

The parameter n takes a value between 0 and 1, ε_∞ is the high-frequency permittivity, ω_{ref} is a reference angular frequency and ε_{ref} is a corresponding reference permittivity. The relationship between n and Q is:

$$n = \frac{2}{\pi} tan^{-1}(Q) . \tag{4.12}$$

For pure dielectric losses, the Q-factor is the reciprocal of the loss tangent,

$$\tan(\delta) = \varepsilon''/\varepsilon' = 1/Q . \tag{4.13}$$

In Figure 4.3 (b) a constant-Q model is plotted, and in (c) the attenuation coefficients are compared with those of the Cole-Cole models in (a). Bradford (2007) advocates how the constant-Q model is useful for describing several dielectric models, like Cole-Cole or Debye, in the case of band-limited GPR signals. For the plotted dielectric models, it appears the approximation holds well. For the S#4 rock sample, the attenuation curve has been shifted with regards to that of an ideal constant-Q medium with zero attenuation at zero frequency. The slope of the S#4 attenuation curve is nevertheless similar to Q=5, but with a constant shift of about -4 dB. Similar observations were actually made during in laboratory measurements by Turner and Siggins (1994), and lead them to define a generalized constant-Q for radar sounding (often denoted Q*) where extrapolation towards zero frequency would give a non-zero attenuation.

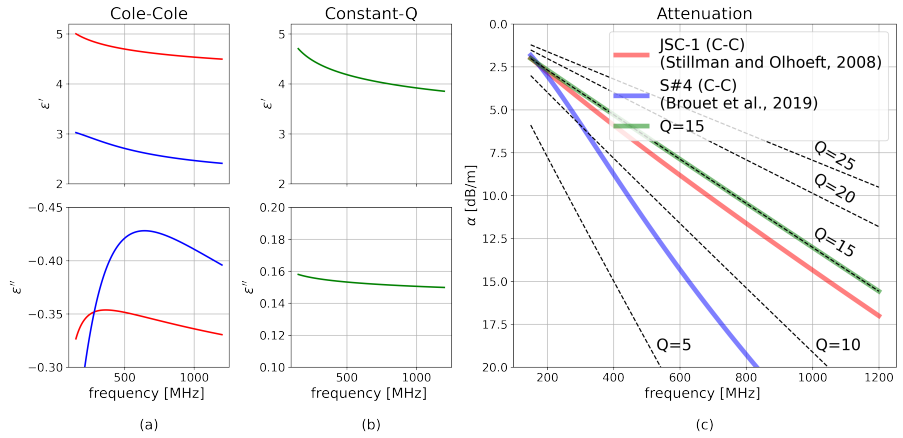

Figure 4.3: (a) Cole-Cole models based on laboratory measurements of rocks (Brouet et al., 2019; Stillman & Olhoeft, 2008). (b) Constant-Q dielectric model for Q=15, ε_∞=1.0, ω_{ref}=600MHz, and ε_{ref}=4. (c) Comparison of attenuation coefficients for Cole-Cole models from (a) and the Constant-Q model from (b). A range of constant-Q values are also plotted with dashed lines, computed for a propagation velocity of 0.15 m/ns.

4.1.2 Scattering loss

Wave propagation thorough an inhomogeneous or heterogeneous medium, will cause continuous scattering of the wavefront and consequently lead to an energy decay; referred to as volume scattering loss. That is, natural media will introduce frequency dependent attenuation that depend on the size, distribution and geometry of the inhomogeneities or reflectors.

In an idealized setting, the response can be described by Mie scattering theory (e.g., Ulaby & Long, 2014). Assuming homogeneously distributed spherical inclusions of a certain size distribution, in a background medium, Mie scattering is a common approach for predicting scattering losses in GPR studies (Di Paolo et al., 2018; Pettinelli et al., 2007). Figure 4.4 (a) presents attenuation constants over the RIMFAX bandwidth for two cases of Mie scattering.

Assuming a stratified and layered propagation medium, with layer thickness varying according to Gaussian, exponential or fractal correlation functions, Van Der Baan (2001) derives theoretical relationships of volume scattering based on wave localization theory. Gaussian and exponential derived functions show very distinct attenuation from the general constant-Q response. Attenuation is highest where the layer thickness l times the wavenumber k equals one (kl=1), and decays for higher frequencies. Fractal-like media approximates a constant attenuation with higher frequencies (Van Der Baan, 2002). Figure 4.4 (b) compares volume scattering in stratified layering based on the three different correlation functions.

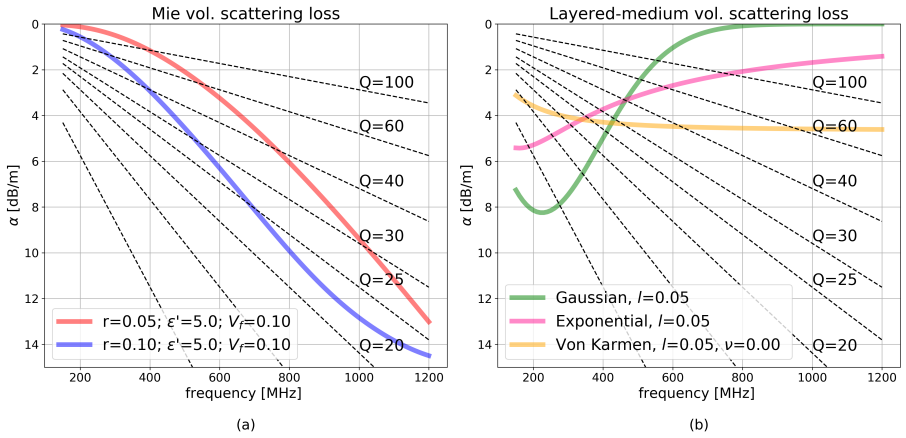

Figure 4.4: Comparison of attenuation due to volume scattering over the RIMFAX bandwidth. Estimates of dB/m assume a propagation velocity of 0.1 m/ns. (a) Mie scattering due to homogeneously distributed spherical inclusions in a background medium. r is radius of inclusions, ε' is the permittivity of the inclusions, and V_f is the volume fraction of inclusions. (b) Volume scattering due to layered-media with dimensions l, based on wave localization theory with different correlation functions. Von Karmen correlation function with ν=0 equals a fractal model.

4.1.3 Reflection at geological targets

The reflection at a single surface in radar imaging can be described theoretically as the sum of reflections from a distributed target over an illuminated surface area. This is described by the radar cross section (RCS) and is defined as the ratio of scattered energy to the incident power density. In the simplest case, a plane wave reflected at a planar and smooth medium boundary can be approximated by Fresnel reflectivity (as also assumed in Section 3.5.1). Since RIMFAX is a nadir-looking radar, we will focus this section on normal incidence reflections. The Fresnel specular reflectivity Γ is defined as the ratio of reflected to incident power, or the squared of reflected to incident electric field intensities,

$$\Gamma = P^r/P^i = |E^r/E^i|^2 = \left|\frac{\eta_2 - \eta_1}{\eta_2 + \eta_1}\right|^2, \tag{4.14}$$

which is determined by the change in intrinsic impedance

$$\eta = \frac{\eta_0}{\sqrt{\varepsilon(\omega)}} = \frac{\eta_0}{\sqrt{\varepsilon'(\omega)}}\left(1 - j\frac{\varepsilon''(\omega)}{\varepsilon'(\omega)}\right)^{-1/2}. \tag{4.15}$$

η_0 is the intrinsic impedance of free air.

Reflections from more complicated geological targets can contain certain characteristics which are not appropriately predicted by the specular Fresnel

reflectivity. A more elaborate versions of the RCS would be required, which can typically be obtained through modelling. For example, dispersive media will have a spectral response (Giannakis & Giannopoulos, 2014). Moreover, from general wave theory employed in seismic, we know that a wave reflected off a thin-layer with thickness below a quarter of the dominant wavelength, the composite seismic amplitude decreases linearly with thickness and the peak frequency slightly increases as the layer thickness decreases (Liu & Marfurt, 2007). Similar effects should be expected in GPR sounding over thin-layered media, but has not been studied as far as the author is aware. Another example is the analytical back-scattered signal based on Mie series, where returned amplitude and spectra are also characteristic of the size of the inhomogeneities (e.g., Ulaby & Long, 2014).

4.1.3.1 Realistic surface roughness

For a natural surface, the topographic roughness will affect the appearance and magnitude of the reflection in a radar image. On a scale much larger than the wavelength, typically meter-scales for GPR sounding, a rough layer interface will appear as a superposition of diffractions and unfocus the reflector image. This effect is studied in Paper I. Some of the along-track topography over a reflector can be corrected in the radar image through migration (as in Section 3.3),

On a scale comparable to the wavelength, centimeter-scale for GPR-imaging, the magnitude of reflections will be a function of the EM-roughness:

$$ks = \frac{2\pi}{\lambda} s\,, \tag{4.16}$$

where s is the root-mean-square (RMS) height of the surface

$$s = \Big[\int_{-\infty}^{\infty} z^2 p(z) dz \Big]^{1/2}, \tag{4.17}$$

and $p(z)$ the distribution of topographic heights, typically assumed to be Gaussian. A surface is considered smooth for ks<0.2 according to the Fraunhofer criterion for plane waves at normal incidences, which require that the maximum phase difference within a reflection to be less than $\pi/8$ radians.

There are several models that modify the magnitude in reflectivity by incorporating the surface roughness, e.g., the zeroth-order physical-optics solution (De Roo & Ulaby, 1994) and the sophisticated I^{2}EM computational algorithm for air/surface reflectivity (Fung et al., 2002). Figure 4.5 presents the results of bistatic reflectivity as a function of surface roughness and incidence angle. Reflectivity is presented as the ratio of the coherent component in the specular direction Γ_{coh} to the theoretical specular Fresnel reflectivity Γ. For a nadir-looking radar and normal incidence reflections (e.g., setting $\cos\theta$=1 in Figure 4.5), the general result is that reflectivity decreases with increasing roughness. Another observation relevant for subsurface sounding, is the relative increase in EM-roughness for a given RMS height s. For example, for a medium with a propagation velocity of 0.1 m/ns, the EM-roughness of a subsurface interface will be three times larger than if it would be located at the air/surface interface.

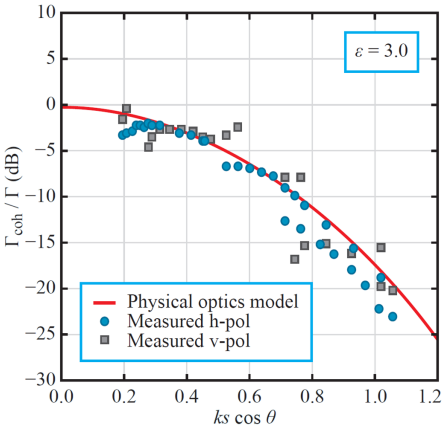

Figure 4.5: Reflectivity as a function of surface roughness, for an analytical zeroth-order physical-optics solution for an air/surface interface with surface permittivity of ε'=3. Also plotted are horizontal and vertical polarized bistatic measurements. Figure from Ulaby and Long (2014).

4.2 Computational electromagnetic methods

GPR-modeling enables calculation of travel time, returned energy or the amplitude response of one or more subsurface targets. As reviewed in Section 1.4, forward modeling can be used to compare with acquired data and hopefully help constrain some subsurface structures and media properties. Alternatively, forward modeling can help evaluate a processing step or routine, or a data analysis technique. Nevertheless, in all cases it is important to account for instrument characteristics as reviewed in Chapter 3, and natural media properties that were addressed in Section 4.1.

The simplest approach is the 1D convolutional model where a waveform is convolved with a reflectivity series (Bianco, 2014). This can be extended into 2D and 3D to incorporate geometrical effects by for example ray-tracing, assuming that an optical travel path is appropriate to describe the wavefront (Cervený, 2001). This high frequency method, or more generally, "asymptotic technique", makes a fundamental approximation to the physics of electromagnetic wave propagation. This may be sufficient in some cases of, e.g., kinematic travel time assessment that is an essential part of subsurface imaging, though there are many scenarios where this would not be appropriate.

Alternatively, analytic solutions of specific idealized scenarios can provide insights to specific aspects of wave propagation, e.g. for estimating scattering losses (Di Paolo et al., 2018; Pettinelli et al., 2007). Radiative transfer theory is an approach that exclusively calculates the energy budget based on various interactions, and can be efficient in certain applications like radiometric analysis and estimates of atmospheric radar wave propagation (Ulaby & Long, 2014).

For this thesis, we have employed a "full-wave" computational electromagnetic (CEM) approach (Davidson, 2010), where we directly calculate the electromagnetic field in a defined subsurface model through numerical iterations. There are numerous available methods and hybrid implementations, both in open source software and commercial products. Each have gained popularity for distinct applications. The selection for this thesis landed on the open source project gprMax (Warren et al., 2016) employing the Finite-Difference Time-Domain (FDTD) technique. Before going into the fundamentals of FDTD in Section 4.2.1 and a description of gprMax in Section 4.2.2, the full-wave CEM methods will be briefly compared in order to evaluate suitableness for subsurface modeling.

In addition to the FDTD technique, the Finite Element Method (FEM) and the Method-of-Moments (MoM) are also popular for CEM applications. The methods all approximate Maxwell's equations numerically, without any initial physical approximation being made, and they discretize some electromagnetic property in space and time for conducting iterative numerical calculations. Table 4.1 presents a overview of how these methods compare for open region problems, which is the typical GPR application. Only a high level comparison based on Davidson (2010) will be given in the remainder of this section. See original author for a more detailed description.

Method	**Equation type**	**Domain**	**Radiation condition**	**PEC only**	**Hetero-geneities**	**Waveform**
FDTD	differential	time	No	weak	good	broadband
FEM	differential	frequency	No	weak	good	monochromatic
MoM	integral	frequency	Yes	good	weak	monochromatic

Table 4.1: Strengths and weaknesses of CEM methods as widely implemented for open region problems. Table modified from Davidson (2010).

MoM is a integral method and is the least computationally demanding of the CEM methods. It has it origins in mathematical physics and analytical electromagnetic theory, employing Green functions to simulate the radiating fields. Traditionally, MoM has been applied in frequency domain for monochromatic waves, i.e. for a single frequency at a time, and the method is a popular choice for simulating radiation from antennas or scattering from highly conductive surfaces. The method is not, however, suited for simulating propagation through an heterogenous media nor for simulating UWB waveforms, as would be important for modeling and evaluation of GPR sounding.

FEM is a general numerical method for solving partial differential equations, and is like MoM typically employed for monochromatic waves in frequency domain. FDTD is also a differential formulation, but solving Maxwell's equation directly in time domain. Both FEM and FDTD can simulate propagation through heterogeneous media properties, as well as include dispersive dielectric models. Contrary to MoM which includes the radiation condition in its formulation, both FEM and FDTD need to include specific boundary conditions. FDTD has,

however, a great advantage over FEM in GPR applications, with the ability to simulate a broadband waveform.

In conclusion, FDTD is the more appropriate choice for simulating UWB GPRs when studying subsurface properties and geometries. A draw-back, however, is the computationally resource demanding implementation compared to FEM and, in particular, MoM. The rigid spatial discretizised model in FDTD is less flexible than both MoM and FEM, where both are able to incorporate non-cubic meshes or varying size. Whereas FDTD can only discretizise into regularized cubic cells. FDTD is not as efficient to simulate antenna radiation as MoM, or dispersive properties and model geometries as FEM, but for UWB wave propagation in a model with natural-like media properties, it is the method of choice.

When studying a specific problem with the help of numerical modeling, it is advantageous to verify the output by means of other techniques in order to ensure that the numerical results are accurate. The verification process is a broad topic, but such verification is typically done with analytical solutions to simplified and idealized parts of the problem or other modeling schemes. Paper I and II uses analytical idealized plane-wave solutions to assess the accuracy of the modeling results.

4.2.1 The Finite-Difference Time-Domain (FDTD) method

Finite difference is a technique that essentially approximates differentiation operators in a partial differential equation. Depending on how it is formulated, it can be either forward, backward or centrally oriented. Consider a function $f(x)$, the forward formulation of the finite difference approximation can be derived with the Taylor series:

$$f'(x) = \frac{f(x+\Delta x) - f(x)}{\Delta x} + O(\Delta x)\,, \tag{4.18}$$

where Δx is the discretized step size. The residual $O(\Delta x)$ denotes the sum of all terms of first order and higher, which effectively defines the accuracy of the approximation. Similarly, the central differencing formulation takes the form:

$$f'(x) = \frac{f(x+\Delta x) - f(x-\Delta x)}{2\Delta x} + O[(\Delta x)^2]\,, \tag{4.19}$$

but here the approximation error $O[(\Delta x)^2]$ only contains terms of second order and higher, i.e. the approximation is second-order accurate.

Electromagnetic phenomena on a macroscopic scale, involving the electric field intensity $\mathbf{E}$ and the magnetic field intensity $\mathbf{H}$, are described by Maxwell's equations. By assuming only conductive currents, the volume charge density is zero and we focus on:

$$\nabla \times \mathbf{E} = -\mu \frac{\partial \mathbf{H}}{\partial t} \quad \text{(Faraday's law)}, \tag{4.20}$$

$$\nabla \times \mathbf{H} = \mathbf{J} + \varepsilon' \varepsilon_0 \frac{\partial \mathbf{E}}{\partial t} \quad \text{(Ampère's law)}. \tag{4.21}$$

The current density $\mathbf{J}=\sigma\mathbf{E}$ is defined with the conductivity σ of the medium. μ is the magnetic permeability, ε' the permittivity, and ε_0 permittivity of free space. We include a source term $\mathbf{\Phi}$ in Equation 4.21 and decompose the fields into principal components, to obtain six scalar equations:

$$\begin{aligned}
\frac{\partial E_z}{\partial y} - \frac{\partial E_y}{\partial z} &= -\mu\frac{\partial H_x}{\partial t} \\
\frac{\partial E_x}{\partial z} - \frac{\partial E_z}{\partial x} &= -\mu\frac{\partial H_y}{\partial t} \\
\frac{\partial E_y}{\partial x} - \frac{\partial E_x}{\partial y} &= -\mu\frac{\partial H_z}{\partial t} \\
\frac{\partial H_z}{\partial y} - \frac{\partial H_y}{\partial z} &= \varepsilon'\varepsilon_0\frac{\partial E_x}{\partial t} + \sigma E_x + \Phi_x \\
\frac{\partial H_x}{\partial z} - \frac{\partial H_z}{\partial x} &= \varepsilon'\varepsilon_0\frac{\partial E_y}{\partial t} + \sigma E_y + \Phi_y \\
\frac{\partial H_y}{\partial x} - \frac{\partial H_x}{\partial y} &= \varepsilon'\varepsilon_0\frac{\partial E_z}{\partial t} + \sigma E_z + \Phi_z
\end{aligned} \tag{4.22}$$

The modeling domain is discretized into Yee cells (Yee, 1966), containing a value for each of the six field components in Equation 4.22. The electric and magnetic field intensities are offset by half a grid size as illustrated in Figure 4.6.

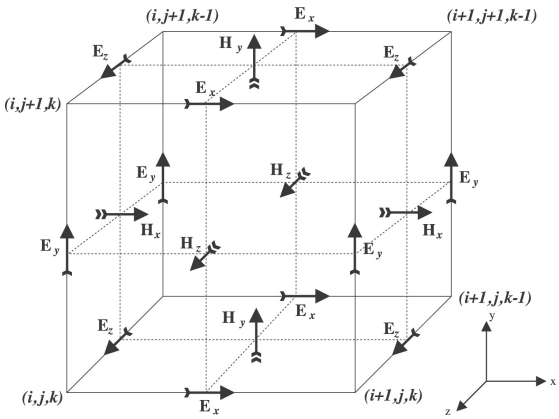

Figure 4.6: Finite difference discretized Yee cell. Figure from Warren et al. (2016).

FDTD can solve an 'initial value' problem, where a source excites the simulation and the evolution of the fields are calculated based on previous states. By discretizing both time (Δt) and 3D space (Δx, Δy, Δz), Equation 4.22 can be solved with a finite difference formulation in a 'leap-frog' approach. The electric field components are solved at a given instant in time; then in turn the magnetic field vector components are solved with half a time step offset. Then the process is repeated with the electric field offset by half a time step from

the preceding magnetic field. Since fields are offset by half a step in both space and time, Equation 4.22 can be solved with central differencing approximation and second-order accuracy.

The FDTD scheme is conditionally stable, and one have to select the time step according to the spatial discretization. Stability is ensured by adhering to the Courant-Friedrichs-Lewy (CFL) condition (Courant et al., 1967):

$$\Delta t \leq \frac{1}{c\sqrt{\frac{1}{(\Delta x)^2} + \frac{1}{(\Delta y)^2} + \frac{1}{(\Delta z)^2}}}\,, \tag{4.23}$$

where c is the speed of light. The spatial discretization is chosen according to the specific problem, weighting result accuracy with computational cost. In general, it should be constrained to an order of a tenth of the smallest wavelength λ, to avoid phase error and numerical dispersion (Kunz & Luebbers, 1993):

$$\Delta x = \Delta y = \Delta z \leq \lambda/10\,. \tag{4.24}$$

FDTD modeling of GPR is an 'open boundary' problem, where the simulation represents unbound electromagnetic propagation but calculated within a finite computational domain. Therefore the model domain has to be truncated at its sides which cause artificial and unwanted reflections of the fields. To restrain this effect, an absorbing boundary condition (ABC) based on mathematical boundary conditions can be applied where the model domain is truncated (e.g., Kunz & Luebbers, 1993; Taflove et al., 2005). With the introduction of perfectly matched layer (PML), this is handled by adding fictitious material along the outer faces of the model to damp incoming waves. There are several distinct formulations, including the 'split-field' PML (Berenger, 1994), 'uniaxial' PML (Sacks et al., 1995), and 'stretched-coordinate' PML (Chew & Weedon, 1994). See also Bérenger (2007) for a recent overview.

With the ability to obtain a broadband solution with only one time-domain simulation, the FDTD scheme also needs to account for dispersive and frequency dependent attenuating properties, as is typical for natural materials. There exist several methods that can facilitate such behaviour, as recursive convolution techniques, auxiliary differential equations, and Z-transform methods (e.g., Taflove et al., 2005). In order to implement more complex media, e.g. like Cole-Cole dielectric functions that is often employed to describe natural soil and rocks, a popular approach is through a multi-pole Debye function (Giannakis & Giannopoulos, 2014).

4.2.2 Ground-penetrating radar modeling with gprMax

The gprMax software is an active open source project with highly capable functionality, dedicated specifically to simulation of GPR sounding (Warren et al., 2016). It is an extensive and fully working FDTD code that let the user focus on the physical problem rather than the computational implementation. Recent years, from 2018 to 2022, the software project has received around 80 - 120 citations yearly, demonstrating its popularity among the GPR community.

The user is free to modify and extend the open source where desired, but advanced features have been implemented and are readily available; e.g. dielectric smoothing and ABCs. A range of dielectric models are built-in for the user to employ (Giannakis et al., 2016), and with the possibility of multi-pole Debye formulations for approximating any dielectric model (Giannakis & Giannopoulos, 2014). Heterogeneous media is possible through fractal mixing of dielectric properties, and interface geometries can incorporate natural-like surface roughness. gprMax also comes with several opportunities to speed-up large simulations, through use of graphics processing units or message passing interface parallel processing.

The open source software project gprMax is therefore a high quality and low resource entry to electromagnetic modeling, while still maintaining flexibility and functionality for employment in sophisticated and custom simulations. The software is also able to simulate electromagnetic waves propagating through natural-like subsurface properties as reviewed in Section 4.1, and was for these reasons selected as the modeling software during this thesis work.

References

Bano, M. (1996). Constant dielectric losses of ground-penetrating radar waves. *Geophysical Journal International*, vol. 124no. 1, 279–288.

Berenger, J.-P. (1994). A perfectly matched layer for the absorption of electromagnetic waves. *Journal of computational physics*, vol. 114no. 2, 185–200.

Bérenger, J.-P. (2007). Perfectly matched layer (pml) for computational electromagnetics. *Synthesis Lectures on Computational Electromagnetics*, vol. 2no. 1, 1–117.

Bianco, E. (2014). Geophysical tutorial: Well-tie calculus. *The Leading Edge*, vol. 33no. 6, 674–677.

Bjørlykke, K., Line, L. H., Jahren, J., et al. (2017). Compaction of sand and clay-constraints from experimental compaction, chemical reactions and fluid flow during burial-an overview. *AAPG Annual Convention and Exhibition*.

Bradford, J. H. (2007). Frequency-dependent attenuation analysis of ground-penetrating radar data. *Geophysics*, vol. 72no. 3, J7–J16.

Brouet, Y., Becerra, P., Sabouroux, P., et al. (2019). A laboratory-based dielectric model for the radar sounding of the Martian subsurface. *Icarus*, vol. 321, 960–973.

Campbell, M. J., & Ulrichs, J. (1969). Electrical properties of rocks and their significance for lunar radar observations. *Journal of Geophysical Research*, vol. 74no. 25, 5867–5881.

Carrier, I., W. D., Olhoeft, G. R., & Mendell, W. (1991). Physical Properties of the Lunar Surface. In G. H. Heiken, D. T. Vaniman, & B. M. French (Eds.).

Cervený, V. (2001). *Seismic ray theory* (Vol. 110). Cambridge university press Cambridge.

Chew, W. C., & Weedon, W. H. (1994). A 3d perfectly matched medium from modified maxwell's equations with stretched coordinates. *Microwave and optical technology letters*, vol. 7no. 13, 599–604.

Courant, R., Friedrichs, K., & Lewy, H. (1967). On the partial difference equations of mathematical physics. *IBM journal of Research and Development*, vol. 11no. 2, 215–234.

Davidson, D. B. (2010). *Computational electromagnetics for RF and microwave engineering* (2nd ed.). Cambridge University Press.

De Roo, R. D., & Ulaby, F. T. (1994). Bistatic specular scattering from rough dielectric surfaces. *IEEE Transactions on Antennas and Propagation*, vol. 42no. 2, 220–231.

Di Paolo, F., Orosei, R., Lauro, S. E., et al. (2018). Volume scattering losses evaluation for radar sounding of Jovian icy moons. *2018 5th IEEE International Workshop on Metrology for AeroSpace (MetroAeroSpace)*, 2422–2425.

Ding, C., Xiao, Z., Su, Y., et al. (2020). Compositional variations along the route of Chang'e-3 Yutu rover revealed by the lunar penetrating radar. *Progress in Earth and Planetary Science*, vol. 7no. 1, 1–11.

Everett, M. E. (2013). Ground-penetrating radar. *Near-surface applied geophysics* (pp. 239–278). Cambridge University Press.

Fung, A., Liu, W., Chen, K., & Tsay, M. (2002). An improved IEM model for bistatic scattering from rough surfaces. *Journal of Electromagnetic Waves and Applications*, vol. 16no. 5, 689–702.

Giannakis, I., & Giannopoulos, A. (2014). A novel piecewise linear recursive convolution approach for dispersive media using the finite-difference time-domain method. *IEEE Transactions on Antennas and Propagation*, vol. 62no. 5, 2669–2678.

Giannakis, I., Giannopoulos, A., & Warren, C. (2016). A realistic FDTD numerical modeling framework of ground penetrating radar for landmine detection. *IEEE Journal of Selected Topics in Applied Earth Observations and Remote Sensing*, vol. 9no. 1, 37–51.

Irving, J. D., & Knight, R. J. (2003). Removal of wavelet dispersion from ground-penetrating radar data. *Geophysics*, vol. 68no. 3, 960–970.

Jonscher, A. K. (1977). The 'universal' dielectric response. *nature*, vol. 267no. 5613, 673–679.

Kunz, K. S., & Luebbers, R. J. (1993). *The finite difference time domain method for electromagnetics*. CRC press.

Liu, J., & Marfurt, K. J. (2007). Instantaneous spectral attributes to detect channels. *Geophysics*, vol. 72no. 2, P23–P31.

Olhoeft, G. R., & Strangway, D. (1975). Dielectric properties of the first 100 meters of the Moon. *Earth and Planetary Science Letters*, vol. 24no. 3, 394–404.

Pettinelli, E., Burghignoli, P., Pisani, A. R., et al. (2007). Electromagnetic propagation of GPR signals in Martian subsurface scenarios including

material losses and scattering. *IEEE Transactions on Geoscience and Remote Sensing*, vol. 45no. 5, 1271–1281.

Richards, P. G., & Aki, K. (1980). *Quantitative seismology: Theory and methods* (Vol. 859). Freeman New York.

Sacks, Z., Kingsland, D., Lee, R., & Lee, J.-F. (1995). A perfectly matched anisotropic absorber for use as an absorbing boundary condition. *IEEE Transactions on Antennas and Propagation*, vol. 43no. 12, 1460–1463.

Stillman, D., & Olhoeft, G. (2008). Frequency and temperature dependence in electromagnetic properties of Martian analog minerals. *Journal of Geophysical Research: Planets*, vol. 113no. E9.

Taflove, A., Hagness, S. C., & Piket-May, M. (2005). Computational electromagnetics: The finite-difference time-domain method. *The Electrical Engineering Handbook*, vol. 3, 629–670.

Turner, G., & Siggins, A. F. (1994). Constant Q attenuation of subsurface radar pulses. *Geophysics*, vol. 59no. 8, 1192–1200.

Ulaby, F. T., Bengal, T. H., Dobson, M. C., et al. (1990). Microwave dielectric properties of dry rocks. *IEEE Transactions on Geoscience and Remote Sensing*, vol. 28no. 3, 325–336.

Ulaby, F. T., & Long, D. G. (2014). *Microwave radar and radiometric remote sensing* (Vol. 4). University of Michigan Press Ann Arbor, MI, USA.

Van Der Baan, M. (2001). Acoustic wave propagation in one dimensional random media: The wave localization approach. *Geophysical Journal International*, vol. 145no. 3, 631–646.

Van Der Baan, M. (2002). Constant Q and a fractal, stratified earth. *Seismic waves in laterally inhomogeneous media* (pp. 1707–1718). Springer.

Warren, C., Giannopoulos, A., & Giannakis, I. (2016). gprMax: Open source software to simulate electromagnetic wave propagation for Ground Penetrating Radar. *Computer Physics Communications*, vol. 209, 163–170.

Watters, T. R., Leuschen, C. J., Campbell, B. A., et al. (2017). Radar sounder evidence of thick, porous sediments in Meridiani Planum and implications for ice-filled deposits on mars. *Geophysical Research Letters*, vol. 44no. 18, 9208–9215.

Xing, S.-G., Su, Y., Feng, J.-Q., et al. (2017). The penetrating depth analysis of Lunar Penetrating Radar onboard Chang'e-3 rover. *Research in Astronomy and Astrophysics*, vol. 17no. 5, 046.

Yee, K. (1966). Numerical solution of initial boundary value problems involving Maxwell's equations in isotropic media. *IEEE Transactions on antennas and propagation*, vol. 14no. 3, 302–307.

Chapter 5

Summary of Papers and Future Work

This thesis studies how modeling can benefit Mars exploration with RIMFAX, and through this approach GPR modeling methodology and analysis techniques have also been investigated. In particular has quantitative analysis of attenuation been studied in great detail. Below, each peer-reviewed paper is addressed individually, relating the papers to one another and to contemporary research. The papers are also put into context of the thesis' objectives. Conclusions and reflections on future work is provided towards the end of this chapter.

All papers are collaborative efforts, but the corresponding author has been leading individual studies in terms of contextualization, technical work and writing. Supervisors and coauthors have contributed with insightful advice and vital discussions, as well as review of text. Processing and analysis of RIMFAX data have employed and built upon core functionality in the 'rimlib' repository, developed by the RIMFAX Science Team.

Paper I is a pre-mission assessments conducted prior to landing of the Perseverance rover, and summarizes the knowledge and expectations before the first RIMFAX soundings were conducted on Mars. It aims at using GPR modeling to evaluate RIMFAX imaging of geological contacts and features observed in orbital imagery. The Jezero Crater landing site geology is therefore reviewed, in particular across the Crater Floor, and related to physical properties of regolith and rocks relevant for GPR sounding. Relevance of orbital radar measurements by MARSIS and SHARAD are also discussed.

The paper also presents how the gprMax FDTD simulation software can be extended to include GIS capabilities for model building. Initial results were first presented in Eide et al. (2019) and later also included in Hamran et al. (2020). An in-depth description of the model building approach is presented in Appendix A. The ability to display radargrams in 3D GIS software is also demonstrated, showing the benefit of linking features in imagery of the surface with results from subsurface sounding (see also Section 3.4).

Paper II describes how a FMCW GPR is efficiently modelled with the FDTD method. As the FDTD method is an appropriate choice for UWB GPR modeling (see Section 4.2), and gprMax being a popular open source FDTD implementation, we demonstrate the necessary steps in order to model RIMFAX with its FMCW stretch processing receiver. This approach

has not been appropriately described in literature previously, and should therefore be a useful reference for the GPR community.

There are, however, FDTD implementations of stepped frequency continuous wave radar (Kafedziski et al., 2018), a radar system with similarities to FMCW radar. Simulations are done by consecutive approximately-monochromatic waves for generating a realistic radar response, but do not take advantage of FDTD's ability to acquire entire target responses with wideband waveforms in a single run. Others have also modelled FMCW with commercial software, e.g. Fioranelli et al. (2015) studying through-the-wall radar imaging employing CST Microwave Studio and its Finite Integration Technique (very similar to FDTD). But a detailed description of the modeling procedure is not provided.

The paper also addresses background theory and the importance of frequency dependent attenuation and dispersion, in both GPR imaging and FDTD modeling. Earlier work on these topics are reviewed, paving the road for the work presented in Paper III.

Paper III presents time-frequency analysis of all RIMFAX data acquired during the Crater Floor campaign, covering approximately a total of 5 km traverse distance. The analysis evaluates the centroid-frequency shift method that has previously been employed to constrain the amount of attenuation in subsurface studies (Quan & Harris, 1997). Attenuation is approximated through a constant-Q model with a linear dependence on frequency. Modeling according to Paper II is done in order to validate the implementation and evaluate the accuracy of the analysis.

Another key topic in this study is enhancement of the recorded deramped signal for spectral analysis, employing the Maximum Entropy technique (Burg, 1975). By identifying and removing artifacts in RIMFAX' deramped signal, retrieving missing parts of the bandwidth is attempted with interpolation based on a Maximum Entropy autoregressive model.

Paper IV presents a dip attribute analysis for RIMFAX data. Modeling based on Paper I and II is used to generate a test dataset for validating a complex trace analysis technique (Barnes, 2007), which automatically extracts the orientation of reflections in a radargram profile. This is then applied in a novel approach for estimating the true subsurface dip, by stereographic fit of apparent dip estimates that have been acquired along the rover traverse in several directions. While this conference proceedings reviews the method, an extract from the conference poster presentation in Appendix B expands on the results and interpretations.

In summary, several aspects of GPR modeling for assessing and supporting RIMFAX acquisition and analysis have been addressed in this thesis. GIS capabilities has helped link imagery of the Martian surface with synthetic radargram, by employing true scales of geological structures on Mars directly in forward modeling. This has enabled both (i) pre-acquisition assessment in

Paper I, and (ii) interpretation and analysis support in Paper IV. These results are according to the thesis objectives. Modeling has moreover been conducted with realistic and natural-like subsurface properties as reviewed in Section 4.1, and with representative instrument characteristics as described in Chapter 3 and Paper II. In Paper III, this was used to rigorously test an analysis technique, which in turn was used to conduct quantitative attenuation analysis of data acquired over the Jezero Crater Floor.

For future work, it still remains to disentangle dielectric and scattering contributions in quantified attenuation estimates (Paper III), and e.g. investigate whether it is possible to detect bound water in Martian rocks. Besides, several of the methods presented in the thesis could be employed on more RIMFAX data, in order to study geological implications in Jezero Crater more exhaustively. 3D software (Section 3.4), for example, can be used to better understand the connection between surface exposures and subsurface soundings. Running the RIMFAX dip attribute analysis (Paper IV) on additional areas on the Crater Floor, could potentially help better constrain the exact Séítah-Máaz relationship, one of the remaining puzzles from the Crater Floor exploration. RIMFAX modeling of outcrop exposures, e.g. similarly to Lecomte et al. (2016) and as done in Paper IV, could be done in additional places and perhaps aid interpretation of RIMFAX sounding where the rover has crossed corresponding lithologies.

For Jezero Western Delta exploration, applying the RIMFAX dip attributes for analyzing layer orientations within the successions should be rewarding. Quantitative attenuation analysis should be interesting for comparing with the Crater Floor, as well as between distinct deposits within the delta.

For future analysis and interpretation of RIMFAX data, the Maximum Entropy interpolation (Paper III) could be applicable for deramped signal enhancement. There are also two general results from this thesis that could be useful for the broader GPR community, beyond RIMFAX and Martian exploration: (i) the FDTD implementation of FMCW radar, and (ii) the review of the centroid-frequency shift method for reliable attenuation estimates.

Throughout this thesis, excitation of simulations have exclusively been done with an idealized Hertzian dipole source that cannot account for the RIMFAX antenna radiation pattern, near-field effects, or interaction with the rover body. The latter, will ideally be removed during radargram processing and background removal. The FDTD implementation in gprMax has capabilities to include antenna radiation patterns and near-field effects, by representing realistic antenna structures (Giannakis et al., 2018; Warren & Giannopoulos, 2011). But this is achieved at the cost of finer spatial discretization and higher computational load. With future additions to the gprMax FDTD implementation of subgridding or near-to-far field transformation, for example, it may be possible to include an antenna model without drastically increasing computation time. Nevertheless, Tran et al. (2013) study antenna height to antenna aperture ratios in FDTD simulations, and demonstrate that near-field effects are negligible and the far-field assumption holds for ratios above 1.2. The ratio for RIMFAX will approximately be 0.7m/0.2m=3.5.

Inversion modeling has not been a topic of this thesis due to the low geometric

constraint as described in Section 3.3, which makes inversion of RIMFAX data an ill-posed problem. Nevertheless, applying forward modeling for generation of authentic training sets for machine learning approaches (e.g., Rohman et al., 2022), which later can be used to invert for subsurface parameters, could be a future application directly employing some results from this thesis.

References

Barnes, A. E. (2007). A tutorial on complex seismic trace analysis. *Geophysics*, vol. 72no. 6, W33–W43.

Burg, J. P. (1975). *Maximum entropy spectral analysis*. Stanford University.

Eide, S., Hamran, S., Dypvik, H., & Amundsen, H. (2019). Rimfax ground penetrating radar modelling: Imaging the subsurface of the jezero western delta. *Ninth International Conference on Mars*, vol. 2089, 6070.

Fioranelli, F., Salous, S., Ndip, I., & Raimundo, X. (2015). Through-the-wall detection with gated FMCW signals using optimized patch-like and Vivaldi antennas. *IEEE transactions on antennas and propagation*, vol. 63no. 3, 1106–1117.

Giannakis, I., Giannopoulos, A., & Warren, C. (2018). Realistic FDTD GPR antenna models optimized using a novel linear/nonlinear full-waveform inversion. *IEEE Transactions on Geoscience and Remote Sensing*, vol. 57no. 3, 1768–1778.

Hamran, S.-E., Paige, D. A., Amundsen, H. E., et al. (2020). Radar imager for Mars' subsurface experiment—RIMFAX. *Space Science Reviews*, vol. 216no. 8, 1–39.

Kafedziski, V., Pecov, S., & Tanevski, D. (2018). Target detection in SFCW ground penetrating radar with C3 algorithm and Hough transform based on gprMax simulation and experimental data. *2018 25th International Conference on Systems, Signals and Image Processing (IWSSIP)*, 1–5.

Lecomte, I., Lavadera, P. L., Botter, C., et al. (2016). 2(3)D convolution modelling of complex geological targets beyond-1D convolution. *First Break*, vol. 34no. 5.

Quan, Y., & Harris, J. M. (1997). Seismic attenuation tomography using the frequency shift method. *Geophysics*, vol. 62no. 3, 895–905.

Rohman, B. P. A., Nishimoto, M., & Ogata, K. (2022). Reconstruction of missing ground-penetrating radar traces using simplified u-net. *IEEE Geoscience and Remote Sensing Letters*, vol. 19, 1–5.

Tran, A. P., Andre, F., Craeye, C., & Lambot, S. (2013). Near-field or far-field full-wave GPR modeling as a function of the antenna height above a planar layered medium. *Prog. Electromagn. Res*, vol. 141, 415–430.

Warren, C., & Giannopoulos, A. (2011). Creating finite-difference time-domain models of commercial ground-penetrating radar antennas using Taguchi's optimization method. *Geophysics*, vol. 76no. 2, G37–G47.

Papers

Paper I

Ground-Penetrating Radar Modeling Across the Jezero Crater Floor

Sigurd Eide, Svein-Erik Hamran, Henning Dypvik, and Hans E. F. Amundsen

Published in *IEEE Journal of Selected Topics in Applied Earth Observations and Remote Sensing*, 2021, volume 14, pp. 2484–2493. DOI: 10.1109/JSTARS.2021.3055944.

Ground-Penetrating Radar Modeling Across the Jezero Crater Floor

Sigurd Eide, Svein-Erik Hamran, Henning Dypvik, and Hans E. F. Amundsen

***Abstract*—This article assesses how the ground-penetrating radar RIMFAX will image the crater floor at the Mars 2020 landing site, where lithological compositions and stratigraphic relationships are under discussion prior to mission operation. A putative mafic unit (lava flow, volcanic ash, or volcaniclastic deposit) on the crater floor will be crucial in piecing together the chronology of deposition and for understanding the volcanic history in the region. In order to see how lithological properties and subsurface geometries affect radar sounding, a synthetic radargram is generated through forward modeling with a finite-difference time-domain method. The acquisition is simulated across the mafic unit as a succession of lava flows, exploring detection of internal structures and contacts to adjacent lithologies. To compare modeling results with the alternative formation scenarios, a discussion about sounding over a tephra or volcaniclastic material is presented. Similarities and differences between Martian and terrestrial lithologies can be related to electromagnetic properties relevant for radar sounding. This article, therefore, evaluates potential scientific insights gained from acquisition across the disputed mafic unit, in light of proposed hypotheses of lithological generation.**

***Index Terms*—Finite-difference time-domain (FDTD), ground-penetrating radar (GPR), mars 2020, RIMFAX.**

I. Introduction

DISCLOSING the near-surface geology will be among the great advances in future exploration of Mars. Not only will it add to our understanding of the planet's geological history and *in situ* resources, but it may also be of major astrobiological interest [1]. The radar imager for Mars' subsurface experiment (RIMFAX) [2] aboard NASA's Mars 2020 rover mission will pioneer in imaging the Martian near surface. The ground-penetrating radar (GPR) will take measurements every 10 cm along the drive path, unveiling subsurface structures, bedding, and stratigraphic relationships. In like manner, GPRs are also included among the scientific payloads for the Chinese Tianwen-1 mission [3] (launched in 2020) and the upcoming European-Russian ExoMars mission [4] (planned for launch in 2022). Improved understanding of Martian geology will be achieved through radar sounding during the next decade of Martian exploration.

To image the subsurface, a GPR transmits microwaves to detect changes in density and composition, i.e., variations in the ground's electromagnetic properties. In those terms, lithological properties can be described by the relative dielectric constant ε^*

$$\varepsilon^* = \varepsilon' - j\varepsilon''. \tag{1}$$

The real part ε' is referred to as the dielectric constant and dominates the propagation velocity in a medium. A GPR essentially records reflections caused by velocity differences in the subsurface, e.g., at the interface between two distinct lithologies. However, small-scale heterogeneous velocity changes can cause scattering and lead to energy reduction in the propagating wavefront, denoted by volume losses. The imaginary part ε'' is referred to as the dielectric loss factor and is a frequency-dependent quantity ($\varepsilon'' = \sigma/\omega\varepsilon_0$, where ω is the angular frequency of the electromagnetic wave, σ is the medium conductivity, and ε_0 is the permittivity of vacuum). The dielectric loss factor describes the intrinsic attenuation in a medium that greatly affects penetration depths in radar sounding. Magnetic properties will similarly influence propagation velocities and attenuation but are generally negligible with the exception of lithologies containing substantial amounts of ferro- or ferrimagnetic material.

Investigation in terrestrial and lunar terrains is a starting point for predicting the dielectric properties for unexplored lithologies on Mars and assessing similarities and differences for radar sounding. As on Earth, GPR imaging has proven successful for several geological applications, including stratigraphic analysis [5] and sounding in volcanic terrain [6], [7]. Landed missions on the Moon have used radar sounding to investigate the regolith thickness and volcanic layering [8]–[10]. Laboratory measurements of dry rocks show wide variations in dielectric constants with a strong correlation to bulk density [11]–[13]. While water content greatly increases the attenuation of microwaves, the dielectric loss factor in dry rocks is dominated by the number of chemical constituents as titanium and iron oxides [12], [13].

In contrast, on Mars, direct measurements of the dielectric constant have only been done by the Phoenix lander [14], but Martian soil simulants have been extensively analyzed in the laboratory [15] and GPR field tests have been conducted in Mars analog terrain [16], [17]. Intriguingly, prominent magnetic surface properties have been measured *in situ* by several landed missions [18]–[20], and magnetization in the lithosphere has been mapped from orbit and, at places, estimated to be one

Manuscript received October 30, 2020; accepted January 27, 2021. Date of publication February 1, 2021; date of current version February 22, 2021. *(Corresponding author: Sigurd Eide.)*

Sigurd Eide and Svein-Erik Hamran are with the Department of Technology Systems, University of Oslo, 2007 Kjeller, Norway (e-mail: sigurd.eide@its.uio.no; s.e.hamran@its.uio.no).

Henning Dypvik is with the Department of Geosciences, University of Oslo, 0371 Oslo, Norway (e-mail: henning.dypvik@geo.uio.no).

Hans E. F. Amundsen is with the Vestfonna Geophysical AS, 8310 Kabelvåg, Norway (e-mail: ha@epx.no).

Digital Object Identifier 10.1109/JSTARS.2021.3055944

This work is licensed under a Creative Commons Attribution 4.0 License. For more information, see https://creativecommons.org/licenses/by/4.0/

order of magnitude larger than on Earth [21]. It is, therefore, possible that magnetic properties could be noticeable for radar sounding on Mars. In the region around the Mars 2020 landing site, specifically, the mapped crustal magnetization is weak [22], although it does not preclude substantial magnetic mineralogy in a demagnetized crust or localized magnetization that is undetectable at orbital altitudes.

Space-borne radars have been sounding the Martian crust's upper hundreds to thousands of meters [23], [24], operating at lower frequencies and larger spatial scales compared to RIMFAX. Analyzing recordings from Shallow Radar (SHARAD) on Mars Reconnaissance Orbiter, Morgan *et al*. [25] investigated the possibility for detecting shallow subsurface reflections that could presumably also be seen by RIMFAX. However, due to a large spatial footprint and topographic variation around the Mars 2020 landing site, clutter obscure subsurface reflections and make such correlation problematic. Accordingly, it is at present largely unknown what RIMFAX will be able to image when operating on the surface of Mars.

As a precursor to planetary rover missions, orbital data are used for geological investigations. Despite extensive mapping already having been conducted at the Mars 2020 landing site [26]–[29], it is generally hard to infer from orbit the origins and exact relationships between outcrops [30], [31], let alone their relationship in the subsurface. Consequently, predicting how the subsurface geology will be imaged by a ground-based GPR holds room for considerable conjecture, while all the more important for evaluating potential science outcome from the upcoming acquisition. To assess RIMFAX-imaging based on the available information, a workflow for generating synthetic radargrams through forward modeling will be presented.

A putative lava flow [26], [32], in this article referred to as the mafic unit, is covering large areas of the landing site; however, based on orbital data alone, it is not possible to rule out alternative origins such as tephra or volcaniclastic deposition [29], [33]. Determining its formation history and stratigraphic context will be central for understanding the geological history of the area. After reviewing discussions surrounding the landing site geology, radar sounding will be simulated in order to examine possible detections made within and beneath the hypothesized lava flow and identify their scientific implications. Similarities and differences between electromagnetic properties in Martian and terrestrial lithologies will be explored, and comparisons will be done between the proposed formational hypotheses for the mafic unit.

II. Modeling Workflow

To assess GPR-acquisition in frontier areas where information is sparse, a modeling workflow was developed (see Fig. 1). Geological mapping and interpretations build on previous studies of the landing site extend the geological model into the subsurface. Using the software BGS Groundhog Desktop GSIS [34] for constructing the subsurface model, dimensions and geometries are kept consistent with observations made of the surface and their geological interpretations. Electromagnetic values are assigned based on interpreted formation, e.g., similar to laboratory measurements of a particular type of rock, predictions from radar sounding in comparable terrain, or rock physics considerations.

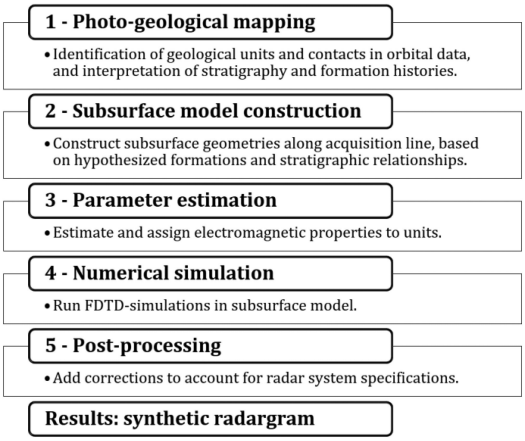

Fig. 1. Modeling workflow involves five steps for producing a synthetic radargram in a frontier area. The minimum input data required for steps 1 and 2 are surface imagery and a digital terrain model. When additional information is available, e.g., detailed surface observations, it can be included in steps 1–3 to enhance the authenticity of the input model used in numerical simulations, step 4. Step 5 corrects for the large data range achieved in numerical simulations compared to that of the actual radar system.

Numerical simulations are carried out with the software gprMax [35], employing a finite-difference time-domain (FDTD) algorithm [36] for solving Maxwell's equations in three dimensions. The amount of computational resources required in numerical simulations put restrictions upon the level of detail that can be considered and the accuracy of the results. To enable FDTD-simulation over hundreds of meters, each sounding is simulated in a separately gridded model around the source and receiver. The domain size is adjustable according to along- and cross-track contributions and target depths. The along-track dimension is predominantly 4.0 m but increases to as much as 10–15 m in areas where off-nadir reflections are thought to be prominent. In the cross-track direction, layer boundaries are extrapolated 3.0 m laterally, ensuring that the first Fresnel zone is enclosed in the domain. To replicate more natural-like surfaces, fractal surface roughness is added in both along- and cross-track directions [5], Cross-track dips of horizons due to geological structures are not accounted for. The depth dimension extends until 19 m at most.

RIMFAX's "deep operation mode" is the focus of this article, where a frequency modeled continuous wave (FMCW) sweeps through the frequency range 150–600 MHz. To prevent very large simulation times, however, an 11.0 ns broadband Ricker wavelet with 250 MHz center frequency and a frequency content that encompasses that of the FMCW is employed as a first approximation.

Discretization of the model space is constrained by the frequency content of the source wavelet, so in order to prevent substantial numerical dispersion, discretization needs to be at least

ten times smaller than the smallest wavelength [37]. However, targets in the model for the most part are substantially thick and laterally continuous and not considered to put significant constraints upon discretization. For the highest value of the dielectric constant in this article ($\varepsilon' = 6.0$), the wavelength corresponding to 600 MHz is sampled by ten cells when discretization of Yee-cells [36] is 0.02 m^3. The CFL-condition ensuring a stable numerical process [37] requires a corresponding time step of 3.8e-11 s. A 250 MHz Ricker wavelet has a highest significant frequency at 700 MHz (at its -40 dB level), giving an estimated largest physical phase-velocity error of -1.5% [38].

In the deep operation mode, gating between transmission and recording in FMCW-acquisition efficiently mutes reflections within the upper meter, and therefore, the shallow range is not considered in this article (but still included in the simulation results for maintaining context between the modeled radargram and surface imagery). Accordingly, a Hertzian-dipole radiation source is considered appropriate for imaging deep structures close to nadir direction, instead of employing an elaborate antenna model. Reception is also done at a single Yee-cell, separated by ten cells from the source.

In post-processing, corrections are made for a presumed 150 dB system dynamic range (SDR) for RIMFAX. Evaluating the signal-to-noise ratio (SNR) from the radar equation, SDR is defined to encompass the system-specific parameters [39], as in

$$\mathrm{SNR} \approx \mathrm{SDR} \times \left[\frac{\lambda_0^2 \, e^{-4(\alpha_i + \alpha_v)(R - R_s)} \, T_s^{\downarrow} \, T_s^{\uparrow} \, \Gamma_{\mathrm{target}}}{(4\pi)^2 (2R)^2} \right]. \quad (2)$$

The last term contains variables related to geometrical spreading (R = range), medium properties (α_i = intrinsic attenuation, α_v = volume loss), transmission losses along the propagation path (T_S = surface transmission), reflection at the target (Γ_{target}= target reflectivity), as well as the wavelength in free air (λ_0), and the antenna height above ground (R_S). Transmission at the surface is included because the antenna is air-coupled and mounted 60 cm above the ground. The approximate equality in (2) derives from a near-nadir approximation with normal incidences at plane, specular boundaries, enabling the target to be expressed in terms of the Fresnel reflectivity [40].

During numerical simulations, parameters in the last term of (2) are accounted for through the FDTD solution of Maxwell's equations, while the radar system parameters are not included. To imitate RIMFAX' detection limit, signals below the SDR are concealed by setting a fictive noise level (N_0) according to a matched filter receiver

$$\frac{P_t}{N_0/2} \approx \mathrm{SDR} \rightarrow \; N_0 \approx \frac{2P_t}{\mathrm{SDR}}, \quad (3)$$

where P_t is the power of the transmitted pulse. Fig. 2 presents a schematic overview of the deep operation mode and signal levels that are simulated.

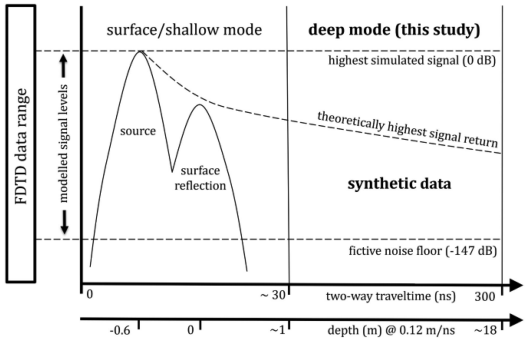

Fig. 2. Schematic view of modeled radar acquisition. The upper meter (~30 ns) containing the transmitted wave, surface reflection, and other shallow reflections is not considered in the deep mode due to gating in FMCW acquisition. Total recording length is set to 300 ns (~18 m at 0.12 m/ns). Left axes display how simulated signal levels fall within the FDTD data range. Simulated signal levels below -147 dB are muted, according to the presumed detection limit for RIMFAX (SDR = 150 dB). The synthetic radargram will consist of data bounded by the fictive noise floor and a theoretically highest signal return due to geometrical spreading.

III. Surface and Subsurface Models

A. Geological Setting

Jezero crater ($D = 50$ km), selected as the landing site for the Mars 2020 mission, is located in the Nili Fossae region on the northwestern edge of the ~3.9 Ga Noachian-aged Isidis impact basin ($D = 1900$ km) [41], [42]. Extensive breccias and impact melts have been noted in the area [43], [44] as well as younger fluvial channels [45] and mineralogical composition indicating early aqueous alteration [46]–[48]. To the west is the Hesperian-aged volcanic complex of Syrtis Major Planum, with possible lava flows extending into the Nili Fossae region [49].

Jezero is a complex impact crater with a central peak [50] that has been severely eroded. Large amounts of scree, mass flows, density current, and melt rock most likely formed during the crater excavation and various stages of modification, comparable to terrestrial impacts where the aqueous origin is still discussed [51], [52]. Based on general depth/diameter ratios for complex craters [53], Jezero may have experienced a ~1 km thick post-impact succession [32], [54].

Light-toned outcrops are present on the Jezero crater floor, displaying a rough surface expression with varying topography and polygonal fractures at a variety of scales. This lithology has been interpreted to be the lowest visible unit among the post-impact deposits in Jezero Crater [26], [32] and has been called various names in the published literature; however, in this article, it is referred to as the light-toned floor (LTF). Olivine and Mg-carbonate signatures are detected in visible to near-infrared (VNIR) reflectance spectra of this unit [26], [54], and possibly related to regional carbonate-bearing exposures observed more broadly in the Nili Fossae region [26], [29]. A summary of formation scenarios is found in [55] and references therein.

Most likely in late Noachian time, a closed basin with standing water was contained within the crater, which later developed

into a hydrologically open lake [45]. Two possible inlet valleys entering the crater through the northern and western rims were feeding the lake system, while a breach in the eastern rim formed the major outlet. Located at the mouth of each inlet valley are deeply eroded deltaic deposits still present with a morphology reminding of fluvial-dominated deltas [32], [45]. These were deposited on top of the LTF [26], [54]. Phyllosilicates and carbonaceous material detected in VINR data indicate early aqueous alteration [54], likely due to detrital deposited material sourced from the nearby Noachian terrain [26].

B. Disputed Mafic Unit

Interpreted to be the youngest consolidated lithology in Jezero, the relatively flat and dark-toned mafic unit appears to onlap older strata within Jezero crater [26], [32]. It displays varying morphological expressions, ranging from smooth to rough, that may be caused by a nonuniform distribution of a mantling material, possibly unconsolidated, overlying the unit's more cratered surfaces [27], [28], whereas Kah *et al*. [56] proposed that the variation in smoothness reflects a sporadic thin veneer of dark-toned material, mantling the underlying rough LTF.

VNIR spectra of the unit show mafic mineralogy (olivine and pyroxene content), which indicates a possible volcanic origin [26], [33]. Morphological observations supporting a low-viscous lava flow origin are a relatively smooth and flat crater-retaining surface and lobating margins embaying neighboring outcrops [26], [32]. As noted by several authors [29], [33], however, alternative formational hypothesizes as a tephra or volcanoclastic deposit cannot be ruled out based on orbital observations alone, in particular, due to similarities between the mafic unit on the crater floor and a regional unit on the rim and outside of Jezero crater.

Based on crater counting, estimated ages for the mafic unit range from 3.45 Ga in the Neukum system [57] to 2.6 Ga [58] and 1.4 Ga [32] in the Hartmann system. However, Cofield and Stack [27] emphasized that caution needs to be applied in case the unit is covered by a thin mantle, and age estimates may only be correct in certain areas. Kah *et al*. [56] advocated that a thin mantle of dark-toned material could be transparent to older craters retained from the underlying LFT, not the mafic unit itself.

Schon *et al*. [32] proposed emplacement of the mafic unit posterior to the cessation of fluvial activity, suggesting the delta was partially eroded prior to possible volcanic emplacement. This is consistent with Goudge *et al*. [57] who studied volcanic resurfacing in Martian open-basin lakes and found no evidence of water interaction in the Jezero crater. Furthermore, buffered crater counts along the valleys that once fed the Jezero paleolake indicate that the fluvial system seceded in late Noachian $\sim$3.8 Ga in the Neukum system [59]. Contrarily, Ruff [60] suggested inverse stratigraphic relationships due to the lack of erosional contact toward the delta deposits. Alternatively, Ruff [60] also indicated that this could be caused by a delta unit less prone to erosion than the mafic material. Explaining this discrepancy, Horgan *et al*. [33] advocated a more interfingered relationship, where parts of the delta could have been deposited after emplacement of the mafic unit.

The vertical extent of the mafic unit is largely unknown, although several thickness estimates have been made along its margins: Schon *et al*. [32] estimated 10–30 m, Goudge, *et al*. [26] estimated $<$ 10 m, and Shahrzad *et al*. [58] estimated $\sim$13 m. Furthermore, in the proposed scenario with the mafic unit as a thin mantling layer, Kah *et al*. [56] suggest that measuring the escarpment height only demonstrates minimum erosion of the LTF along the margins. The mafic unit may have acted as a cap, while topographically higher and previously uncovered parts of the LTF have eroded, resulting in the apparent erosional embayment structure.

C. Acquisition Traverse and Subsurface Model

A selected traverse across the mafic unit runs close to the nominal mission traverse [61] and includes several geological units identified from orbital observations. The traverse is presented in Fig. 3(a), plotted on top of orbital imagery from Dickson *et al*. [62]. To the SSE is the LTF with a rough surface expression and varying relief. The line extends across the darker toned and relatively flat mafic unit, where a range of distinct surface expressions can be seen to the east and west of the line, from smooth to rough. Here, it also crosses over a 2-m wide linear fracture and a 10-m diameter sized impact crater. Toward the NNW, the line approaches $\sim$50-m tall erosional scarp of the western delta deposits.

A hypothesized subsurface model is constructed along the traverse, with the mafic unit modeled as an accumulation of basaltic lava flows embaying the delta deposits and the LTF [see Fig. 3(c)]. Prodelta deposits are assumed NNW of the line based on Goudge *et al*. [63], whereas numerous formation scenarios and compositions have been proposed for the LTF. In this article, the "Comanche" outcrops in Columbia Hills are used as a proxy due to their comparable composition within VNIR constraints to exposures of carbonate-bearing rocks in the Nili Fossae region [64]. Mars Exploration Rover Spirit studied these outcrops and interpreted them to be volcaniclastics with 16 to 34 weight percent carbonaceous material, possibly cemented through hydrothermal activity.

A series of simplifications are made during the construction of the subsurface model. Presuming a general subsurface model for low latitude regions, the regolith is composed of dry sedimentary and volcanic rocks [65], [66] where attenuation of radar waves is dominated by volume losses and intrinsic losses due to Fe-/Ti-oxide content. Magnetic properties are assumed negligible and the dielectric properties are assumed uniformly distributed within each geological unit (the dielectric constant and conductivity are invariant for each unit). Temporal variations and their effect on the regolith's dielectric properties, due to temperature changes [15] or atmospheric interaction [14], [67], are not considered.

The mafic unit is ascribed typical properties of basalts ($\varepsilon' = 6$ and $\varepsilon'' = 0.25$ at the 250 MHz center frequency), supported by SHARAD-observations confirming that properties of Martian lava flows are comparable to their terrestrial and

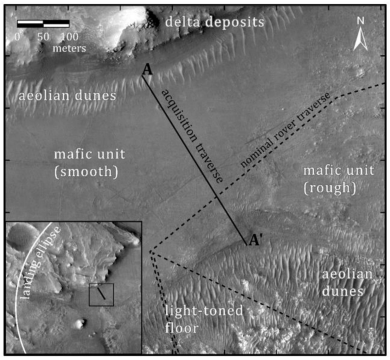

	Aeolian dunes	Surficial sands	Mafic unit	Delta deposits	Light-toned floor
ε′	2.1	2.4	6.0	3.5	4.5
ε″	0.06	0.07	0.25	-	-

(b)

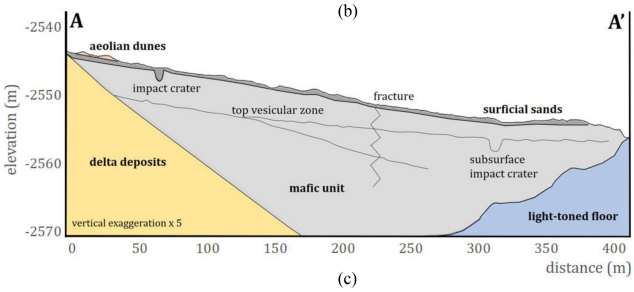

Fig. 3. (a) Map with the acquisition traverse in this article (A-A': solid line) together with the nominal Mars 2020 rover traverse (dashed line). Annotations describe units identified in photogeologic mapping. The image embedded in the lower-left corner of the map gives a regional context of the map frame and acquisition traverse. (b) Parameters as defined for each unit. The dielectric loss factors are listed for the 250 MHz center frequency. (c) Schematic view of the cross-sectional model over which radar sounding is simulated.

lunar counterparts [68]. A great variety of flow morphologies exist [69], but from the crater floor's relatively flat topography and interpreted embaying features [26], [32], we assume fairly laterally homogeneous basaltic flows with the typical tripartite internal structure [70]: 1) a less dense top vesicular zone (TVZ); 2) a compact middle zone; and 3) a thin basal section with some vesicles. In the subsurface model, separate flows are divided by the TVZ with up to ∼30% porosity increase, similar to emplaced low viscous flows on Earth. This implies a decrease in the dielectric constant over this zone ($\varepsilon' = 4$–6), in agreement with the relationship to bulk density for dry rocks. The upper reflector of the TVZ is assigned ±0.5 m fractal roughness intends to replicate the surface expression of the crater floor's rougher parts, while the lower boundary is constructed with gradual and randomly decreasing porosity.

The subsurface model includes the 10 m diameter impact crater (60 m along the traverse) and 2 m wide linear fracture (220 m along the traverse), which is observed in surface imagery, as well as an idealized crater structure in the subsurface (310 m along the traverse). Both craters are constructed with a 0.2 depth/diameter ratio and with gradual and randomly varying dielectric constants in the surrounding deformation zone. The fracture is modeled similarly but as a 2-m thick vertically extending deformation zone. In all cases, dielectric properties are assigned according to a maximum ∼10% fracture induced porosity.

Sedimentary porosities will in general be higher on Mars than for terrestrial equivalents due to lower surface gravity and weakened mechanical compaction [71]. However, high amounts of cementation have been observed on Mars [72], which in turn can drastically reduce porosities. As a first estimate, rather low dielectric values are assumed for the prodelta deposits ($\varepsilon' = 3.5$) and cemented volcaniclastic rocks ($\varepsilon' = 4.5$). As only their top surfaces are considered, intrinsic and volume losses are disregarded together with any internal layering. The top surface of the LTF is generated by extrapolating its wavy surface topography into the ground, with additional ±0.5 m fractal roughness, while the delta has a smooth and dipping top surface with ±0.1 m fractal roughness. The aeolian dunes and the unconsolidated layer mantling the mafic unit are assumed to have low densities (1.1 and 1.3 g/cm^3, respectively) in the range of *in situ* measurements done by the Viking lander [73]. This corresponds to low dielectric constants ($\varepsilon' = 2.1$ and $\varepsilon' = 2.4$) and losses ($\varepsilon'' = 0.06$ and $\varepsilon'' = 0.07$, at the center frequency) according to measurements of the soil simulant JSC-1 [15].

IV. Results and Discussion

The synthetic radargram presented in Fig. 4(a) displays the simulated radar soundings where each trace has a recorded length of 300 ns (the equivalent of ∼18 m depth, assuming a constant medium velocity of 0.12 m/ns). Traces have been applied a dewow-filter and gain before stacked and corrected for time-zero and topography. The aeolian dunes and the unconsolidated layers are modeled with thicknesses up to 0.5 m, so detection of these units is not considered in the deep operation mode. They still have a great influence on underlying reflectors, as reflectors are observed shifted vertically according to the amount of low-density overburden. This is particularly apparent below the filled impact crater (60–70 m along the traverse), where imaging of the structures below is distorted [Fig. 4(b)].

Distinct reflections from layering within the mafic unit can be detected, with the TVZ (top vesicular zone) displaying a strong top reflection that grades into weaker incoherent reflections [see Fig. 4(a)–(d)]. In general, the well-known tripartite structure can be difficult to detect due to the gradual density variations within individual flows, although separate lava flows are distinguished in GPR surveys on Earth [7], [16]. In the simulation results, the TVZ-layer thickness can be inferred from the vertical extent of scattering. On Mars, acquiring such information could reveal

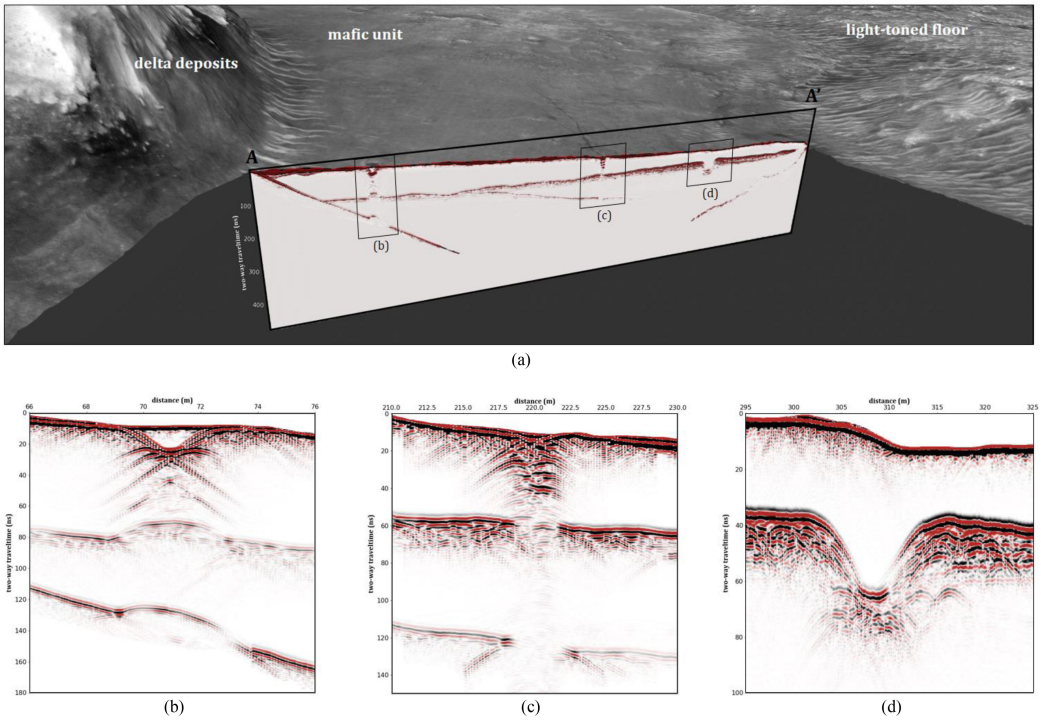

Fig. 4. (a) Synthetic radargram displays the results from modeling radar sounding over the 400 m acquisition traverse (A-A'). Note that the radargram is aligned with the topography, but its vertical axis below the surface is in two-way travel time [ns] and has a vertical exaggeration of x2.0, assuming a constant medium velocity of 0.12 m/ns. Image zooms in (a) on the impact crater, (b) on the vertical fracture, and (c) on the subsurface crater structure.

clues about paleoenvironmental conditions due to how the internal vesicularity solidifies during cooling and is affected by the confining pressure [74]. In general, the TVZ in Martian lava flows should be thinner than on Earth due to lower atmospheric pressure [75] as the distribution of vesicles within flows shows a good fit with the ideal-gas law. Confining pressure should also be prominent for lava flows emplaced in an aqueous environment, although other structures and flow morphologies could then be apparent [69]; and no evidence has been found to support fluvial and/or lacustrine activity within Jezero coeval with emplacement of the hypothesized lava flow [57]. Studying detection of TVZ-thickness in more detail, however, is outside the scope of this article, which could require comparison with a radiative-transfer model or with a GPR field survey on Earth.

Image distortion is observed where the acquisition line crosses the linear fracture (∼220 m along the traverse) [see Fig. 4(c)]. The fracture is clearly visible from the highly scattering appearance in the radargram, but its vertical extent is difficult to constrain due to high volume loss and recorded clutter. At 300–315 m along the traverse, the general shape of the subsurface crater is resolved in the simulations [see Fig. 4(d)]. The image is not a typical "bow-tie," as expected from off-nadir reflections when sounding over concave structures, but rather a collection of diffractions below the concavely shaped TVZ.

In Fig. 5(a) and (c), there are clear distinctions between the rather plane reflections of the dipping delta deposits and the rougher LTF surface, where the latter results in many diffractions collectively forming an undulating and slightly incoherent reflection. The maximum depth of detection is compared with calculations according to (2) [see Fig. 5(b) and (d)], verifying that returned signal levels are correctly simulated and within range of plane-wave theoretical estimates. Due to a large velocity difference between the crater floor and the delta deposits, detection of the top delta reflector is achievable down to ∼16 m in the simulations. A smaller velocity change toward the LTF, together with an undulating surface that further distorts imaging, makes detection possible down to ∼14 m. The discrepancy between modeling results and calculations exists as the latter does not account for a broadband source wavelet, complex overburden, volume losses through the TVZ, off-nadir reflections from dipping and rough interfaces, etc.

A. Alternative Formation Scenarios for the Mafic Unit and Implications for Radar Sounding

The character of layering within pyroclastic or volcaniclastic deposited material is very different from structures within a succession of lava flows. Radar sounding over deposited material

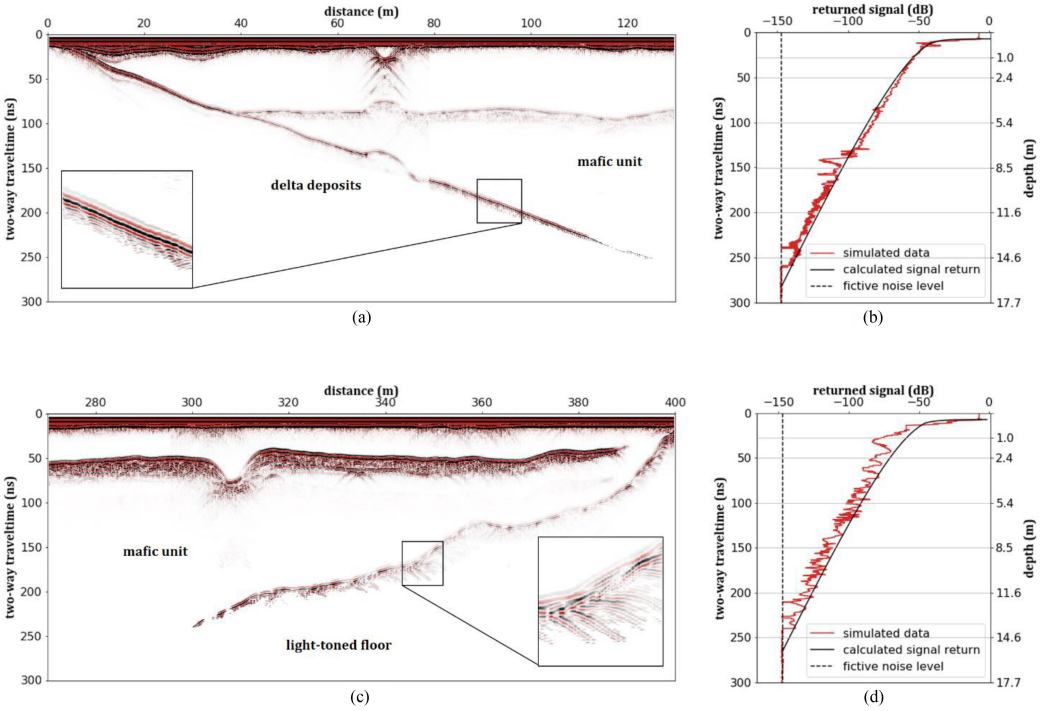

Fig. 5. Detection of lithological boundaries through the mafic unit, where left images show modeling results over the (a) delta deposits and (c) LTF unit. Radargrams are displayed in two-way traveltime below time zero. For each radargram, there is a zoomed-in window highlighting the contact. (b), (d) Corresponding signal powers (red line) measured over the reflections, plotted together with plane-wave calculations of SNR/SDR (black line) according to (2). Depth axes correspond to a constant medium velocity of 0.12 m/ns for a radar located 0.6 m above ground. The detection limit is at the -147 dB noise level defined according to (3).

can detect decimetre-scale bedding and stratigraphic geometries indicative of the depositional environment and mechanism [5]. While traversing over a pyroclastic or volcaniclastic mafic unit, RIMFAX could possibly detect individual layers based on bulk density differences and constrain corresponding bedding geometries. In the case of a pyroclastic material, GPR is furthermore capable of detecting the degree of welding/consolidation within a deposit [17], [76], which in turn could be related to the physical and thermal properties of the materials [77].

Pyroclastic deposits on Mars could be very porous, as Carter *et al*. [78] observed when studying subsurface reflections from SHARAD-sounding over the Medusae Fossae Formation. They identified possible low-density welded or interlocked pyroclastic deposits, with an estimated bulk dielectric constant of $\sim$3.0 for the formation's upper hundreds of meters. Their prediction corresponds to very high porosities despite the formation's capability of sustaining steep-sided yardangs and ridges seen in orbital imagery. In general, dry, deposited rocks on Earth will have lower densities and dielectric constants than lava flows. The low surface gravity on Mars further weakens the effect of mechanical compaction so that volcaniclastic and pyroclastic deposits are on average expected to have even lower densities. This is in contrast to Martian lava flows with electromagnetic properties similar to that of Earth and the moon, and even slightly higher due to possible reduced vesicularity. Sounding over a pyroclastic or volcaniclastic material should for that reason be affected by noticeable low dielectric values (e.g., $\varepsilon' = 3$-5) compared to sounding over lava flows with typically high values ($\varepsilon' = 6$-9), although pyroclastic welding or cementation in volcaniclastic material could increase the dielectric constant and reduce this gap.

Drawing on the experience from the space-borne radars on Mars, predicting penetration depths in front of data acquisition is very difficult due to the unknown subsurface environment [79]; so maximum penetration depths in this article (see Fig. 5) are included to verify the numerical simulations, not to give quantitative estimates. However, penetration depths depend upon overburden properties, especially the amount of intrinsic attenuation and volume losses. This implies that the characteristically lower dielectric constants expected for tephra or volcaniclastic deposits, compared to lava flows, would in general yield greater detection depths. Not considering volume losses, this prediction is valid for dry rocks where the pore space is not occupied by brine or ice, and attenuation is caused by mineral constituents in the rock (e.g., Ti/Fe-oxide content). That is, intrinsic attenuation for a dry porous rock ($\alpha_i = \pi\varepsilon''/\omega\sqrt{\varepsilon'}$; low-loss approximation

for $\varepsilon''/\varepsilon' << 1$) will be less than for a more dense rock of similar composition, if air fills pore spaces and lowers the magnitudes of the bulk dielectric constant and loss factor proportionally (assuming the ratio $\varepsilon''/\varepsilon'$ remains unchanged for each frequency under consideration).

B. Validity of a Dry Subsurface Model Assumption

Water content in rocks and sediments strongly affects the dielectric constant and loss factor. Dry rocks were assumed in this article; however, the subsurface environment on Mars is largely unknown and the presence of ice and brines in the near-surface could be possible, see, e.g., Stamenković *et al*. [1] and references within. Furthermore, the Phoenix lander measured diurnal variations in the dielectric constant at the surface, indicating possible atmospheric water uptake in the regolith [14] that could be consistent with a salty mixture in the ground affecting the dielectric properties over the course of a sol [67]. Perhaps GPR-imaging capabilities and penetration depths will change accordingly, which should be taken into concern during data interpretation, while also making it possible to study water exchange between the atmosphere and regolith through radar sounding.

Bound water in rocks and sediments, especially clays, is another potential aqueous source in Jezero, where phyllosilicate-signatures in VNIR-data indicate smectite carrying delta deposits. It has been hypothesized that bound water could be the reason behind the great radar loss experienced by space-borne radars orbiting Mars [79], in which case, an increased dielectric loss factor would be noticeable through sounding with RIMFAX. In accordance with measurements of Martian soil simulant JSC-1 [15], in this article bound water was included for the aeolian dunes and unconsolidated material, but only in thin surficial accumulations that did not distinctly affect imaging. If, however, high intrinsic attenuation would be detected over larger successions of smectite-rich delta deposits, radar sounding could turn out to be an appropriate tool for identifying and locating *in situ* water resources at the landing site.

V. Conclusion

A synthetic radargram was generated along a carefully selected acquisition traverse on the Jezero crater floor, enabling assessment of internal structures and detection of adjacent lithologies in a hypothesized geological setting. The modeling workflow shows the potential for assisting interpretation of data acquired on Mars by placing simulated radar sounding in the correct spatial context and by accurately estimating the returned signal levels. Comparing modeling results with actual RIMFAX-recordings could, therefore, help constrain subsurface geometries and electromagnetic properties. From orbital observations, uncertainties are ascribed stratigraphic relationships, lithological formations, as well as the electromagnetic properties of each geological unit; thus, decisive estimates of imaging capabilities are therefore not possible to make. Still, noticeable differences are expected between sounding over lava flows compared to tephra or volcanoclastic lithology, due to distinct internal structures and, in particular, due to how the low surface gravity on Mars affects sediment and rock generation and, consequently, the electromagnetic properties.

Acknowledgment

The authors would like to thank Geocap AS for granting an academic license for their software Geocap Desktop used in this research.

References

[1] V. Stamenković *et al.*, "The next frontier for planetary and human exploration," *Nat. Astron.,* vol. 3, no. 2, pp. 116–120, Jan. 2019.
[2] S. Hamran *et al.*, "Radar imager for mars' subsurface experiment.RIMFAX," in *Space Science Reviews*, vol. 216, no. 8, p. 128, 2020, doi: 10.1007/s11214-020-00740-4.
[3] B. Zhou *et al.*, "The subsurface penetrating radar on the rover of china's mars 2020 mission," in *Proc. 16th Int. Conf. Ground Penetrating Radar*, 2016. pp. 1–4.
[4] V. Ciarletti *et al.*, "WISDOM GPR designed for shallow and high-resolution sounding of the martian subsurface," *Proc. IEEE,* vol. 99, no. 5, pp. 824–836, May 2011.
[5] G. S. Baker and H. M. Jol, *Stratigraphic Analyses Using GPR*. Boulder, CO, USA: Geological Soc. Amer., 2007.
[6] J. K. Russell and M. V. Stasiuk, "Characterization of volcanic deposits with ground-penetrating radar," *Bull. Volcanol.,* vol. 58, no. 7, pp. 515–527, 1997.
[7] G. Olhoeft *et al.*, "Hot and cold lava tube characterization with ground penetrating radar," in *Proc. 8th Int. Conf. Ground Penetrating Radar*, 2000, pp. 482–487.
[8] G. Simmons *et al.*, "Surface electrical properties experiment," *Nat. Aeronaut. Space Admin.*, Washington, DC, USA, Apollo 17, Prelim. Sci. Rep. 330, 1973, p. 15.
[9] L. Xiao *et al.*, "A young multilayered terrane of the northern mare imbrium revealed by chang'E-3 mission," *Science,* vol. 347, no. 6227, 2015, Art. no. 1226.
[10] C. Li *et al.*, "The moon's farside shallow subsurface structure unveiled by chang'e-4 lunar penetrating radar," *Sci. Adv.,* vol. 6, no. 9, 2020, Art. no. eaay6898.
[11] M. J. Campbell and J. Ulrichs, "Electrical properties of rocks and their significance for lunar radar observations," *J. Geophysical Res.,* vol. 74, no. 25, pp. 5867–5881, 1969.
[12] G. R. Olhoeft and D. W. Strangway, "Dielectric properties of the first 100 meters of the moon," *Earth Planet. Sci. Lett.,* vol. 24, no. 3, pp. 394–404, Jan. 1975.
[13] F. T. Ulaby *et al.*, "Microwave dielectric properties of dry rocks," *IEEE Trans. Geosci. Remote Sens.*, vol. 28, no. 3, pp. 325–336, May 1990.
[14] A. Zent *et al.*, "Initial results from the thermal and electrical conductivity probe (TECP) on Phoenix," in *J. Geophysical Research: Planets.*, vol. 115, no. E3, 2010, doi: https://doi.org/10.1029/2009JE003420.
[15] D. Stillman and G. Olhoeft, "Frequency and temperature dependence in electromagnetic properties of martian analog minerals," *J. Geophysical Res., Planets,* vol. 113, no. E9, 2008, doi: 10.1029/2007JE002977.
[16] E. Heggy *et al.*, "Ground-penetrating radar sounding in mafic lava flows: Assessing attenuation and scattering losses in Mars-analog volcanic terrains," *J. Geophysical Res., Planets,* vol. 111, no. E6, 2006, doi: 10.1029/2005JE002589.
[17] R. E. Grimm *et al.*, "Absorption and scattering in ground-penetrating radar: Analysis of the bishop tuff," *J. Geophysical Res., Planets,* vol. 111, no. E6, 2006, doi: 10.1029/2005JE002619.
[18] R. B. Hargraves *et al.*, "The viking magnetic properties experiment: Primary mission results," *J. Geophysical Res.,* vol. 82, no. 28, pp. 4547–4558, 1977.
[19] S. F. Hviid *et al.*, "Magnetic properties experiments on the mars pathfinder lander: Preliminary results," *Science,* vol. 278, no. 5344, pp. 1768–1770, 1997.
[20] M. B. Madsen *et al.*, "Overview of the magnetic properties experiments on the mars exploration rovers," *J. Geophysical Res., Planets,* vol. 114, no. E6, 2009, doi: 10.1029/2008JE003098.
[21] B. Langlais *et al.*, "Crustal magnetic field of mars," *J. Geophysical Res., Planets,* vol. 109, no. E2, 2004, doi: 10.1029/2003JE002048.
[22] A. Mittelholz *et al.*, "The mars 2020 candidate landing sites: A magnetic field perspective," *Earth Space Sci.,* vol. 5, no. 9, pp. 410–424, 2018.

[23] G. Picardi *et al.*, "Radar soundings of the subsurface of mars," *Science,* vol. 310, no. 5756, 2005, Art. no. 1925.

[24] R. Seu *et al.*, "SHARAD sounding radar on the mars reconnaissance orbiter," *J. Geophysical Res., Planets,* vol. 112, no. E5, May 2007, doi: 10.1029/2006JE002745.

[25] G. A. Morgan *et al.*, "Radar investigations of the mars 2020 rover landing sites," in *Proc. 49th Lunar Planet. Sci. Conf.*, 2018, Paper 1404.

[26] T. A. Goudge *et al.*, "Assessing the mineralogy of the watershed and fan deposits of the jezero crater paleolake system, mars," *J. Geophysical Res., Planets,* vol. 120, no. 4, pp. 775–808, 2015.

[27] S. M. Cofield and K. M. Stack, "Geologic mapping and stratigraphic analysis of a candidate mars 2020 landing site: Jezero crater, mars," in *Proc. 49th Lunar Planet. Sci. Conf.*, 2018, Paper 2563.

[28] K. M. Stack *et al.*, "Photogeologic map of the perseverance rover field site in jezero crater constructed by the mars 2020 science team," in *Space Science Reviews*, vol. 216, no. 8, 2020, Art. no. 127, doi: 10.1007/s11214-020-00739-x.

[29] V. Z. Sun and K. M. Stack, "Understanding the continuity of regional units in the mars 2020 jezero and northeast syrtis regions: Implications for the origin of the mafic unit(s)," in *Proc. 50th Lunar Planet. Sci. Conf.*, 2019, Paper 2271.

[30] K. L. Tanaka *et al.*, "Assessment of planetary geologic mapping techniques for mars using terrestrial analogs: The SP mountain area of the san francisco volcanic field, arizona," *Planet. Space Sci.,* vol. 57, no. 5, pp. 510–532, May 2009.

[31] K. M. Stack *et al.*, "Comparing orbiter and rover image-based mapping of an ancient sedimentary environment, aeolis palus, gale crater, mars," *Icarus,* vol. 280, pp. 3–21, Dec. 2016.

[32] S. C. Schon *et al.*, "An overfilled lacustrine system and progradational delta in jezero crater, mars: Implications for noachian climate," *Planet. Space Sci.,* vol. 67, no. 1, pp. 28–45, Jun. 2012.

[33] B. H. N. Horgan *et al.*, "The mineral diversity of jezero crater: Evidence for possible lacustrine carbonates on mars," *Icarus*, vol. 339, Nov. 2019, Art. no. 113526.

[34] B. Wood *et al.*, "BGS groundhog desktop geoscientific information system external user manual," Brit. Geol. Survey, Nottingham, U.K., Rep. OR/15/046, 2015.

[35] C. Warren *et al.*, "gprMax: Open source software to simulate electromagnetic wave propagation for ground penetrating radar," *Comput. Phys. Commun.,* vol. 209, pp. 163–170, Dec. 2016.

[36] K. Yee, "Numerical solution of initial boundary value problems involving maxwell's equations in isotropic media," *IEEE Trans. Antennas Propag.,* vol. 14, no. 3, pp. 302–307, May 1966.

[37] K. S. Kunz and R. J. Luebbers, *The Finite Difference Time Domain Method for Electromagnetics*. Boca Raton, FL, USA: CRC Press, 1993.

[38] A. Taflove and S. C. Hagness, *Computational Electrodynamics: The Finite-Difference Time-Domain Method*. Norwood, MA, USA: Artech house, 2005.

[39] S. E. Hamran *et al.*, "Ground penetrating synthetic pulse radar: Dynamic range and modes of operation," *J. Appl. Geophys.,* vol. 33, no. 1, pp. 7–14, Jan. 1995.

[40] F. Uaby and D. Long, *Microwave Radar and Radiometric Remote Sensing*. Norwood, MA, USA: Artech House, 2015, pp. 201–203.

[41] S. C. Werner, "The early martian evolution—Constraints from basin formation ages," *Icarus,* vol. 195, no. 1, pp. 45–60, May 2008.

[42] C. I. Fassett and J. W. Head, "Sequence and timing of conditions on early mars," *Icarus,* vol. 211, no. 2, pp. 1204–1214, Feb. 2011.

[43] J. F. Mustard *et al.*, "Mineralogy of the nili fossae region with OMEGA/Mars express data: 1. Ancient impact melt in the isidis basin and implications for the transition from the noachian to hesperian," *J. Geophysical Res., Planets,* vol. 112, no. E8, 2007, doi: 10.1029/2006JE002834.

[44] J. F. Mustard *et al.*, "Composition, morphology, and stratigraphy of noachian crust around the isidis basin," *J. Geophysical Res., Planets,* vol. 114, no. E2, 2009, doi: 10.1029/2009JE003349.

[45] C. Fassett and J. W. Head, "Fluvial sedimentary deposits on mars: Ancient deltas in a crater lake in the nili fossae region," *Geophysical Res. Lett.,* vol. 32, no. 14, 2005.

[46] F. Poulet *et al.*, "Phyllosilicates on mars and implications for early martian climate," *Nature,* vol. 438, no. 7068, pp. 623–627, Dec. 2005.

[47] B. L. Ehlmann *et al.*, "Orbital identification of carbonate-bearing rocks on mars," *Science,* vol. 322, no. 5909, pp. 1828–1832, 2008.

[48] B. L. Ehlmann *et al.*, "Identification of hydrated silicate minerals on mars using MRO-CRISM: Geologic context near nili fossae and implications for aqueous alteration," *J. Geophysical Res., Planets,* vol. 114, no. E2, 2009, doi: 10.1029/2009JE003339.

[49] H. Hiesinger and J. W. Head, "The syrtis major volcanic province, mars: Synthesis from mars global surveyor data," *J. Geophysical Res., Planets,* vol. 109, no. E1, 2004, doi: 10.1029/2003JE002143.

[50] N. Barlow, "A review of martian impact crater ejecta structures and their implications for target properties," in *Large Meteorite Impacts III*, vol. 384. Boulder, CO, USA: Geological Soc. Amer., 2005, pp. 433–442.

[51] H. Dypvik *et al.*, "Mechanisms of late synimpact to early postimpact crater sedimentation in marine-target impact structures," in *Large Meteorite Impacts and Planetary Evolution IV*, vol. 465. Boulder, CO, USA: Geological Soc. Amer., 2010.

[52] H. Dypvik *et al.*, *Chesapeake Bay Impact Structure—Development of "Brim" Sedimentation in a Multilayered Marine Target*. Boulder, CO, USA: Geological Soc. Amer., 2018.

[53] J. B. Garvin *et al.*, "Craters on mars: Global geometric properties from gridded MOLA topography," in *Proc. 6th Int. Conf. Mars*, 2003, Paper 3277.

[54] B. L. Ehlmann *et al.*, "Clay minerals in delta deposits and organic preservation potential on mars," *Nat. Geosci.,* vol. 1, pp. 355–358, 2008.

[55] A. J. Brown *et al.*, "Olivine-carbonate mineralogy of the jezero crater region," *J. Geophysical Res., Planets,* vol. 125, no. 3, 2020, Art. no. e2019JE006011.

[56] L. Kah *et al.*, "Depositional relationships between crater floor materials in jezero crater, mars," in *Proc. 51st Lunar Planet. Sci. Conf.*, 2020, Paper 1301.

[57] T. A. Goudge *et al.*, "Constraints on the history of open-basin lakes on mars from the composition and timing of volcanic resurfacing," *J. Geophysical Res., Planets,* vol. 117, no. E12, 2012, doi: 10.1029/2012JE004115.

[58] S. Shahrzad *et al.*, "Crater statistics on the dark-toned, mafic floor unit in jezero crater, mars," *Geophysical Res. Lett.,* vol. 46, no. 5, pp. 2408–2416, 2019.

[59] C. I. Fassett and J. W. Head, "The timing of martian valley network activity: Constraints from buffered crater counting," *Icarus,* vol. 195, no. 1, pp. 61–89, May 2008.

[60] S. W. Ruff, "Investigating the floor of paleolake jezero by way of gusev crater," in *Proc. 4th Conf. Early Mars, Geologic, Hydrologic, Climatic Evol. Implic. Life*, 2017, Paper 3076.

[61] Mars 2020 Landing Site Working Group, "Mars 2020 science team assessment of jezero crater," in Presented at Fourth Landing Site Workshop for the Mars 2020 Rover Mission, [Online]. Available: https://marsnext.jpl.nasa.gov/workshops/2018-10/PRESENTATIONS/m2020_lsw_day2_19_Jezero_Final.pdf

[62] J. L. Dickson *et al.*, "A global, blended CTX mosaic of mars with vectorized seam mapping: A new mosaicking pipeline using principles of non-destructive image editing," in *Proc. 49th Lunar Planet. Sci. Conf.*, 2018, pp. 1–2.

[63] T. A. Goudge *et al.*, "Sedimentological evidence for a deltaic origin of the western fan deposit in jezero crater, mars and implications for future exploration," *Earth Planet. Sci. Lett.,* vol. 458, pp. 357–365, Jan. 2017.

[64] R. V. Morris *et al.*, "Identification of carbonate-rich outcrops on mars by the spirit rover," *Science,* vol. 329, no. 5990, pp. 421–424, 2010.

[65] S. M. Clifford, "A model for the hydrologic and climatic behavior of water on mars," *J. Geophysical Res., Planets,* vol. 98, no. E6, pp. 10973–11016, 1993.

[66] S. Piqueux *et al.*, "Widespread shallow water ice on mars at high latitudesand midlatitudes," *Geophysical Res. Lett.,* vol. 46, no. 24, pp. 14290–14298, 2019.

[67] D. E. Stillman and R. E. Grimm, "Dielectric signatures of adsorbed and salty liquid water at the phoenix landing site, mars," *J. Geophysical Res., Planets,* vol. 116, no. E9, Sep. 2011, doi: 10.1029/2011JE003838.

[68] L. M. Carter *et al.*, "Dielectric properties of lava flows west of ascraeus mons, mars," *Geophysical Res. Lett.,* vol. 36, no. 23, 2009, doi: 10.1029/2009GL041234.

[69] D. Jerram, "Volcanology and facies architecture of flood basalts," *Special Paper Geological Soc. Am,* vol. 362, pp. 119–132, Jan. 2002.

[70] S. Self *et al.*, "Emplacement of continental flood basalt lava flows," *Large Igneous Provinces, Continental, Ocean., Planet. Flood Volcanism*, vol. 100, pp. 381–410, Jan. 1997.

[71] K. W. Lewis *et al.*, "A surface gravity traverse on mars indicates low bedrock density at gale crater," *Science,* vol. 363, no. 6426, pp. 535–537, 2019.

[72] J. P. Grotzinger *et al.*, "Curiosity's mission of exploration at gale crater, mars," *Elements,* vol. 11, no. 1, pp. 19–26, 2015.

[73] H. J. Moore and B. M. Jakosky, "Viking landing sites, remote-sensing observations, and physical properties of martian surface materials," *Icarus,* vol. 81, no. 1, pp. 164–184, 1989.
[74] D. L. Sahagian and J. E. Maus, "Basalt vesicularity as a measure of atmospheric pressure and palaeoelevation," *Nature,* vol. 372, no. 6505, pp. 449–451, Dec. 1994.
[75] L. S. Crumpler, "MER field observations and analysis of vesicles in the gusev plains: Significance as records of emplacement environment," in *Proc. 36th Lunar Planet. Sci. Conf.*, 2005, Art. no. 2122.
[76] A. Rust and J. Russell, "Detection of welding in pyroclastic flows with ground penetrating radar: Insights from field and forward modeling data," *J. Volcanol. Geothermal Res.,* vol. 95, no. 1/4, pp. 23–34, 2000.
[77] S. L. Quane and J. K. Russell, "Ranking welding intensity in pyroclastic deposits," *Bull. Volcanol.,* vol. 67, no. 2, pp. 129–143, 2005.
[78] L. M. Carter *et al.*, "Shallow radar (SHARAD) sounding observations of the medusae fossae formation, mars," *Icarus,* vol. 199, no. 2, pp. 295–302, Feb. 2009.
[79] D. E. Stillman and R. E. Grimm, "Radar penetrates only the youngest geological units on mars," *J. Geophysical Res., Planets,* vol. 116, no. E3, 2011, doi: 10.1029/2010JE003661.

Sigurd Eide received the M.Sc. degree in geophysics, in 2014, from the University of Oslo, Norway, where he is currently working toward the Ph.D. degree in geophysics.

From 2014 to 2018, he was a Consultant within Marine Geophysics and Geographical Information Systems. His research interest include remote sensing and numerical modeling applied to geological exploration, in particular ground-penetrating radar and active-source seismic.

Svein-Erik Hamran received the M.Sc. degree in physics from the Norwegian University of Science and Technology, Trondheim, Norway, in 1984 and the Ph.D. degree in physics from the University of Tromø, Tromsø, Norway, in 1990.

He is currently a Professor with the Department of Technology Systems, University of Oslo. He is also the Principal Investigator of the Radar Imager for Mars subsurface eXperiment RIMFAX on the NASA Mars 2020 Perseverance Rover Mission and a Coprincipal Investigator on the WISDOM GPR experiment on the ESA ExoMars rover. His research interests include UWB radar design, radar imaging, and modeling in medical and ground-penetrating radar.

Henning Dypvik was born in Oslo, Norway. He received the Dr.philos. degree in geology from the University of Oslo, Norway, in 1985.

He is currently a Professor of Sedimentology and Petroleum geology with the University of Oslo. He has worked with field sedimentology and diagenetic analysis, in addition to detailed shale geochemistry. For the last 20 years, he has been involved in impact cratering and involved in the discoveries of the three Norwegian impact craters. His research interests include postimpact sedimentation.

Hans E. F. Amundsen received the M.Sc. and Ph.D. degree in volcanology and geochemistry from the University of Oslo, Norway, in 1987 and 1991, respectively.

He is currently a Geologist and the CEO with Vestfonna Geophysical AS, Kabelvåg, Norway. He is also a Long-Term Planner on Mars2020, Co-I on the RIMFAX GPR (Mars2020), and Co-I on the WISDOM GPR (ExoMars). His research interests include the are of scientific expertise covers volcanology, igneous- and sediment geochemistry, geochronology, organic geochemistry, development of rovers, payload instruments and planetary protection protocols, field geology and image analyses, sedimentology and basin evolution, and interpretation of seismic and electromagnetic data in subsurface imaging.

Paper II

Modeling FMCW Radar for Subsurface Analysis

Sigurd Eide, Titus Casademont, Øyvind Aardal, and Svein-Erik Hamran

Published in *IEEE Journal of Selected Topics in Applied Earth Observations and Remote Sensing*, 2022, volume 15, pp. 2998–3007. DOI: 10.1109/JSTARS.2022.3165135.

II

Modeling FMCW Radar for Subsurface Analysis

Sigurd Eide, Titus Casademont, Øyvind Lund Aardal, and Svein-Erik Hamran

***Abstract*—Determining subsurface properties through ground penetrating radar sounding can be challenging, especially in planetary exploration, where little is known about the terrain and additional observations are limited. Analysis and interpretation of data acquired with the Radar Imager for Mars' Subsurface Experiment (RIMFAX) could therefore be improved by in-detail comparison with forward modeling. RIMFAX transmits a frequency modulated continuous waveform and utilizes a stretch processing receiver, and we demonstrate how accurate modeling can be achieved through finite-difference time-domain simulations. As the simulation scheme do not allow for direct implementation of such radar system, this study presents the necessary steps in order to replicate the same transmitter and receiver characteristics. In particular, we investigate how the method holds for modeling sounding in a realistic subsurface medium with attenuating and dispersive properties, by comparing the results with analytical estimates. The modeling approach is also assessed through comparison with RIMFAX field test measurements.**

***Index Terms*—Finite-difference time-domain (FDTD), frequency modulated continuous wave (FMCW), ground penetrating radar (GPR), Radar Imager for Mars' Subsurface Experiment (RIMFAX).**

I. Introduction

IMAGING of geological layering and analysis of subsurface properties are among the principal applications of ground penetrating radar (GPR). In planetary exploration, means of constraining acquired GPR data are limited to surface observations, either from orbital imagery or by other payload instruments. This can be difficult and ultimately lead to controversy surrounding the results, as to whether actual subsurface structures have been detected or if it is rather system noise being misinterpreted [1], [2]. Additional insight can be obtained, however, by testing hypotheses and comparing with modeling, e.g., evaluating how the subsurface have affected reflection geometries and target responses in recorded radargrams. Forward modeling has been done in lunar exploration to assess interpreted subsurface model and electromagnetic media properties [3], as well as to assure adequate processing of acquired data [4]. Accordingly, modeling studies could be helpful for analyzing soundings from the Radar Imager for Mars' Subsurface Experiment (RIMFAX) [5] on the Perseverance rover mission, the first GPR to be operating from the surface of Mars.

In order to use modeling for analyzing subsurface properties, modeling should be able to reproduce the same spectral characteristics and target responses as would be acquired with the transmitter and receiver of a specific GPR system. RIMFAX is a frequency modulated continuous wave (FMCW) radar with a stretch processing receiver, operating in the 150–1200 MHz frequency range (see Hamran *et al.* [5] for detailed information about the instrument and acquisition modes). Among several modeling approaches [6], the finite-difference time-domain (FDTD) method has been largely adapted by the GPR-community with availability of open-source software [7]. For modeling pulsed radar systems, FDTD-simulations are excited by a copy of the transmitted waveform and reflections from the subsurface model are recorded. But this is not viable for FMCW radars due to high computational costs, as the duration of a FMCW sweep can be on the order of 100–1000 times longer than the waveform in pulsed radar. To the best of our knowledge, FMCW-implementation in FDTD has not previously been thoroughly investigated.

In this study, we demonstrate how the target response of RIMFAX and other FMCW stretch processing receivers can be obtained through FDTD-simulations and subsequent corrections, asserting that modeling can be used for in-detail subsurface analysis. The obstacle of long sweep times is overcome by conducting simulations with a short-duration broadband waveform and afterwards correcting for differences in the waveform frequency spectra, as well as incorporating effects due to antenna gain and receiver processing. This can be accomplished because acquisition, the subsurface model and receiver processing can be described in a linear time-invariant system, as described in the method section. Notably, we present modeling of radar sounding in realistic media with attenuation and dispersion properties, and verify the results by comparing with analytical estimates. Assessment of the modeling approach is also done through comparison with RIMFAX field test measurements.

II. Method

The method is subdivided into four sections. Section A describe the FMCW signal, Section B the FMCW stretch processing receiver, and Section C the FDTD-modeling corrections. Last, in Section D, an example demonstrates how FDTD-simulations with a short-duration broadband waveform are corrected to reproduce the same time domain result as a that of a long duration FMCW and a stretch processing receiver.

Manuscript received October 4, 2021; revised December 6, 2021 and January 31, 2022; accepted March 22, 2022. Date of publication April 5, 2022; date of current version April 27, 2022. *(Corresponding author: Sigurd Eide.)*

Sigurd Eide, Titus Casademont, and Svein-Erik Hamran are with the Department of Technology Systems, University of Oslo, 2007 Kjeller, Norway (e-mail: sigurd.eide@its.uio.no; titus.casademont@its.uio.no; s.e.hamran@its.uio.no).

Øyvind Lund Aardal is with the Department of Technology Systems, University of Oslo, 2007 Kjeller, Norway, and also with the Norwegian Defence Research Establishment (FFI), 2027 Kjeller, Norway (e-mail: o.l.aardal@its.uio.no).

Digital Object Identifier 10.1109/JSTARS.2022.3165135

This work is licensed under a Creative Commons Attribution 4.0 License. For more information, see https://creativecommons.org/licenses/by/4.0/

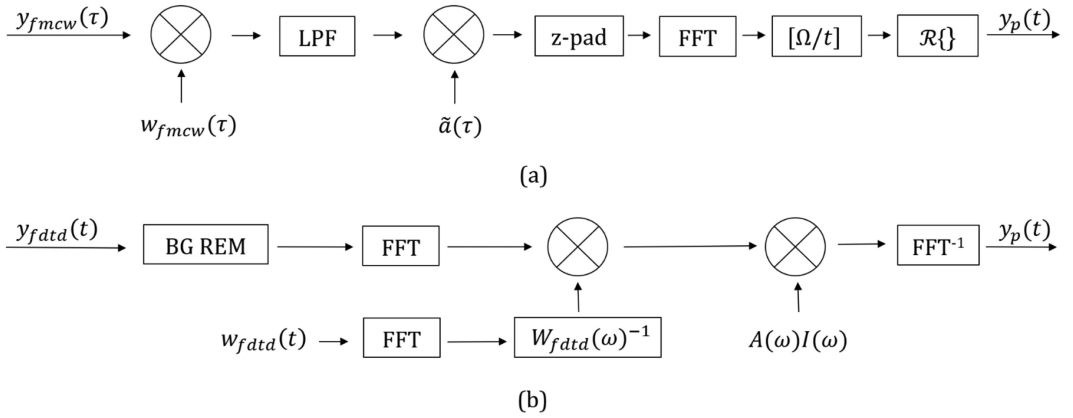

Fig. 1. Block diagrams of (a) stretch processing receiver and (b) FDTD-modeling corrections. Crossed circles indicate mixing or multiplication (not distinguishing between analog and digital operations). "LPF" is low pass filtering and "z-pad" is zero-padding/time-shifting. "FFT" and "FFT^{-1}" is the forward and inverse Fast Fourier Transform. $[\Omega/t]$ indicates variable substitution and $\Re\{\}$ symbolizes the operation of taking the real value of a complex signal. Background removal of FDTD-source effects is represented by "BG REM," while $W_{\text{fdtd}}(\omega)^{-1}$ is the deconvolution operator in frequency domain. Variables are as described in the text.

A. FMCW Signal

A linearly varying FMCW with start angular frequency Ω_0, bandwidth B, and sweep length T, can be written as

$$w_{\text{fmcw}}(\tau) = \tilde{i}(\tau) \exp j \left[\Omega_0 \tau + \pi \frac{B}{T} \tau^2 \right]. \tag{1}$$

The exponential term, containing the waveform oscillation, is multiplied with an instrument-specific correction term $\tilde{i}(\tau)$ that describes amplitude variations with frequency in the radiated signal. We refer to the time variable τ as "sweep-time," which is related to the timing during instrument acquisition.

Received reflections from N targets with two-way travel-time delays t_i are then written

$$y_{\text{fmcw}}(\tau) = \tilde{i}(\tau) \sum_{i=1}^{N} d_i \tilde{h}_i(\tau) \exp j \left[\Omega_0 (\tau - t_i) + \pi \frac{B}{T} (\tau - t_i)^2 \right] \tag{2}$$

where d_i is assumed frequency independent and corrects the amplitude for geometrical spreading and the target's radar cross section. For propagation in attenuating and dispersive media, reflected signals will besides have undergone frequency dependent alteration [8]–[10], here represented by the term $\tilde{h}_i(\tau)$ in sweep-time domain.

B. Stretch Processing Receiver

A stretch processing receiver as illustrated in Fig. 1(a), takes the received signal in (2) and conducts several operations to output a compressed result, i.e., the target responses. First, the received signal is mixed with the transmitted waveform and the product is passed through a low pass filter. These operations

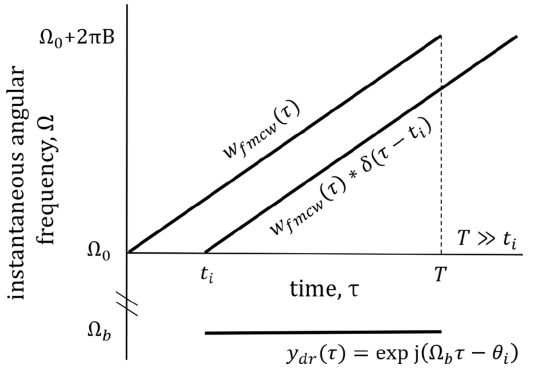

Fig. 2. Illustration of stretch processing and beat-frequency for a single reflection at t_i, where the reflected signal is a time-delayed copy of the transmitted waveform. $\delta(\tau)$ is the Dirac delta function.

produce the deramped signal [11]

$$y_{dr}(\tau) = \tilde{i}(\tau) \sum_{i=1}^{N} d_i \tilde{h}_i(\tau) \exp j \left[2\pi \frac{B}{T} t_i \tau - \theta_i \right] \tag{3}$$

where each target introduces a constant phase shift

$$\theta_i = -\Omega_0 t_i + \pi B t_i^2 / T \approx -\Omega_0 t_i \,. \tag{4}$$

The term $\pi B t_i^2 / T$ is known as the "residual video phase" and has a very small contribution. It is typical negligible in subsurface sounding where target delay times are relatively short compared to sweep lengths, as $\pi B t_i^2 / T \Omega_0 t_i \propto t_i / T \approx 0$.

The resultant deramped signal consists of "separate tones" denoted beat frequencies, $\Omega_b = 2\pi B t_i / T$, which correspond to the two-way travel-time delay t_i of each reflection. This principle is illustrated in Fig. 2 for a single reflection.

By zero-padding the beginning of the mixer output, effectively time-shifting the signal, the constant phase term (4) can be removed

$$y_{dr}(\tau) * \delta(\tau - t_s) = \tilde{i}(\tau) \sum_{i=1}^{N} d_i \tilde{h}_i(\tau) \exp j\left[\Omega_b(\tau - t_s) - \theta_i\right] = \tilde{i}(\tau) \sum_{i=1}^{N} d_i \tilde{h}_i(\tau) \exp j\left[\Omega_b \tau\right]. \quad (5)$$

We describe this through convolution ($*$) with the Dirac delta function and an appropriately chosen time shift, $t_s = \Omega_0\, T/2\pi B$.

Before zero-padding and transforming the mixer-output into frequency domain, an amplitude taper $\tilde{a}(\tau)$ is included to modify the target responses, lowering sidelobes at the cost of a broader mainlobe and reduced signal-to-noise ratio. It should be noted that there are options on how to apply this taper that could end up distorting the target responses, though negligible when FMCW sweep times are much longer than the target delays [11].

Employing that multiplication in time domain equals convolution in frequency domain, the Fourier transform of the product then yields

$$\begin{aligned} Y_{dr,a}(\Omega) &= \int_{-\infty}^{\infty} \tilde{a}(\tau) y_{dr}(\tau - t_s) e^{-j\Omega\tau}\, d\tau \\ &= \tilde{A}(\Omega) * \int_{-\infty}^{\infty} y_{dr}(\tau - t_s) e^{-j\Omega\tau}\, d\tau \\ &= \tilde{A}(\Omega) * \tilde{I}(\Omega) \; * \int_{-\infty}^{\infty} \sum_{i=1}^{N} d_i \tilde{h}_i(\tau) e^{j\Omega_b\tau} e^{-j\Omega\tau}\, d\tau \\ &= \tilde{A}(\Omega) * \tilde{I}(\Omega) \; * \sum_{i=1}^{N} d_i \tilde{H}_i(\Omega) * \int_{-\infty}^{\infty} e^{j(\Omega_b - \Omega)\tau}\, d\tau\,. \end{aligned} \quad (6)$$

The integral term is evaluated over the interval $[0, T]$, yielding a scaled sinc function plus an imaginary term $\zeta(t_i, \Omega)$

$$\int_0^T e^{j(2\pi \frac{B}{T} t_i - \Omega)\tau}\, d\tau = T \frac{\sin\left[\pi(2Bt_i - \frac{\Omega T}{\pi})\right]}{\pi(2Bt_i - \frac{\Omega T}{\pi})} + \zeta(t_i, \Omega) \quad (7)$$

so that

$$Y_{dr,a}(\Omega) = \tilde{A}(\Omega) * \tilde{I}(\Omega) * T \sum_{i=1}^{N} d_i \tilde{H}_i(\Omega) * \left[\operatorname{sinc}\left(2Bt_i - \frac{\Omega T}{\pi}\right) + \zeta(t_i, \Omega)\right]. \quad (8)$$

Since each beat-frequency is related to the travel-time delay, or corresponding target range, the frequency in (8) can be substituted with time through a linear relationship

$$\Omega = 2\pi \frac{B}{T} t\,. \quad (9)$$

This time variable is written as t and termed "fast-time". It has been discriminated from the sweep-time τ that span the frequency sweep during acquisition, as fast-time is on a much shorter time scale similar to the travel-time delays. The frequency variables in sweep-time can therefore be redefined to time variables in fast-time ($\tilde{I}[\Omega(t)] = i(t)$, $\tilde{A}[\Omega(t)] = a(t)$, $\tilde{H}_i[\Omega(t)] = h_i(t)$, and $\zeta[t_i, \Omega(t)] = \zeta(t_i, t)$)

$$Y_{dr,a}[\Omega(t)] = a(t) * i(t) * T \sum_{i=1}^{N} d_i h_i(t) * [\operatorname{sinc}[2B(t - t_i)] + \zeta(t_i, t)] \quad (10)$$

where we take advantage of sinc being an even function.

The signal in (10) is complex, so we define the final processed recording as its real part, $y_p(t) = \Re\{Y_{dr,a}[\Omega(t)]\}$. The expression can be simplified using the Dirac delta function and defining the reflectivity series

$$\begin{aligned} T \sum_{i=1}^{N} d_i h_i(t) * \operatorname{sinc}[2B(t - t_i)] &= T \operatorname{sinc}(2Bt) * \sum_{i=1}^{N} d_i \delta(t - t_i) * h_i(t) \\ &= T \operatorname{sinc}(2Bt) * r(t) \\ &= T\, r(t)\,. \end{aligned} \quad (11)$$

The reflectivity series $r(t)$ is the typical definition for reflections in attenuating and dispersive media, employing the nonstationary convolution model [12]. The sinc function can furthermore be safely ignored as the convolution will not alter the expression, because the waveform's frequency sweep in (1) is contained within $2B$.

The final result is expressed in terms of a convolution model between the amplitude taper, instrument-correction, and reflectivity series in fast-time, or as multiplication of corresponding spectra in frequency domain:

$$\begin{aligned} y_p(t) &= a(t) * i(t) * T\, r(t) \\ Y_p(\omega) &= A(\omega)\, I(\omega)\, T\, R(\omega)\,. \end{aligned} \quad (12)$$

As seen in the equations above, the results are scaled by a factor T, the instrument sweep length. Note also that ω is the fast-time frequency, which is distinguished from the sweep-time frequency Ω in (6)–(9). In Fig. 3, the variables are presented in both sweep-time and fast-time, through the linear relation described in (9). Also presented are a RIMFAX-specific instrument correction and a commonly used amplitude taper.

C. FDTD-Modeling Corrections

In this section, we will review FDTD-simulations and the necessary corrections steps so that one may obtain the same results as a FMCW radar. The raw simulation results $y_{\text{fdtd}}(t)$ can be described as the convolution between the short-duration excitation waveform $w_{\text{fdtd}}(t)$ and the subsurface model's reflectivity series $r(t)$. Additionally, an inevitable direct wave between source and receiver will be included together with a term $\gamma_w(t)$ describing source excitation effects [13]

$$y_{\text{fdtd}}(t) = w_{\text{fdtd}}(t) * [r(t) + d_d \delta(t - t_d)] + \gamma_w(t)\,. \quad (13)$$

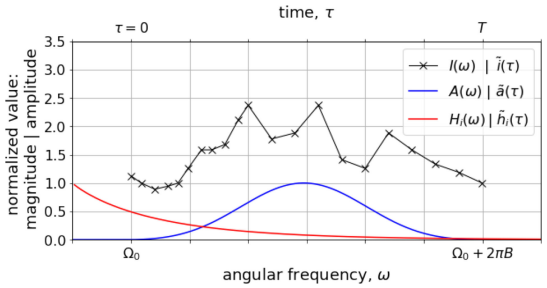

Fig. 3. Instrument correction (black) and amplitude taper (blue) in fast-time frequency domain and sweep-time time domain. Normalized magnitude is used in frequency domain representation and normalized amplitude is used in time domain representation. The instrument correction is assumed to be equal the measurements of RIMFAX' bore-sight gain [5], while the amplitude taper is a commonly used blackman window. Also plotted is an example of an attenuation and dispersion functions (red), accounting for the frequency dependent attenuation for an individual reflection. The function equals that of a constant-Q medium, as described in "Results and Discussion" Section A.

Here, $r(t)$ is the same as in (11), d_d corrects the amplitude of the direct wave for geometrical spreading and t_d is the travel-time of the direct wave.

In Fig. 1(b) a block diagram of the modeling corrections is presented. In order to model a monostatic radar system, the first operation is a background removal, subtracting the simulation over the subsurface model with, e.g., a subtrahend containing the direct wave and source effects

$$y_{\text{fdtd}}(t) - [d_d w_{\text{fdtd}}(t - t_d) + \gamma_w(t)] = w_{\text{fdtd}}(t) * r(t). \quad (14)$$

The background subtrahend could typically be another simulation conducted over an empty model. Depending on the focus of the study, the background removal could alternatively be conducted with a trend extracted from the simulated data similar to standard techniques in field data processing.

When studying air-coupled radars with a focus on weak subsurface reflections, it can be beneficial to include the surface reflection in the subtrahend. First, it is an efficient way of eliminating artificial "ringing" between the surface reflection and insufficiently damped reflections from the bounding sides of the FDTD-model. Second, if the radar system's waveform have dominant sidelobes, they could drown out weaker reflections, which is especially relevant for subsurface reflections in attenuating media.

By using the waveform to deconvolve the remainder in (14), the transmitted waveform is effectively removed from the signal. This operation is achieved through multiplication in frequency domain with the inverse of the waveform spectrum,

$$W^{-1}_{\text{fdtd}}(\omega) W_{\text{fdtd}}(\omega) R(\omega) = R(\omega) \quad (15)$$

where

$$W^{-1}_{\text{fdtd}}(\omega) = W^{*}_{\text{fdtd}}(\omega) / |W_{\text{fdtd}}(\omega)|^2 . \quad (16)$$

The frequency ω is equivalent to the fast-time frequency in stretch processing.

The next step is multiplication with an instrument correction $I(\omega)$ and amplitude taper $A(\omega)$. In time domain, the result is the same as in (12), but with an unscaled reflectivity series

$$y_p(t) = a(t) * i(t) * r(t) . \quad (17)$$

Since this result, equal the output form a FMCW receiver, we have demonstrated that it is possible to conduct FDTD-simulations with a short-duration waveform and obtain the same response as that of a FMCW radar with long sweep time.

D. Modeling Example

To illustrate how the correction steps modify a FDTD-simulation, in Fig. 4 modeling over a no-loss planar, multilayered model is compared to the equivalent FMCW response. The simple geometry in (a) allows for calculating a 1D-reflectivity series and the FMCW response according to (12), as presented in (b). The amplitude taper $A(\omega)$ and instrument correction $I(\omega)$ are as in Fig. 3.

Some considerations are needed in order to model acquisition similar to that of RIMFAX, which has a monostatic air-coupled antenna elevated 0.6 m off the surface. The source–receiver offset in (a) is necessary for the receiver cell to be uninfluenced by the source [7], so these are offset by 0.4 m from one another and located inside the uppermost layer (with permittivity equal that of air, $\epsilon' = 1$). The source and receiver are also elevated 0.57 m above the second layer ($\epsilon' = 4.1$), calculated from the straight ray-path to the central midpoint on that surface ($0.57 = \sqrt{0.6^2 - (0.4/2)^2}$). The waveform in Fig. 4(c) is a Gaussian-modulated sine-wave with centre frequency (675 MHz) and bandwidth (1050 MHz), chosen to have a short-duration that keep computation times low while its frequency spectra encompasses the bandwidth of RIMFAX. Source excitation is done with a Hertzian dipole polarized in the x-direction.

In (d) are the uncorrected FDTD-simulations, source artifacts, the results after background removal, and the final corrected modeling results. FDTD-simulations are conducted with the open-source software gprMax [8] within requirements for a stable simulation, with spatial discretization of 0.01 m and a time increment equal 1.92583e-11 s. Not shown in the model in (a) are the 15 cells thick "perfectly matched layers" at all sides of the model, limiting reflections at the model boundaries.

In the uncorrected FDTD-simulations in (d), the reflection from the second layer is partially obscured by the direct wave, but through background removal it can be recovered. The background subtrahend in this example is the results from simulations conducted over an empty model. By comparing the FMCW response in (b) and the modeling results in (d), it can be seen that modeling corrections give the same results as would be obtained by a FMCW radar, despite there are some minor differences between the 1-D and 3-D reflectivity series. The 3-D model used in FDTD-simulations will also include multiples from within the layers, as well as potential ringing from inadequately damped model boundary reflections.

III. Results and Discussion

The results and discussion is divided into three sections. Section A presents the theory of propagation in attenuating and dispersive media, and its implementation in FDTD-simulations.

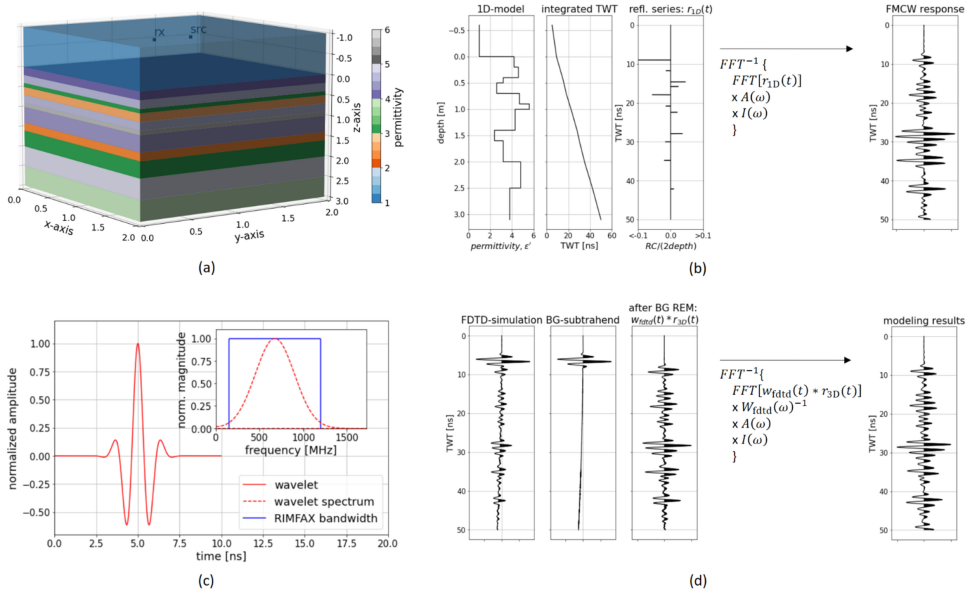

Fig. 4. FDTD-modeling corrections for a no-loss planar, multi-layer model, and the equivalent FMCW response. (a) 3D permittivity model. Not shown in figure are the absorbing boundary conditions applied at all faces of the model space to constrain artificial reflections. (b) 1D-equivalent permittivity model, integrated two-way travel-time (TWT), reflectivity series and analytical FMCW response. The integrated travel-time is calculated according to the permittivity with depth (TWT $= 2$ depth $\sqrt{\varepsilon'}/c$, with c being the speed of light). The corresponding reflectivity series $r(t)$ is equal the reflection constant (RC) at each change in permittivity, multiplied with an amplitude correction of $1/(2 \text{ depth})$ according to geometrical spreading and reflections at planar interfaces. Scaling of the reflectivity series as in (11) is ignored. The FMCW response is obtained from multiplication in frequency domain according to (12). For display purposes, the wiggle-trace has been multiplied with t^2 as a gain function. (c) Gaussian-modulated sine-wave used to excite FDTD-simulations. Next to the waveform's spectrum, RIMFAX' bandwidth is also included for reference. (d) Uncorrected FDTD-simulations, source artifacts (BG-subtrahend), the results after background removal, and the corrected modeling results. Wiggle-traces are displayed with a t^2 gain.

A comparison between modeling results and analytical estimates is presented in Section B, where also the accuracy of the modeling approach is discussed. In Section C, a RIMFAX field test radargram is compared with forward modeling along the same acquisition line. Here, we assess how well modeling reproduce the field recordings, as well as how forward modeling can verify subsurface properties, demonstrating potential use in radargram analysis.

A. Modeling in Attenuating and Dispersive Media

To assess how the presented method holds for modeling the GPR response over a subsurface with realistic properties, we study propagation in an attenuating and dispersive media. This is likely also a representative description for Martian rocks and regolith, where dielectric models have been presented based on measurement of electric and magnetic properties in analog lithologies [14], [15]. We will focus on a constant-Q medium, originally used to describe the cumulative attenuating effects for seismic waves [16], but which has also been found applicable for describing microwave propagation in natural soils and rocks over the GPR frequency range (0.1–1.0 GHz) [8], [9].

Bano [10] demonstrated that the "universal" power-law [17], which approximates media permittivities above the relaxation frequency, corresponds to a constant-Q model

$$\frac{\Im}{\Re}\{\varepsilon(\omega) - \varepsilon_\infty\} = \frac{\varepsilon''(\omega)}{\varepsilon'(\omega) - \varepsilon_\infty} \approx \frac{1}{Q} \tag{18}$$

for the permittivity expressed as

$$\varepsilon(\omega) = \varepsilon'(\omega) + j\varepsilon''(\omega) = \varepsilon_{ref}\left(-j\frac{\omega}{\omega_{ref}}\right)^{n-1} + \varepsilon_\infty. \tag{19}$$

$\varepsilon'(\omega)$ and $\varepsilon''(\omega)$ are the real and imaginary components of the complex permittivity function, respectively. These are frequency dependent quantities in a constant-Q model, while for nonattenuating media the real part is often considered to be constant. The parameter n takes a value between 0 and 1, ε_∞ is the high-frequency permittivity, ω_{ref} is a reference angular frequency and ε_{ref} is a corresponding reference permittivity. The relationship between n and Q is

$$n = \frac{2}{\pi}\tan^{-1}(Q). \tag{20}$$

With respect to the analytical response of a FMCW radar, the attenuating and dispersive transfer function takes the following form in frequency domain:

$$H_i(\omega) = e^{k(\omega)t_i v_i}. \tag{21}$$

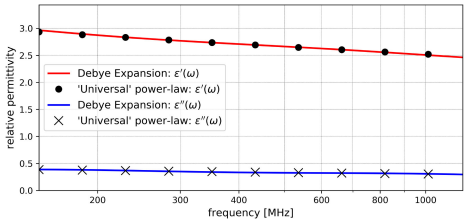

Fig. 5. Two-pole Debye function fit to a "universal" power-law dielectric model. In red and blue are the fitted real and imaginary parts of the permittivity, while circles and crosses are the corresponding data points of the dielectric model according to "overburden" in Fig. 6.

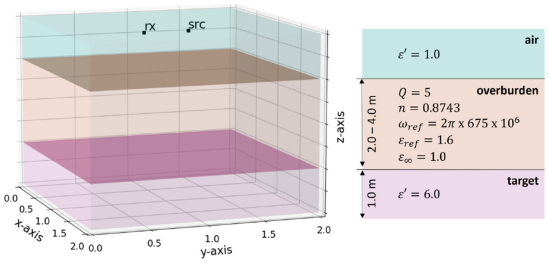

Fig. 6. Model and parameters used in simulation. Source (src) and receiver (rx) are inside of the of the upper air layer, separated by 0.4 m in y-direction and elevated 0.57 m from layer underneath. Overburden is an attenuating and dispersive constant-Q medium with $Q = 5$ and 2.0–4.0 m thickness. Half space target layer is a no-loss medium with permittivity $\varepsilon' = 6.0$ and thickness 1.0 m. Not shown in figure are the absorbing boundary conditions applied at all faces of the model space to constrain artificial reflections.

The sign of the exponent is determined by the complex permittivity convention used in (19), and the exponent is defined in terms of each reflection's two-way traveltime delay t_i, the corresponding average propagation velocities v_i, and the complex wavenumber

$$k(\omega) = j\frac{\omega}{c}\sqrt{\varepsilon(\omega)} \tag{22}$$

where c is the speed of light in vacuum.

For FDTD-simulations, permittivities following the "universal" power-law can be implemented through a multiple pole Debye formulation [18]. Fig. 5 displays the two-pole Debye approximation to a constant-Q dielectric medium.

Modeling results and analytic estimates are compared in a simple scenario with a constant-Q medium overburden and a half-space target layer below, Fig. 6. Dielectric media parameters are also listed in the figure. To assess changes in the reflected signals and their target responses, caused by increasing propagation distance in the attenuating overburden, depth to the target is increased from 2.0 to 4.0 m and reflections at different depths are analyzed individually. The half-space target is itself a 1.0 m deep layer, but only reflections from the interface between the media are fully recorded as perfectly matched layer boundaries restrain reflections from the sides of the model. 3-D FDTD-simulations are conducted as in the Method Section D, with lateral dimensions of the model equal 2.0 m × 2.0 m.

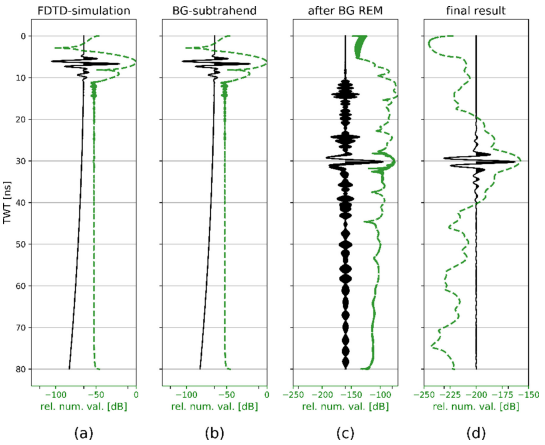

Fig. 7. Modeling corrections applied to FDTD-simulations over target depth at 2.0 m. Traces in black are displayed with a t^2 gain. In green are corresponding envelopes, being equal the magnitude of a complex signal where the real part is the trace and the imaginary part is calculated using the Hilbert transform. The envelope is plotted in dB according to the relative numeric value (rel. num. val.), referenced to the largest computed value. In (a) is the raw result from FDTD-simulations. The background subtrahend is plotted in (b), equal a simulation over a model without target layer. The recording include both the direct wave and surface reflection, as well as source effects and ringing from model boundary reflections. In (c) is the result after background removal, where high frequency noise is dominant. In (d) is the final result after frequency domain operations.

As an example of the correction steps employed, we take a look at the 2.0 m target depth simulation, Fig. 7(a). The background removal subtrahend in (b) includes the direct wave and the first reflection from the air–surface boundary. Choosing this background model was seen to be an efficient way of isolating the low amplitude target reflection, both from source effects and "ringing" caused by inadequately damped reflections at the model boundaries. The relatively strong surface reflections will also get strong sidelobes after incorporation of the instrument correction, which could drown out any low amplitude signal. As seen in (c), high frequency noise has been introduced after the subtraction due to comparably low numerical values in the target reflection. The noise is later removed when applying the amplitude taper that acts like a band-pass filter over the radar bandwidth. The instrument correction and amplitude taper are as in Fig. 3, and corrected modeling result is presented in (d).

B. *Accuracy of Modeling in Attenuating and Dispersive Media*

For each reflection in Fig. 8(a), the target response is seen to be fairly constant, primarily defined by the instrument correction and amplitude taper. There are, however, several characteristic and detectable features caused by attenuation of higher frequency components in a constant-Q medium. The envelopes in (b) show slight broadening with increasing propagation distance, as seen for three selected target depths (2.0 m, 3.0 m, and 4.0 m). Mainlobe widths and sidelobe strengths are similar for modeling and analytical estimates with a relative error below 12%. Associated centre frequency shifts are presented in (c),

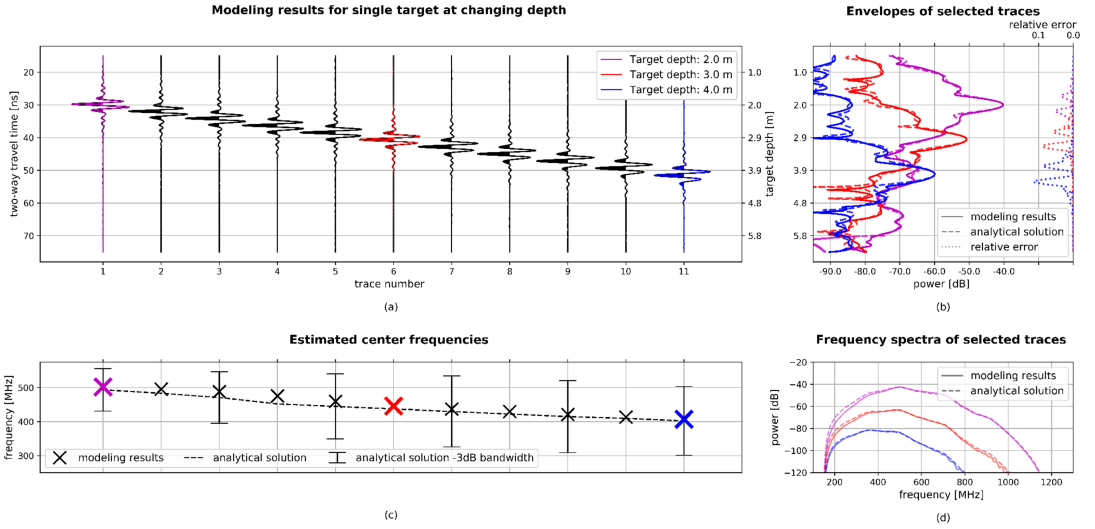

Fig. 8. (a) Results from corrected FDTD-simulations for reflector depths between 2.0 and 4.0 m. Selected traces in color corresponds to target depths at 2.0 m (magenta), 3.0 m (red), and 4.0 m (blue). All traces have normalized amplitudes. (b) Envelopes of selected traces, comparing modeling results with analytical solutions. As in Fig. 7, envelopes are calculated using the Hilbert transform. On the right side are corresponding relative errors with respect to the analytical solution's peak amplitude. (c) Estimates of center frequencies, calculated from the mean value at −3 dB below the spectrum peak. Also shown are the −3 dB bandwidth of the analytical spectra. (d) Comparison of frequency spectra for selected traces.

where modeling and analytical estimates show similar trends. A small mismatch is observed, partly due to a simple definition of the the centre frequency as the mean value at −3 dB below the spectrum peak. Looking at entire frequency spectra in (d), an overall good match is observed.

The observed differences could be caused by inaccurate FDTD-simulations, artifacts from subsequent corrections, or a combination. By looking at the relative error in (b), an inverse proportionality is observed with the amplitude of the reflected waveform, possibly indicating inaccurate representation of very small numerical values. This could for example occur during the background removal, when high frequency noise is introduced, or during the deconvolution operation. Alternatively, the FDTD-model introduce small errors that increase with propagation distance.

The geometry in this simple numerical experiment should not introduce any noticeable errors. Likewise, discrete Fourier transforms and spectral edits are likely not the source of the errors, since both the analytical solution and the modeling corrections are subjected to the same operations. The FDTD-scheme is also solved within requirements of a stable solution [7], ensuring that results are valid with numerical dispersion contained at a minimum. Therefore, inaccuracies deriving from FDTD-computations conducted with double precision should be smaller than the observed differences. Furthermore, approximating the dielectric model through multiple pole Debye formulations have also shown to give accurate results in FDTD simulations [18].

The method presented in this study describes modeling with a short-duration broadband waveform, but how to choose the optimal waveform to excite FDTD-simulations and for conducting subsequent deconvolution, is not within the scope. In fact, excitation could be carried out with a single time increment impulse to yield the reflectivity series directly and omitting the need for deconvolution [13], but then appropriate care would be required to filter out high frequency components not adhering to the FDTD-discretization requirement. This could be handled when applying the amplitude taper during the correction steps, though it might be preferable to excite simulations with a waveform for better control of the FDTD output before applying corrections. Regardless, the observed errors in Fig. 8 are minor, but an optimal waveform could perhaps reduce FDTD source artefacts that can not be fully corrected for by the background removal, as well as restrain potential inaccuracies deriving from the following deconvolution operation.

C. *RIMFAX Field Test Measurements*

To assess how well modeling replicate actual RIMFAX soundings, we look at a radargram acquired during an instrument field test survey. The comparison is also an example of how forward modeling can be used to analyze and verify subsurface properties. Field measurements were conducted with an uncalibrated RIMFAX engineering model, so the analysis will be focused on spectral characteristics in the data since power estimates would not be accurately retrieved.

Fig. 9(a) contains the map view over a selected survey line from Coral Pink state park in Utah, US. The park contains eolian deposited, migrating sand dunes [19], and we look at radar soundings acquired along a 20 m long decent from a ∼4 m tall

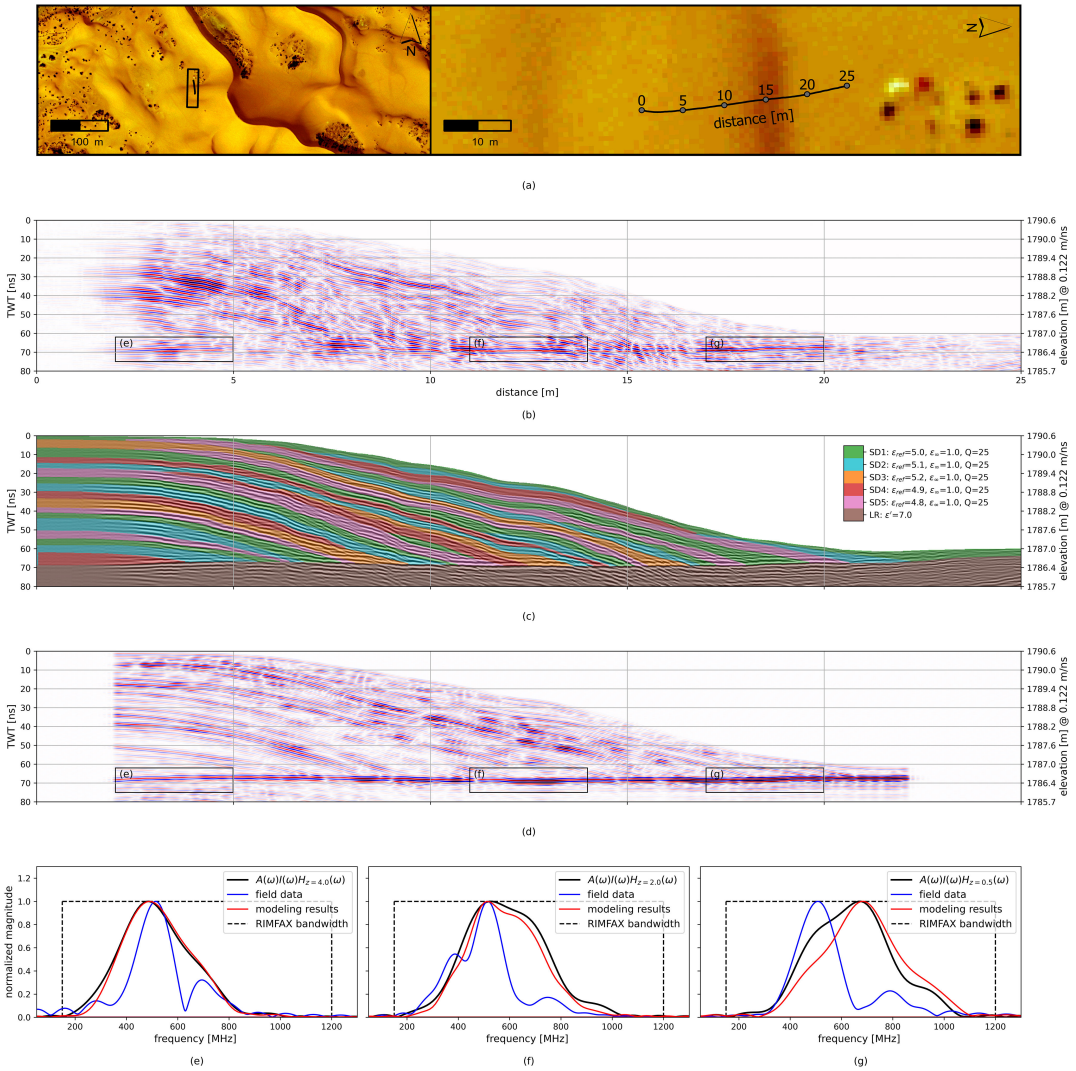

Fig. 9. (a) Selected traverse from the 2018 Coral Pink RIMFAX field test survey, plotted on top of areal imagery acquired the same year by the National Agriculture Imagery Program [22]. To the left is an overview of the nearby sand dunes and the location of the traverse. To the right is the traverse seen descending down from a single sand dune, which can be identified by elongated E-W striking shadows in the areal imagery. (b) Topography corrected radargram showing clearly the shape of the sand dune, and internal layering show down-lapping onto a semihorizontal LR. (c) Subsurface model used in FDTD-simulations. Dielectric models for sand dune layers (SD1–SD5) and LR are listed to the right. The constant-Q models for SD1–SD5, all use the same reference angular frequency, $\omega_{\text{ref}} = 2\pi \times 675 \times 10^6$. (d) Modeling results from FDTD-simulations and subsequent corrections. (e, f, g) Comparison of the frequency spectra for the field data, modeling results and theoretical estimates. Spectra are calculated within windows as shown in (b) and (d), and correspond to average depths of 4, 2, and 0.5 m, respectively. The RIMFAX bandwidth is also outlined for reference.

sand dune and onto an underlying bedrock. In the radargram in (b), internal layering within the sand dune is seen down-lapping onto a semiplanar lower reflector (LR), interpreted as the continuation of the flat bedrock terrain outcropping to the north of the dune. In what follows, we will show how modeling can be used to reproduce similar target responses as in the recorded field data, which is determined by the dune's internal structure and properties. However, an in-depth analysis of the radargram and description of how soil and subsurface parameters are determined, are not within the scope of this study.

The first steps of processing the radargram was done according to Fig. 1(a), with the amplitude taper from Fig. 3. Thereafter, a background removal subtracted a moving average from each sounding, with the average calculated within a window

length of 5 m. The radar system's gating effects [5] were compensated for by equalizing the received power, and a gain with depth was applied in order to visually enhance weaker reflections. Each sounding were shifted vertically so that the peak of the surface reflection would coincide with time zero, before applying a topography correction aligning each sounding according to the elevation and a constant subsurface velocity of 0.122 m/ns. The velocity was initially chosen so that the strong, lower reflection got more planar with an horizontal orientation.

The FDTD subsurface model presented in Fig. 1(c), uses the field data radargram directly as an outline, where the depth axis is linearly related TWT through the constant subsurface velocity. The LR was mapped by tracing the peak of the signal's envelope along the traverse, and interpolating in between where its presence is less clear. Power estimates are not assessed in this study, nor are reflections within the lower layer, so it was simply assigned an arbitrary constant permittivity value, $\varepsilon' = 7$.

Digitizing layering within the sand dune was done by tracing the most prominent reflections, decided to be those with a considerable lateral extent of at least a couple of meters. For simplicity during this assessment, reflections in the processed radargram are assumed to be due to subsurface reflectors, regardless if they in fact could be artificial due to the background removal processing. Furthermore, radargram migration would be required if an exact representation of the reflector dip would be necessary, but not considered significant in this assessment. The mapped reflections were then defined as top interfaces of layers which were assigned a range of dielectric values around a mean velocity of 0.134 m/ns, or $\varepsilon' = 6$, at the center frequency 675 MHz. We define all these layers to have the same constant-Q dielectric model, with $Q = 25$ as an initial guess. Dielectric parameterization is summarized in Fig. 9(c). All media are considered nonmagnetic.

The radargram in Fig. 9(d) was created by running FDTD-simulations over the subsurface model as described for Fig. 8. The 2-D-subsurface model extend in cross-track direction to a 2.5D model, and each sounding was computed every 10 cm along the traverse within a $4.0 \times 1.5 \times 5.5$ m^3 subset [20]. At last, corrections were applied according to Fig. 1(b).

Qualitatively, the modeled radargram contain most of the prominent features from the field data, like the sand dune's internal layering down-lapping onto a lower, planar reflection. The field data, however, inevitably contain more details and more incoherent reflections than the simulation over a simplified and orderly stratified FDTD-model. Target responses along the lower planar reflection seem nevertheless to be fairly similar the two cases.

To assess how well modeling replicate field measurements, in Fig. 9(e)–(g), spectra are compared at depths of $\sim$4, $\sim$2, and $\sim$0.5 m. This is also an example of how to use a boundary reflector to evaluate overburden properties. A edge tapered cosine window (tukey window) is multiplied with targeted data ranges in time-domain, outlined in (b) and (d), before transforming into frequency-domain. Analytical estimates are added for reference, equal the product of the instrument correction, amplitude taper, the transfer function in (21), and similar window taper effects.

The spectra of the modeling results are aligned with analytical estimates, while the field data spectra have a different appearance with, e.g., a prominent dip at around 650 MHz. Still, for the most part, the field data spectra are contained within the others. The apparent mismatch for the $\sim$0.5 m depth in (g), is mostly because the analytic and modeling are normalized to their peak at 650 MHz while the field data are normalized to a peak value of 500 MHz, due to the dip in frequency content. Nevertheless, by looking at the trend in frequency shift with overburden thickness, forward modeling confirm that field measurements are fairly well described by a constant-Q approximation with $Q = 25$.

Using the boresight gain as an approximation to the instrument correction is a simplified approach, as it ideally should also take into account radar electronics that is causing the prominent dip in the field data spectra at around 650 MHz. Interference form the survey vehicle could also be significant and should ideally be incorporated as well. Assessment has been made for integration with the Mars 2020 rover [21], but has not been studied for field test vehicles. When studying RIMFAX data from Mars, however, all effects described by the instrument correction will be attempted corrected for during data processing, meaning that only the amplitude taper will be necessary during FDTD-modeling corrections. This would in fact be preferable for GPR imaging and analysis, as instrument effects will only increase sidelobes of waveforms and reduce the vertical resolution in the radargram.

IV. Conclusion

We have demonstrated that it is possible to conduct FDTD-simulations with a short-duration waveform and model the same target response as would be acquired by a FMCW radar with a stretch processing receiver. Special considerations necessary for modeling weak reflections in realistic, attenuating, and dispersive media have been carefully reviewed. Comparison with field test measurements has assessed the accuracy of the modeling approach and demonstrated the practical use. Forward modeling could therefore be useful for future in-detail analysis of data acquired with RIMFAX, appraising how subsurface structures are imaged with the radar system's resolution and how frequency-dependent attenuation modifies received signals. For example, measurements of the Martian subsurface could be compared with forward modeling over hypothetical subsurface models, and analyzed in a similar way as have been done in lunar exploration. Studying the combined effects of dielectric and volume-scattering losses is furthermore an interesting application, and attempting to decouple these into their individual contributions may in turn be helpful when searching for subsurface water content. Perhaps will it be possible to detect or infer water content in the subsurface through a particular dielectric relaxation. Moreover, the forward modeling approach presented in this study may also turn out to be valuable for inversion modeling. By having obtained the target response of a specific radar system, forward modeling could be compared directly with soundings acquired over a subsurface with unknown properties, with an iterative optimization of FDTD-model parameters.

ACKNOWLEDGMENT

The authors would like to acknowledge RIMFAX team members responsible for the 2018 Coral Pink field test survey, and especially Tor Berger who made the recordings available for us to present in this publication.

REFERENCES

[1] E. Pettinelli, S. E. Lauro, E. Mattei, B. Cosciotti, and F. Soldovieri, "Stratigraphy versus artefacts in the Chang'e-4 low-frequency radar," *Nature Astron.*, vol. 5, pp. 890–893, 2021.
[2] C. Li *et al.*, "Pitfalls in GPR data interpretation: False reflectors detected in lunar radar cross sections by Chang'e-3," *IEEE Trans. Geosci. Remote Sens.*, vol. 56, no. 3, pp. 1325–1335, Mar. 2018.
[3] J. Lai *et al.*, "First look by the Yutu-2 rover at the deep subsurface structure at the lunar farside," *Nature Commun.*, vol. 11, no. 1, 2020, Art. no. 3426.
[4] L. Zhang *et al.*, "Simulation of the lunar regolith and lunar-penetrating radar data processing," *IEEE J. Sel. Topics Appl. Earth Observ. Remote Sens.*, vol. 11, no. 2, pp. 655–663, Feb. 2018.
[5] S.-E. Hamran *et al.*, "Radar imager for Mars' subsurface experiment-RIMFAX," *Space Sci. Rev.*, vol. 216, no. 8, pp. 1–39, 2020.
[6] D. B. Davidson, *Computational Electromagnetics for RF and Microwave Engineering*. 2nd ed. Cambridge, U.K.: Cambridge Univ. Press, 2010.
[7] C. Warren, A. Giannopoulos, and I. Giannakis, "gprMax: Open source software to simulate electromagnetic wave propagation for ground penetrating radar," *Comput. Phys. Commun.*, vol. 209, pp. 163–170, 2016.
[8] G. Turner and A. F. Siggins, "Constant Q attenuation of subsurface radar pulses," *Geophysics*, vol. 59, no. 8, pp. 1192–1200, 1994.
[9] F. Hollender and S. Tillard, "Modeling ground-penetrating radar wave propagation and reflection with the Jonscher parameterization," *Geophysics*, vol. 63, no. 6, pp. 1933–1942, 1998.
[10] M. Bano, "Constant dielectric losses of ground-penetrating radar waves," *Geophys. J. Int.*, vol. 124, no. 1, pp. 279–288, 1996.
[11] B. Keel, J. Baden, W. Melvin, and J. Scheer, "Advanced pulse compression waveform modulations and techniques," in *Principles of Modern Radar: Advanced Techniques*, Edison, New Jersey: SciTech Publishing, 2012, pp. 19–85.
[12] G. F. Margrave, "Theory of nonstationary linear filtering in the fourier domain with application to time-variant filtering," *Geophysics*, vol. 63, no. 1, pp. 244–259, 1998.
[13] D. T. Murphy, A. Southern, and L. Savioja, "Source excitation strategies for obtaining impulse responses in finite difference time domain room acoustics simulation," *Appl. Acoust.*, vol. 82, pp. 6–14, 2014.
[14] D. Stillman and G. Olhoeft, "Frequency and temperature dependence in electromagnetic properties of martian analog minerals," *J. Geophys. Res., Planets*, vol. 113, no. E9, 2008, doi: 10.1029/2007JE002977.
[15] Y. Brouet, P. Becerra, P. Sabouroux, A. Pommerol, and N. Thomas, "A laboratory-based dielectric model for the radar sounding of the martian subsurface," *Icarus*, vol. 321, pp. 960–973, 2019.
[16] P. G. Richards and K. Aki, *Quantitative Seismology: Theory and Methods*. vol. 859. New York, NY, USA: Freeman, 1980.
[17] A. K. Jonscher, "The 'universal' dielectric response," *Nature*, vol. 267, no. 5613, pp. 673–679, 1977.
[18] I. Giannakis, A. Giannopoulos, and N. Davidson, "Incorporating dispersive electrical properties in FDTD GPR models using a general Cole-Cole dispersion function," in *Proc. IEEE 14th Int. Conf. Ground Penetrating Radar*, 2012, pp. 232–236.
[19] R. Ford, S. Gillman, D. Wilkins, W. Clement, and K. Nicoll, "Geology and geomorphology of coral pink sand dunes state park," *Utah Geological Assoc. Pub.*, vol. 28, pp. 379–406, 2010.
[20] S. Eide, S.-E. Hamran, H. Dypvik, and H. E. F. Amundsen, "Ground-penetrating radar modeling across the Jezero crater floor," *IEEE J. Sel. Topics Appl. Earth Observ. Remote Sens.*, vol. 14, pp. 2484–2493, 2021.
[21] E. Gonzales, E. Cordoba, and S.-E. Hamran, "Compatibility tests between the mars vehicle system test bed and RIMFAX radar antenna prototype for the Mars 2020 mission," in *Proc. IEEE Int. Symp. Electromagn. Compat. Signal/Power Integrity*, 2017, pp. 44–50.
[22] USDA-FPAC-BC-APFO Aerial Photography Field Office, "NAIP digital georectified image geospatial_data_presentation_form: Remote-sensing image," *Entity ID: M_3711259_SW_12_060_20180807*, 2019. Accessed: Nov. 15, 2021. [Online]. Available: https://earthexplorer.usgs.gov

Sigurd Eide received the M.Sc. degree in geophysics from the University of Oslo, Oslo, Norway, in 2014. He is currently working toward the Ph.D. degree in geophysics with the Department of Technology Systems, University of Oslo.

From 2014 to 2018, he was a Consultant within marine geophysics and geographical information systems. Since 2018 and the start of his Ph.D. work, he has been engaged with the RIMFAX instrument on the NASA Mars 2020 Perseverance Rover Mission, where he has been developing methods of data analysis and taking part in tactical payload operation. His research interests includes remote sensing and numerical modeling applied to geological exploration, in particular ground penetrating radar and active-source seismic.

Titus Casademont received the M.Sc. degree in geophysics from the University of Hamburg, Hamburg, Germany, in 2020. He is currently working toward the Ph.D. degree in geophysics with the Center for Space Sensors and Systems, University of Oslo, Oslo, Norway.

As a member of the Mars 2020 RIMFAX team, he studies dielectric permittivity and density inversion of the Martian subsurface, both with conventional and machine learning approaches. His research interests are centered around radar remote sensing for earth and planetary geoscience with a focus on *in situ* UWB radar.

Øyvind Lund Aardal received the M.Sc. degree in applied mathematics from the University of Oslo, Oslo, Norway, in 2008, and the Ph.D. degree in medical radar from the University of Oslo, in 2013.

Since 2020, he has been an Adjunct Associate Professor with the Department of Technology Systems, University of Oslo, where he teaches a course in radar remote sensing. Since 2009, he has been a Scientist with the Norwegian Defence Research Establishment (FFI), Norway. His research interests include radar signal processing, medical radar, and sensor data handling and exploitation.

Svein-Erik Hamran received the M.Sc. degree in physics from the Norwegian University of Science and Technology, Trondheim, Norway, in 1984, and the Ph.D. degree in physics from the University of Tromsø, Tromsø, Norway, in 1990.

He is currently a Professor with the Department of Technology Systems, University of Oslo. He is also the Principal Investigator of the Radar Imager for Mars subsurface eXperiment RIMFAX on the NASA Mars 2020 Perseverance Rover Mission and a Co-Principal Investigator on the WISDOM GPR experiment on the ESA ExoMars rover. His research interests include UWB radar design, radar imaging, and modeling in medical and ground-penetrating radar.

Paper III

Radar Attenuation in the Shallow Martian Subsurface: RIMFAX Time-Frequency Analysis and Constant-Q Characterization over Jezero Crater Floor

Sigurd Eide, Titus M. Casademont, Tor Berger, Henning Dypvik, Emileigh S. Shoemaker, and Svein-Erik Hamran

Published in *Geophysical Research Letters*, 2022, volume 50, pp. e2022GL101429. DOI: 10.1029/2022GL101429.

III

Geophysical Research Letters

RESEARCH LETTER
10.1029/2022GL101429

Special Section:
The Mars Perseverance Rover Jezero Crater Floor Campaign

Radar Attenuation in the Shallow Martian Subsurface: RIMFAX Time-Frequency Analysis and Constant-Q Characterization Over Jezero Crater Floor

Sigurd Eide[1], Titus M. Casademont[1], Tor Berger[1,2], Henning Dypvik[1], Emileigh S. Shoemaker[3], and Svein-Erik Hamran[1]

[1]Centre for Space Sensors and Systems (CENSSS), University of Oslo, Kjeller, Norway, [2]Norwegian Defence Research Establishment (FFI), Kjeller, Norway, [3]Lunar and Planetary Laboratory, University of Arizona, Tucson, AZ, USA

Abstract Attenuation of radar waves in the subsurface can be quantified with a constant-Q approximation through time-frequency analysis. We implement the centroid frequency-shift method and study Radar Imager for Mars' Subsurface Exploration (RIMFAX) data acquired along the Mars 2020 Perseverance rover traverse. Attenuation is among key media properties, but quantified estimates need to account for instrument characteristics and limitations in the analysis technique. We ensure accurate constant-Q characterization and present the first estimates of radar attenuation in the upper 5 m of the shallow Martian subsurface. Over Jezero Crater Floor, constant-Q is on average 70.4 ± 7.7, which equals an attenuation of -2.6 ± 0.3 dB/m at RIMFAX' 675 MHz center frequency. Regions comprising the Máaz or Séítah formations have similar attenuation properties that are consistent with magmatic lithologies.

Plain Language Summary First estimates of radar attenuation in the shallow Martian subsurface are presented. Estimates are from Jezero Crater Floor, along the drive path of the Mars 2020 Perseverance rover. Attenuation is among key media properties that describe radar wave propagation and can relate to lithological properties. Estimates of signal losses are consistent with magmatic lithologies and differences between distinct regions on Jezero Crater Floor are not detected.

Key Points:

- First estimates of radar attenuation in the shallow Martian subsurface are on average −2.6 dB/m at the Radar Imager for Mars' Subsurface Exploration (RIMFAX) 675 MHz center frequency
- Results are consistent with magmatic lithologies on the Jezero Crater Floor
- The centroid frequency-shift method is adequately implemented for RIMFAX analysis

Correspondence to:
S. Eide,
sigurd.eide@its.uio.no

Citation:
Eide, S., Casademont, T. M., Berger, T., Dypvik, H., Shoemaker, E. S., & Hamran, S.-E. (2023). Radar attenuation in the shallow Martian subsurface: RIMFAX time-frequency analysis and constant-Q characterization over Jezero Crater Floor. *Geophysical Research Letters*, *50*, e2022GL101429. https://doi.org/10.1029/2022GL101429

Received 5 OCT 2022
Accepted 7 DEC 2022

Author Contributions:
Conceptualization: Sigurd Eide, Titus M. Casademont, Tor Berger, Henning Dypvik, Svein-Erik Hamran
Data curation: Sigurd Eide
Formal analysis: Sigurd Eide
Funding acquisition: Svein-Erik Hamran
Investigation: Sigurd Eide
Methodology: Sigurd Eide, Svein-Erik Hamran
Project Administration: Svein-Erik Hamran
Resources: Sigurd Eide
Software: Sigurd Eide

© 2022. The Authors.
This is an open access article under the terms of the Creative Commons Attribution License, which permits use, distribution and reproduction in any medium, provided the original work is properly cited.

1. Introduction

During the first 379 sols of NASA's Perseverance rover mission on Mars, over 5 km had been driven over the Jezero Crater Floor. The rover had gone from the Octavia E. Butler landing site (OEB), located on the relatively flat terrain of the Máaz Formation, to the distinct rugged exposures of the Séítah Formation. Afterward, the rover drove back again to OEB, largely backtracking its original route. The Radar Imager for Mars' Subsurface Exploration (RIMFAX; Hamran et al., 2020) conducted measurements along the whole traverse, providing an exceptional data set for constraining subsurface parameters over a large geographical area spanning several different regions (Figure 1). Moreover, the close vicinity of the two passes allows for testing replicability of obtained media parameters.

The first look into the shallow Martian subsurface disclosed intriguing reflector geometries, which at places can be correlated with outcropping rock formations on the surface (Hamran et al., 2022). Yet, more information is contained in the acquired data, hidden by randomly distributed reflections dominating the radar image. This calls for supplementary analysis of the radar data beyond that of visual inspection.

Ground-penetrating radar (GPR) data is strongly affected by the frequency dependent attenuation mechanisms. In general, higher frequency content is attenuated more than lower, so that subsurface reflection spectra will be altered compared to that of the transmitted waveform. The constant-Q factor was originally used to describe similar behavior of seismic waves due to cumulative attenuating effects in the ground (Richards & Aki, 1980), but it has also been found applicable for electromagnetic propagation in natural soil and rocks over the GPR frequency range 0.1–1.0 GHz (Harbi & McMechan, 2012; Turner & Siggins, 1994). For this reason, it can be appropriate to assume a linear frequency dependence for the attenuation in GPR sounding:

$$E(\omega, t_{wt}) = E_0(\omega) \times \exp\left(-\frac{\omega t_{wt}}{2Q^*}\right). \quad (1)$$

Supervision: Tor Berger, Henning Dypvik
Validation: Sigurd Eide
Visualization: Sigurd Eide, Svein-Erik Hamran
Writing – original draft: Sigurd Eide
Writing – review & editing: Sigurd Eide, Titus M. Casademont, Henning Dypvik, Emileigh S. Shoemaker

The frequency spectrum of the electric field intensity $E(\omega, t_{twt})$ is a function of angular frequency ω and propagation time t_{twt}. $E_0(\omega)$ is the spectrum of the transmitted waveform. Turner and Siggins (1994) noted that the GPR parameter Q* is effectively a generalized version of the corresponding seismic parameter Q, but differs as radar attenuation extrapolates to a finite value at zero frequency. However, this difference bears little practical significance in radargram analysis of low conductivity media like the dry Martian regolith. From evaluating the exponential term in Equation 1, the attenuation constant α can be written in terms of Q* and the propagation velocity v:

$$\alpha = \frac{\omega}{2Q^* v}\ [Np/m] = 8.69 \times \frac{\omega}{2Q^* v}\ [dB/m]. \tag{2}$$

In many radar studies, the relationship between the imaginary and real part of a dielectric model is commonly described by the loss tangent ($\tan\delta$). For non-dispersive media and in the absence of scattering losses, it will effectively be the inverse Q*-factor. In fact, the "universal" power-law that approximates media permittivity above the relaxation frequency (Jonscher, 1977), implies a constant-Q model (Bano, 1996). Bradford (2007) also show how the constant-Q model is useful for describing several dielectric models, like Cole-Cole or Debye, in the case of band-limited GPR signals.

In addition to dielectric attenuation, volume scattering losses are frequency dependent and contribute to the composite signal attenuation, for example, Mie scattering by idealized distribution of spherical inclusions (e.g., Ulaby & Long, 2014) or layer scattering as predicted by localization theory (Van Der Baan, 2001). For GPR field measurements, the constant-Q model has proven useful for describing the bulk attenuation (Bradford, 2007; Ding et al., 2020; Economou & Kritikakis, 2016; Irving & Knight, 2003; Lauro et al., 2022). Moreover, radars in orbit around Mars also assume a constant-Q equivalent model (B. Campbell & Morgan, 2018; B. Campbell et al., 2008). The term "effective loss tangent" is sometimes used for describing bulk attenuation ($\tan\delta_e = 1/Q^*$).

There exist numerous techniques for estimating the Q*-factor (e.g., Tonn, 1991). As relative change in spectral components is independent of the total signal strength at a certain time interval, spectral methods are especially suitable for recordings where true amplitudes are not easily retrieved. In this study, we study both spectra of selected reflections and the integrated time-frequency (T-F) spectra of whole radargram sections. By doing so, we omit having to correct for numerous RIMFAX acquisition parameters in order to adjust and calibrate amplitudes. For a monostatic radar such as RIMFAX, reflection amplitudes along a natural subsurface target will furthermore vary greatly with the viewing angle and variation in media properties, which makes amplitude analysis challenging.

The centroid-frequency shift (CFS) method (Quan & Harris, 1997) is employed to obtain constant-Q estimates in RIMFAX data. We investigate if we can obtain reliable Q*-factor estimates and if it is possible to detect any significant variation over Jezero Crater Floor. The CFS technique's accuracy is one aspect that previously has not been evaluated thoroughly. Through a numerical modeling experiment, we ensure an appropriate implementation of the analysis and study the accuracy of the method. Processing steps needed for preparing RIMFAX data for spectral analysis are also addressed. Thereafter, the first estimates of radar attenuation in the upper 5 m of the Martian subsurface are presented.

2. Methods

In this section we first review the centroid frequency-shift (CFS) technique for determining the Q*-parameter. A numerical modeling experiment will then be used to ensure a correct implementation of the CFS technique and to assess the accuracy of the analysis. Finally, a spectral enhancement processing step will be implemented, which is needed for preparing RIMFAX' frequency modulated continuous wave (FMCW) radar data for spectral analysis.

2.1. Spectral Analysis and the Centroid Frequency-Shift Method

Quan and Harris (1997) present the CFS method where the Q*-factor is obtained analytically from the slope $\Delta f_c / \Delta t_{twt}$ in a recording:

$$Q^* = -C\pi \left(\frac{\Delta f_c}{\Delta t_{twt}} \right)^{-1}. \tag{3}$$

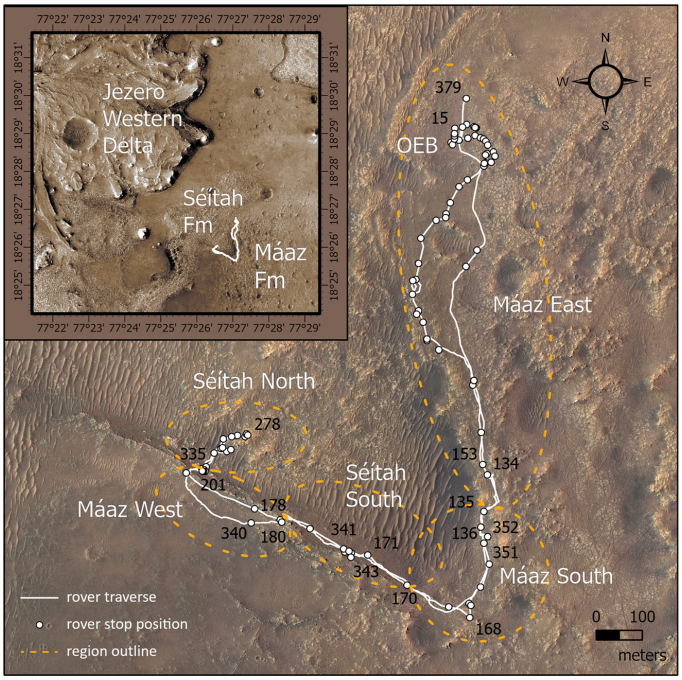

Figure 1. Map view over RIMFAX soundings conducted while driving over the Crater Floor. Inset figure gives the large-scale perspective and show the location of the rover traverse with regards to the Jezero Western Delta. During the first 379 sols, the rover drove from OEB to Séítah, and back. In the map are orange dashed ellipses outlining distinct regions that are investigated separately in this study: (i) Máaz East (sol 15–135 and 353–379); (ii) Máaz South (sol 136–170 and 351–353); (iii) Séítah South (sol 171–178 and 341–351); (iv) Máaz West (sol 180–201 and 340–341); and (v) Séítah North (sol 201–278 and 280–335). Basemaps are Mars 2020 Science Team colored HiRISE mosaics.

The instantaneous center frequency f_c is evaluated over travel time t_{twt}. The constant C depends on the waveform shape and bandwidth, which for a Gaussian waveform equals its variance (in Hz). The amplitude taper employed during FMCW radar processing ideally decides the radar system's impulse response, that is, the waveform equivalent, and enables accurate determination of C and direct use of the equation.

There are several approaches for obtaining the CFS in a single trace or in a section of a radargram. Here we employ the Short-Time Fourier Transform (STFT) to obtain the integrated time-frequency (T-F) spectra of several neighboring traces. For a Gaussian amplitude taper applied during processing over the signal's bandwidth, the instantaneous center frequency will be at the spectra's peak magnitude, for a given travel time. At 1.5 ns time increments in the STFT spectra, the central frequency is identified as the midpoint between −6 dB below the peak spectral value. Then, the slope of the CFS is obtained from a least-square linear regression of central frequencies with travel time.

The CFS can also be obtained from analyzing a coherent reflection in a radargram. A Fourier Transform of a selection with only the target reflection, will ideally give the frequency content of that individual reflection. Doing this on traces where the reflection is located at varying depth, the CFS can be obtained by a linear regression of center frequencies with travel time.

2.2. Evaluation of Analysis Method on Synthetic Data

To assess the CFS technique, we model the radar response over a subsurface model for a range of different Q-values. The subsurface model in Figure 2a is from Eide et al. (2022), consisting of a layered medium overlying

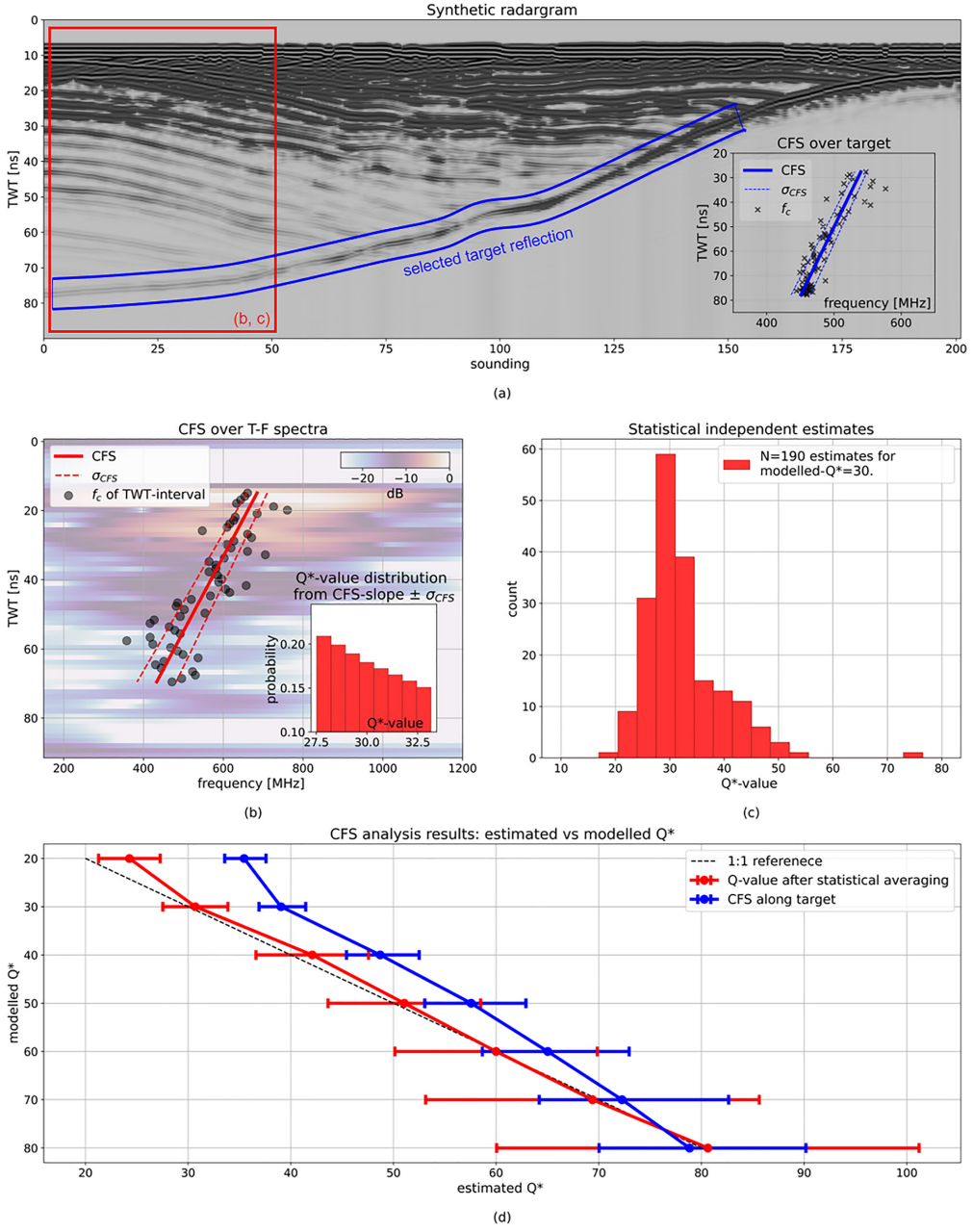
Synthetic radargram
TWT [ns]
sounding
selected target reflection
(b, c)
CFS over target
CFS
σ_{CFS}
f_c
frequency [MHz]
(a)
CFS over T-F spectra
f_c of TWT-interval
dB
Q*-value distribution
from CFS-slope ± σ_{CFS}
probability
Q*-value
frequency [MHz]
(b)
Statistical independent estimates
N=190 estimates for
modelled-Q*=30.
count
Q*-value
(c)
CFS analysis results: estimated vs modelled Q*
1:1 referenece
Q-value after statistical averaging
CFS along target
modelled Q*
estimated Q*
(d)

Figure 2.

a strong target reflection. For each simulation, layers have the same given Q-value and permittivities around a mean of $\varepsilon' = 6$. Soundings are simulated at 0.1 m intervals along a 20 m transect. Numerical simulations are conducted with gprMax (Warren et al., 2016) with the dielectric constant-Q model implemented through a multiple pole Debye formulation (Giannakis & Giannopoulos, 2014). Corrections according to Eide et al. (2022) are applied to the simulation results, in order to replicate a FMCW radar with the same bandwidth and central frequency as RIMFAX. Corrections imitate FMCW radar processing with a Gaussian-shaped amplitude taper.

Analyzing the synthetic radargram in Figure 2a should be a suitable numerical experiment for evaluating the spectral analysis methods for RIMFAX data. Note, during analysis of the synthetic data, the surface reflection is removed as in Eide et al. (2022) for improved imaging of subsurface structures. The target analysis is focused on the reflection within the blue selection, while the integrated T-F spectra analysis focuses on the red selection. Inset figure shows the CFS fit for the target, with the standard deviation of the residuals as an estimate of the uncertainty.

Results from the CFS analysis are highly sensitive to the linear fit to the center frequencies, so a statistical approach was taken for the T-F spectra analysis. Figure 2b displays the regression to the estimated center frequencies of each time interval in the T-F spectra. The inset figure shows the range of Q*-values within one standard deviation of the residuals ($\pm\sigma_{\mathrm{CFS}}$). As the function Q* has an hyperbolic dependence with the slope $\Delta f/\Delta t_{\mathrm{twt}}$, valid (positive) Q* estimates will be drawn from an exponential distribution. That is, small inaccuracies during slope regression will not yield Q* estimates centered around the true Q* value in the data. But an improved estimate can be obtained by averaging statistically independent estimates, which will result in a more centralized distribution. The statistically independent estimates are obtained by conducting CFS fits to multiple selections of neighboring soundings within the analyzed radargram section. With the skewed distribution in (c), the median of all estimated Q*-values is the most likely and the uncertainty is defined in terms of the semi-interquartile range (semi-IQR).

Conducting the same target and T-F spectra analyses for models with Q*-values between 20 and 80, we obtain the results in (d). The accuracy of the target analysis in blue is low for modeled Q*-values of 60 and less, but consistent in that models with lower Q*-factors results in lower Q*-estimates. For analysis of the T-F spectra, a better match with the modeled Q* is obtained. The statistical approach clearly helps constraining the average value. Still, it can be observed that the analysis results have high uncertainties that increase with higher Q*-values.

2.3. Spectral Enhancement of RIMFAX' Deramped Signal

This study analyses RIMFAX' shallow mode recordings acquired across the full bandwidth, 150–1,200 MHz. RIMFAX is a stretch processing receiver that records a deramped signal from the mixer output (see Eide et al., 2022; Hamran et al., 2020). The first processing step is a background removal (BGR) with a single value decomposition filter, applied to remove ringing in the recording. Figures 3a–3d present the raw and filtered deramped signal.

In (e, f) an amplitude taper is applied, for sidelobe reduction in the later Fourier transform and radargram generation. For the CFS analysis, a Gaussian window was selected with a standard deviation equal 20% of the bandwidth (122 sweep time samples). For a Gaussian window centered at the 675 MHz RIMFAX center frequency, that is equivalent to 210 MHz. When conducting spectral analysis, there is a trade-off between a well-represented Gaussian function (small standard deviation) and a wide bandwidth for better constrain on the CFS (large standard deviation). The selected window was seen to work well over RIMFAX' bandwidth.

In some of RIMFAX' sweep time samples, the signal is dominated by artifacts after BGR. Samples between 250 and 300 are influenced by a combination of (a) low synthesized signals in the electronic box over that interval, (b) low antenna gain at the corresponding frequencies, and (c) noticeable strong ringing occurring during that time of the FMCW sweep. This results in a radargram having non-uniform frequency spectrum with certain

Figure 2. CFS analysis on synthetic data modeled with constant-Q dielectric media. (a) Synthetic radargram with selection in red for the integrated T-F analysis and selection in blue for target reflection analysis. Inset figure shows the scatter plot of the target's center frequencies for each sounding, and the CFS linear regression. Error bars are according to the standard deviation of the residuals in the regression (σ_{CFS}). The analysis is illustrated in the case of a model with Q* = 30. (b) CFS linear regression over T-F spectra in the case of Q* = 30. Inset figure show the exponential distribution of values within one standard deviation of the regression residuals ($\pm\sigma_{CFS}$), illustrating the low accuracy of a single CFS regression. (c) A statistical averaging is done to overcome the low accuracy in a single T-F CFS regression, with the median of *N* statistically independent estimates providing a more reliable results. (d) Results form integrated spectra and target analyses for modeled Q*-values in the range 20–80. Error bars for the statistically averaged T-F spectra estimates are according to the semi-IQR.

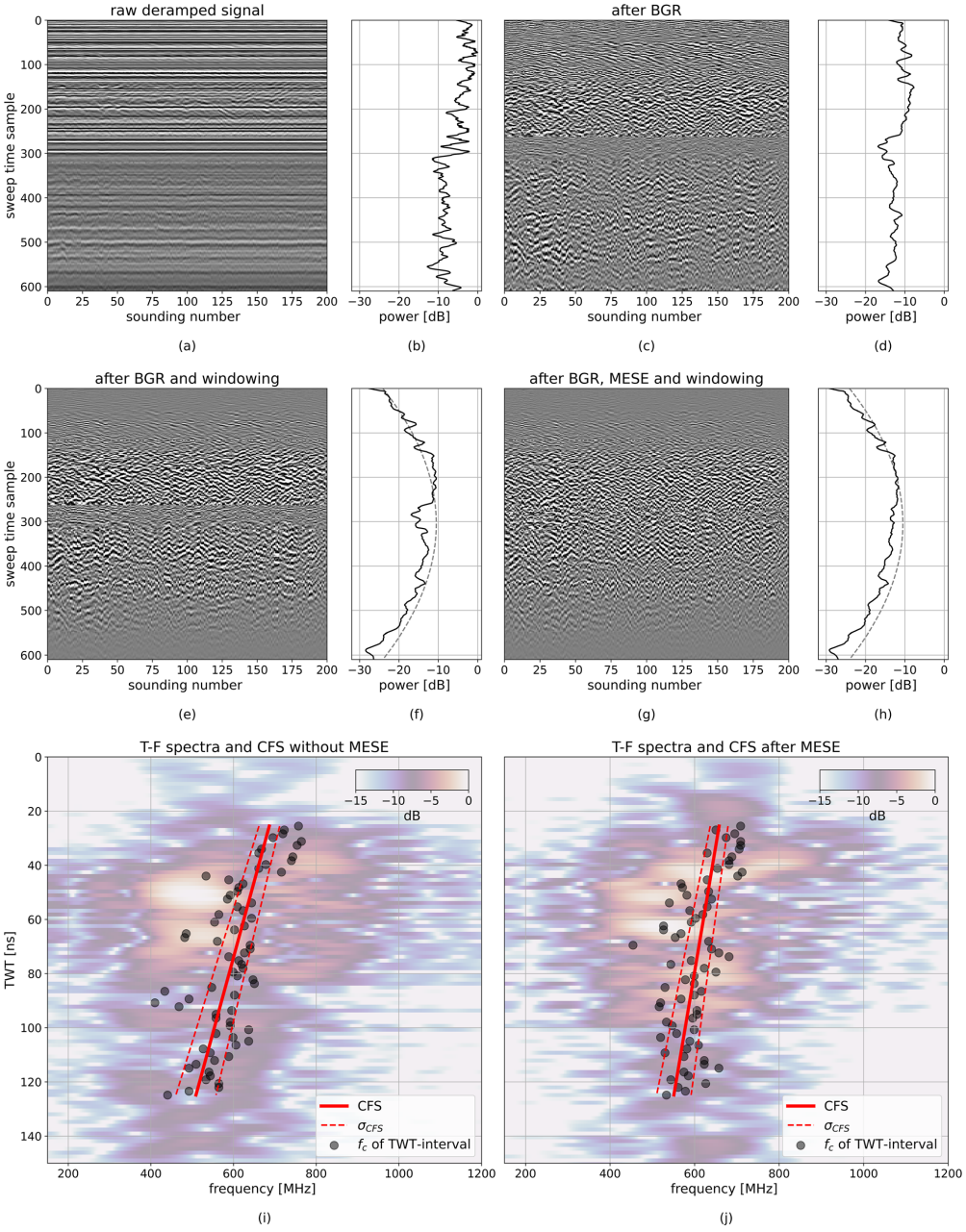
raw deramped signal
after BGR
sweep time sample
sounding number
power [dB]
(a)
(b)
(c)
(d)
after BGR and windowing
after BGR, MESE and windowing
(e)
(f)
(g)
(h)
T-F spectra and CFS without MESE
T-F spectra and CFS after MESE
dB
TWT [ns]
frequency [MHz]
CFS
σ_{CFS}
f_c of TWT-interval
(i)
(j)

Figure 3.

low-magnitude bands dominated by artifacts. For layer detection, this is not crucial as a Fourier transform of the deramped signal will still retrieve targets' time-delays. When studying spectral characteristics of the signal, however, this can deteriorate the analysis.

The deramped signal, in theory, is composed of series of superimposed monochromatic waves, whose frequencies correspond to targets' travel time delays. We therefore make the fundamental assumption that it is possible to mute and interpolate over the samples that cannot properly be retrieved, in order to reconstruct the original signal content. A range of techniques exists for wavefield reconstruction with, for example, recent advances employing convolutional neural network approaches (Larsen Greiner et al., 2020). Still, the autoregressive maximum entropy method (Burg, 1975) remains a viable option for predicting missing parts of a signal based on preceding or proceeding data points. It has, for example, had successful application in bandwidth extrapolation for radar systems (Gambacorta et al., 2022; Oudart et al., 2021). The reconstructed signal over an interval of removed samples, will be a linear combination of the changes above and below in each recorded signal. This is consistent with the linear assumption of a constant-Q model.

Figures 3e–3h compare the windowed deramped signal without and after Maximum Entropy Spectral Enhancement (MESE). The sample range 250–300 in (e), has been improved to a more consistent image in (g). These samples are also seen as a dip in the integrated power spectra in (f), while in (h) a more even power spectra has been retrieved. By applying MESE, the results after windowing will be more aligned with the expected performance of the window function, and hence help improve spectral analysis of RIMFAX data.

A Fourier transform of the deramped signal will yield the radargram, and a STFT of the radargram will generate the T-F spectra. In (i, j) are the T-F spectra without and after MESE. Center frequencies at 1.5 ns time intervals and the CFS regression are also plotted over the spectra. MESE results in a more uniform spectra in (j) with center frequencies more aligned compared to the spectra in (i). The CFS analysis is limited to the time range 25–125 ns, corresponding to the first 100 ns below the surface reflection. Beyond that recording time, RIMFAX shallow mode spectra can be dominated by noise. For the average subsurface radar wave velocity in Jezero Crater of 0.1 m/ns (Casademont et al., 2023), 100 ns corresponds to a depth of 5 m.

3. Results and Discussion

Based on the modeling experiment, we conclude that T-F spectra analysis is more appropriate compared to target analysis. T-F spectra are more suitable for a statistical averaging implementation, which improves accuracy. Its automated implementation is also better suited for processing the large amount of data acquired along the entire rover traverse. Moreover, RIMFAX radargrams are dominated high-amplitude reflection packages instead of single coherent reflections (Hamran et al., 2022), making target picking ambiguous.

Results form T-F CFS analysis every 10 m along the rover traverse are presented in Figure 4. The average for the whole Jezero Crater Floor is in (a) while (b–f) cover the five regions in Figure 1 individually. In (b–f), separate estimates are made for the OEB-Séítah and Séítah-OEB passes. The difference between mean values of two passes within a single region, is comparable to differences between regions. Moreover, all regions have mean values close to the combined estimate in (a), which for all soundings over the Crater Floor is $Q^* = 70.4 \pm 7.7$. At the RIMFAX 675 MHz center frequency, that equates to an attenuation of -2.6 ± 0.3 dB/m assuming a subsurface velocity of 0.1 m/ns (Casademont et al., 2023). Uncertainties are listed in terms of standard deviations. In terms of the effective loss tangent, the average estimate equals $\tan\delta_e = 0.014 \pm 0.002$.

That attenuation is similar over the Jezero Crater Floor, is in line with results from Hamran et al. (2022) where maximum imaging depths are fairly constant. Casademont et al. (2023) analyzed dielectric permittivity in the RIMFAX data and found only small differences between regions. Similar propagation velocities and similar attenuation estimates, could indicate that the shallow subsurface electrical properties are comparable over the whole investigated area. Simultaneously, it may reflect limitations in the analyses' accuracy.

Figure 3. Example of RIMFAX' deramped signal and the effect of MESE. (a) The raw recorded deramped signal for 200 soundings and (b) the corresponding average power spectrum. (c, d) The deramped signal and its power spectrum after BGR. After ringing is removed, the signal level drops to about −10 dB below the raw data recording. Low magnitude sweep time samples appears in the range 250–300. (e, f) The deramped signal after applied amplitude taper, or windowing. (g, h) The windowed deramped signal after applied MESE. The window function is Gaussian with a standard deviation of 20% of the bandwidth, and is shown in (f, h) with a dashed gray line. After MESE in (g), low magnitude samples have been improved, and in (h) the power spectra is more aligned with the window function. (i, j) STFT spectra without and after MESE. Estimated center frequencies f_c align better after MESE and improve the CFS linear regression.

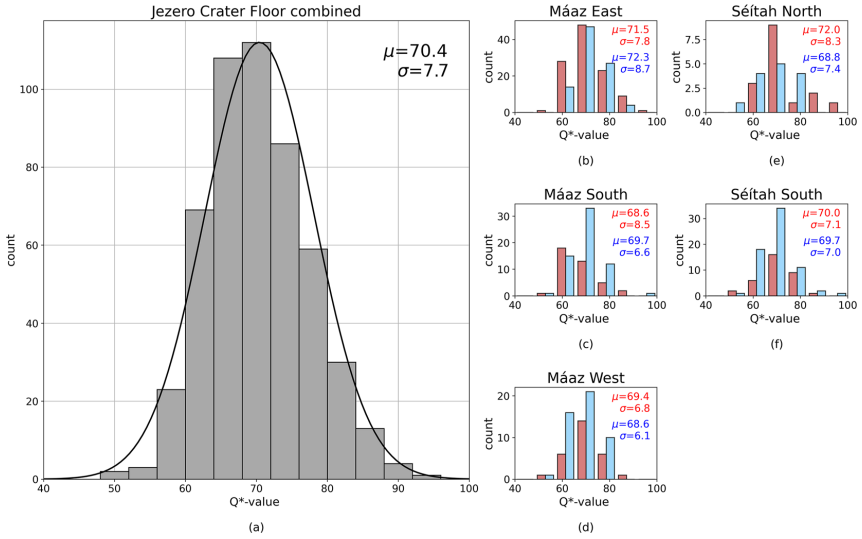

Figure 4. Results form CFS analysis of T-F spectra every 10 m from sol 15 to 379. (a) Histogram of the combined results together with a Gaussian distribution fit. (b–f) The analysis divided into five regions comprising either a part of the Máaz or Séítah formations: (b) Máaz East; (c) Máaz South; (d) Máaz West; (e) Séítah North; and (f) Séítah South. For each separate region, parts of drives extending beyond its boundary are not included in the analysis. Passes are analyzed separately, colored in red for OEB-Séítah and blue for Séítah-OEB. The mean value (μ) and its standard deviation (σ) are listed with each histogram.

Still, Casademont et al. (2023) inferred a small increase in permittivity and density going from the Máaz to Séítah Formation, which was also concluded from observations by the SuperCam instrument of outcrops on the surface (Wiens et al., 2022). The stratigraphic order between Séítah and Máaz was disclosed by RIMFAX imaging (Hamran et al., 2022), but their exact relationship and true emplacement histories are currently under debate (Farley et al., 2022). It is not understood whether (a) Máaz is a separate lithology emplaced on top of Séítah, or (b) if it is an upper differentiated section of the proposed Séítah igneous cumulate. The attenuation analysis, however, cannot detect any variation between the formations or discriminate between the two formation scenarios.

The constant-Q approximation generalizes the composite attenuation of electromagnetic waves and comprises both dielectric and scattering losses. Separating the two is not easily done without additional measurements, though an approach by Harbi and McMechan (2012), for example, attempts this based on theoretical models of the intrinsic losses. Water is in general dominating attenuation in natural terrains on Earth (e.g., Ulaby & Long, 2014). On the Moon, attenuation is usually ascribed to high concentrations of TiO_2 and FeO minerals (e.g., Ding et al., 2020; Olhoeft & Strangway, 1975), often disregarding subsurface volume scattering altogether. It is unknown to what extent volume scattering, mineralogy and any potential water content do affect the attenuation of radar signals in the Martian subsurface. There is furthermore an enrichment of magnetic materials on the surface of Mars (e.g., Madsen et al., 2009) that could impact attenuation in radar sounding, though Stillman and Olhoeft (2008) advocate it would be negligible based on laboratory measurements.

The orbital Martian radar SHARAD did experience a surprising absence of signal returns at places, implying high attenuation over older volcanic lithologies (>1 Ga) and over terrain inferred to have been altered by water. Scattering or bound water in clay-rich lithologies, have been proposed as possible governing loss mechanisms (Stillman & Grimm, 2011). Attenuation estimates by orbital radars, however, are not directly relatable RIMFAX, as scattering losses for wavelengths at which they operate would be caused by inhomogeneities at much larger spatial scales. Furthermore, low-frequency bound-water attenuation would be less at the RIMFAX bandwidth compared to the lower range at which SHARAD operate. But if we assume the obtained constant-Q model from this study can be extrapolated to the SHARAD 20 MHz center frequency, a Q* = 70 equals 0.08 dB/m for a

subsurface velocity of 0.1 m/ns. This estimate is toward the lower bound of the 0.065–0.27 dB/m range obtained in high attenuation regions by Stillman and Grimm (2011), but within range 0.05–0.16 dB/m of other measurements of Martian basalts (Carter et al., 2009; Simon et al., 2014).

Attenuation estimates from this study fall within range of typical values for laboratory measurements of dry magmatic lithologies (M. J. Campbell & Ulrichs, 1969; Ulaby et al., 1990), as RIMFAX permittivity estimates also do (v). Therefore, radar attenuation estimates are consistent with the interpretations by Farley et al. (2022), synthesized from both surface and subsurface observations of Jezero Crater Floor lithologies.

4. Conclusions

The attenuation for RIMFAX soundings over Jezero Crater Floor is estimated to $Q^* = 70.4 \pm 7.7$, or -2.6 ± 0.3 dB/m at the 675 MHz center frequency. Regions comprising the Máaz or Séítah formations have similar attenuation properties that are consistent with magmatic lithologies. Results from this study are non-conclusive with regards to the disputed formation and emplacement histories of the Máaz and Séítah formations.

The centroid frequency-shift (CFS) technique for analyzing radar attenuation is a capable approach that bypass obstacles associated with studying returned signal power. In particular, it is applicable for FMCW radars where the amplitude taper can be appropriately selected for the spectral analysis. The accuracy of the CFS method is assessed through numerical modeling, concluding that single estimates are not reliable and statistical averaging is necessary.

Attenuation estimates from this study could be used as a starting point for more detailed quantitative studies. The results can be valuable as independent and complementary estimates for future studies of returned power in the RIMFAX data. Detailed studies could, for example, focus on smaller-scale detection of radar facies with either high- or low-Q*. If the shallow Martian subsurface contains liquid subsurface brines or significant amounts of bound-water bearing clays, it may be possible to detect a locally increased attenuation and a low-Q*. However, interpretation of attenuation is inherently non-unique with regards to scattering losses verses conductive and dielectric losses. Future work on disentangling the different loss mechanisms will therefore require additional observations or, perhaps, incorporation of appropriate attenuation models based on scientific ingenuity.

Data Availability Statement

The data used in this work are available at the NASA PDS Geosciences Node (https://pds-geosciences.wustl.edu/missions/mars2020/rimfax.htm) (Hamran & Paige, 2021).

Acknowledgments
This work has received funding and support from the Research Council of Norway, Grant 309835 Centre for Space Sensors and Systems (CENSSS), through their SFI Centre for Research-based Innovation program. The authors would also like to acknowledge Letizia Gambacorta at Sapienza University of Rome, for helpful discussions regarding the Maximum Entropy Spectral Enhancement (MESE) technique used in RIMFAX raw data reconstruction.

References

Bano, M. (1996). Constant dielectric losses of ground-penetrating radar waves. *Geophysical Journal International*, *124*(1), 279–288. https://doi.org/10.1111/j.1365-246x.1996.tb06370.x

Bradford, J. H. (2007). Frequency-dependent attenuation analysis of ground-penetrating radar data. *Geophysics*, *72*(3), J7–J16. https://doi.org/10.1190/1.2710183

Burg, J. P. (1975). *Maximum entropy spectral analysis*. Stanford University.

Campbell, B., Carter, L., Phillips, R., Plaut, J., Putzig, N., Safaeinili, A., et al. (2008). Sharad radar sounding of the vastitas borealis formation in amazonis planitia. *Journal of Geophysical Research*, *113*(E12), E12010. https://doi.org/10.1029/2008je003177

Campbell, B., & Morgan, G. A. (2018). Fine-scale layering of Mars polar deposits and signatures of ice content in nonpolar material from multi-band sharad data processing. *Geophysical Research Letters*, *45*(4), 1759–1766. https://doi.org/10.1002/2017gl075844

Campbell, M. J., & Ulrichs, J. (1969). Electrical properties of rocks and their significance for lunar radar observations. *Journal of Geophysical Research*, *74*(25), 5867–5881. https://doi.org/10.1029/jb074i025p05867

Carter, L. M., Campbell, B. A., Holt, J. W., Phillips, R. J., Putzig, N. E., Mattei, S., et al. (2009). Dielectric properties of lava flows west of Ascraeus Mons, Mars. *Geophysical Research Letters*, *36*(23), L23204. https://doi.org/10.1029/2009gl041234

Casademont, T. M., Eide, S., Shoemaker, E. S., Liu, Y., Nunes, D. C., Russell, P., et al. (2023). RIMFAX ground penetrating radar reveals dielectric permittivity and rock density of shallow Martian subsurface. *Journal of Geophysical Research: Planets*, *128*, e2022JE007598. https://doi.org/10.1029/2022JE007598

Ding, C., Xiao, Z., Su, Y., Zhao, J., & Cui, J. (2020). Compositional variations along the route of Chang'e-3 Yutu rover revealed by the lunar penetrating radar. *Progress in Earth and Planetary Science*, *7*(1), 1–11. https://doi.org/10.1186/s40645-020-00340-4

Economou, N., & Kritikakis, G. (2016). Attenuation analysis of real GPR wavelets: The equivalent amplitude spectrum (EAS). *Journal of Applied Geophysics*, *126*, 13–26. https://doi.org/10.1016/j.jappgeo.2016.01.005

Eide, S., Casademont, T., Aardal, Ø. L., & Hamran, S.-E. (2022). Modeling FMCW radar for subsurface analysis. *IEEE Journal of Selected Topics in Applied Earth Observations and Remote Sensing*, *15*, 2998–3007. https://doi.org/10.1109/JSTARS.2022.3165135

Farley, K. A., Stack, K. M., Shuster, D. L., Horgan, B. H. N., Hurowitz, J. A., Tarnas, J. D., et al. (2022). Aqueously altered igneous rocks sampled on the floor of Jezero Crater, Mars. *Science*, *0*(0), eabo2196. https://doi.org/10.1126/science.abo2196

Gambacorta, L., Raguso, M. C., Mastrogiuseppe, M., & Seu, R. (2022). UWB processing applied to multifrequency radar sounders: The case of MARSIS and comparison with SHARAD. *IEEE Transactions on Geoscience and Remote Sensing*, *60*, 1–14. https://doi.org/10.1109/TGRS.2022.3216893

Giannakis, I., & Giannopoulos, A. (2014). A novel piecewise linear recursive convolution approach for dispersive media using the finite-difference time-domain method. *IEEE Transactions on Antennas and Propagation*, *62*(5), 2669–2678. https://doi.org/10.1109/TAP.2014.2308549

Hamran, S.-E., & Paige, D. A. (2021). Mars 2020 perseverance rover RIMFAX raw and calibrated data products [Dataset]. NASA PDS Geosciences Node. Retrieved from https://pds-geosciences.wustl.edu/missions/mars2020/rimfax.htm

Hamran, S.-E., Paige, D. A., Allwood, A., Amundsen, H. E. F., Berger, T., Brovoll, S., et al. (2022). Ground penetrating radar observations of subsurface structures in the floor of Jezero Crater, Mars. *Science Advances*, *8*(34), eabp8564. https://doi.org/10.1126/sciadv.abp8564

Hamran, S.-E., Paige, D. A., Amundsen, H. E., Berger, T., Brovoll, S., Carter, L., et al. (2020). Radar imager for Mars' subsurface experiment—RIMFAX. *Space Science Reviews*, *216*(8), 1–39. https://doi.org/10.1007/s11214-020-00740-4

Harbi, H., & McMechan, G. A. (2012). Conductivity and scattering q in GPR data: Example from the ellenburger dolomite, central Texas. *Geophysics*, *77*(4), H63–H78. https://doi.org/10.1190/geo2011-0337.1

Irving, J. D., & Knight, R. J. (2003). Removal of wavelet dispersion from ground-penetrating radar data. *Geophysics*, *68*(3), 960–970. https://doi.org/10.1190/1.1581068

Jonscher, A. K. (1977). The "universal" dielectric response. *Nature*, *267*(5613), 673–679. https://doi.org/10.1038/267673a0

Larsen Greiner, T. A., Hlebnikov, V., Lie, J. E., Kolbjørnsen, O., Kjelsrud Evensen, A., Harris Nilsen, E., et al. (2020). Cross-streamer wavefield reconstruction through wavelet domain learning. *Geophysics*, *85*(6), V457–V471. https://doi.org/10.1190/geo2019-0771.1

Lauro, S. E., Baniamerian, J., Cosciotti, B., Mattei, E., & Pettinelli, E. (2022). Loss tangent estimation from ground-penetrating radar data using Ricker wavelet centroid-frequency shift analysis. *Geophysics*, *87*(3), H1–H12. https://doi.org/10.1190/geo2021-0431.1

Madsen, M. B., Goetz, W., Bertelsen, P., Binau, C. S., Folkmann, F., Gunnlaugsson, H. P., et al. (2009). Overview of the magnetic properties experiments on the Mars exploration rovers. *Journal of Geophysical Research*, *114*(E6), E06S90. https://doi.org/10.1029/2002je002029

Olhoeft, G. R., & Strangway, D. (1975). Dielectric properties of the first 100 meters of the moon. *Earth and Planetary Science Letters*, *24*(3), 394–404. https://doi.org/10.1016/0012-821x(75)90146-6

Oudart, N., Ciarletti, V., Le Gall, A., Mastrogiuseppe, M., Hervé, Y., Benedix, W.-S., et al. (2021). Range resolution enhancement of wisdom/exomars radar soundings by the bandwidth extrapolation technique: Validation and application to field campaign measurements. *Planetary and Space Science*, *197*, 105173. https://doi.org/10.1016/j.pss.2021.105173

Quan, Y., & Harris, J. M. (1997). Seismic attenuation tomography using the frequency shift method. *Geophysics*, *62*(3), 895–905. https://doi.org/10.1190/1.1444197

Richards, P. G., & Aki, K. (1980). *Quantitative seismology: Theory and methods* (Vol. 859). Freeman.

Simon, M. N., Carter, L. M., Campbell, B. A., Phillips, R. J., & Mattei, S. (2014). Studies of lava flows in the THARSIS region of Mars using SHARAD. *Journal of Geophysical Research: Planets*, *119*(11), 2291–2299. https://doi.org/10.1002/2014je004666

Stillman, D. E., & Grimm, R. E. (2011). Radar penetrates only the youngest geological units on Mars. *Journal of Geophysical Research*, *116*(E3), E03001. https://doi.org/10.1029/2010je003661

Stillman, D. E., & Olhoeft, G. (2008). Frequency and temperature dependence in electromagnetic properties of Martian analog minerals. *Journal of Geophysical Research*, *113*(E9), E09005. https://doi.org/10.1029/2007je002977

Tonn, R. (1991). The determination of the seismic quality factor Q from VSP data: A comparison of different computational methods. *Geophysical Prospecting*, *39*(1), 1–27. https://doi.org/10.1111/j.1365-2478.1991.tb00298.x

Turner, G., & Siggins, A. F. (1994). Constant Q attenuation of subsurface radar pulses. *Geophysics*, *59*(8), 1192–1200. https://doi.org/10.1190/1.1443677

Ulaby, F. T., & Long, D. G. (2014). Microwave radar and radiometric remote sensing. (Vol. *4*). University of Michigan Press

Ulaby, F. T., Bengal, T. H., Dobson, M. C., East, J. R., Garvin, J. B., & Evans, D. L. (1990). Microwave dielectric properties of dry rocks. *IEEE Transactions on Geoscience and Remote Sensing*, *28*(3), 325–336. https://doi.org/10.1109/36.54359

Van Der Baan, M. (2001). Acoustic wave propagation in one dimensional random media: The wave localization approach. *Geophysical Journal International*, *145*(3), 631–646. https://doi.org/10.1046/j.1365-246x.2001.01405.x

Warren, C., Giannopoulos, A., & Giannakis, I. (2016). gprMax: Open source software to simulate electromagnetic wave propagation for Ground Penetrating Radar. *Computer Physics Communications*, *209*, 163–170. https://doi.org/10.1016/j.cpc.2016.08.020

Wiens, R. C., Udry, A., Beyssac, O., Quantin-Nataf, C., Mangold, N., Cousin, A., et al. (2022). Compositionally and density stratified igneous terrain in Jezero Crater, Mars. *Science Advances*, *8*(34), eabo3399. https://doi.org/10.1126/sciadv.abo3399

Paper IV

RIMFAX Dip Attribute Analysis: Unconformity Detection and True Dip in the Martian Subsurface

Sigurd Eide, Henning Dypvik, Hans Amundsen, David Page, and Svein-Erik Hamran

Published in *19th International Conference on Ground Penetrating Radar*, Society of Exploration Geophysicists, 2022, pp. 159–162. DOI: 10.1190/gpr2022-018.1.

An extract from a conference poster presentation is included in Appendix B and contains some extended results of this conference proceedings.

Appendices

Appendix A

BGS Groundhog Desktop GSIS as Model Builder for gprMax, for Assessment of Subsurface Hypotheses

A

Sigurd Eide

RIMFAX Science Team technical documentation, 2022.

BGS Groundhog Desktop GSIS as Model Builder for gprMax, for Assessment of Subsurface Hypotheses

An high-level demonstration is given of how to use the freeware software BGS Groundhog Desktop GSIS (Wood et al., 2015) to create subsurface models for importing into the open-source GPR simulation software gprMax (Warren et al., 2016). A description of how gprMax will need to be configured is also given. This description is a technical demonstration of the modeling presented in section 5.4 in Hamran et al. (2020) and the modeling workflow presented in Eide et al. (2021). Programming instructions are not included and scientific interpretation of results is not within the scope of this document.

Table of Contents

1. Groundhog Desktop data import 1
2. Digitize subsurface model 1
3. Gridding cross-section into dielectric model 6
4. Simulating soundings in subdomain along traverse 6
5. Assessing modeling results 6
6. References 9

1. Groundhog Desktop data import

Surface imagery, a digital terrain model (DTM) and shape file with rover navigation is imported into Groundhog and a cross-section is generated as a 2D plane along the rover navigation. Note that Groundhog do not use projections, so raster data and shape files need to be in the same projection before import.

The corresponding radargram can be imported as an image file (.PNG) and overlain the cross-section, Figure 1.

2. Digitize subsurface model

To assess a certain subsurface hypothesis, a model can be drawn along the cross-section for later import into gprMax. The model can e.g. be an interpretation based on the depth converted radargram and outcropping lithology as seen in the surface imagery. Linkage between positions in the map view and cross-section is enabled by Groundhog, enabling accurate location of e.g. outcrops in the subsurface model.

Here we want to study if the radargram can be an image of a cyclic step succession as proposed by Hamran et al. (2022), and described in Figure 2. This is one of several hypothesis that have been proposed, where the most supported interpretation has inferred an uplifted magmatic lithology (Farley et al., 2022). Nevertheless, based on the radargram image projected along the traverse and the cyclic steps schematic cartoon, we digitize geological layering along a selected distance of the sol 201-202 traverse.

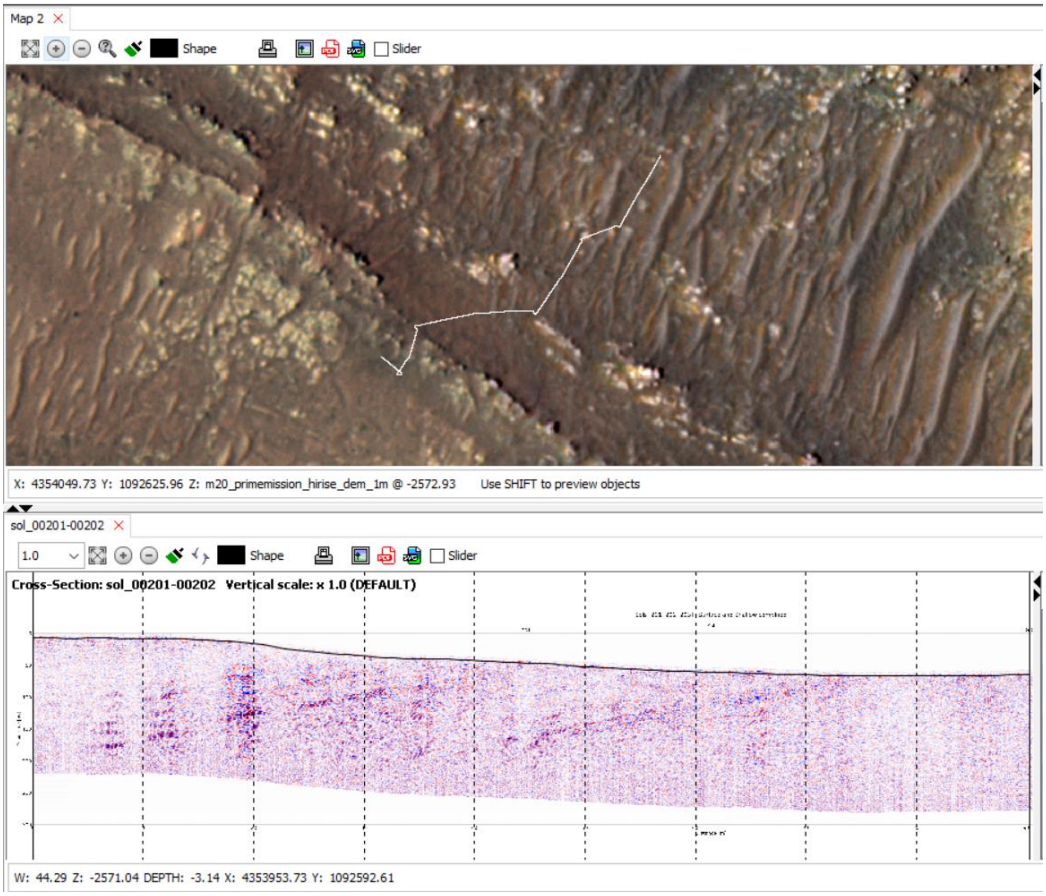

Figure 1: Groundhog view of 2D map with rover navigation from sol 201-202 and cross-section with radargram overlay. DTM has been used for terrain profile in cross-section (black line) and a topography-correction was applied the radargam before import. The depth relationship in the radargram is set according to a constant subsurface velocity (0.1 m/ns).

2.1. Geological layering

Drawn lines define the top geological horizons and are identified by numeric values and a text description. The numeric value will later be used as identifiers for the dielectric properties of that layer.

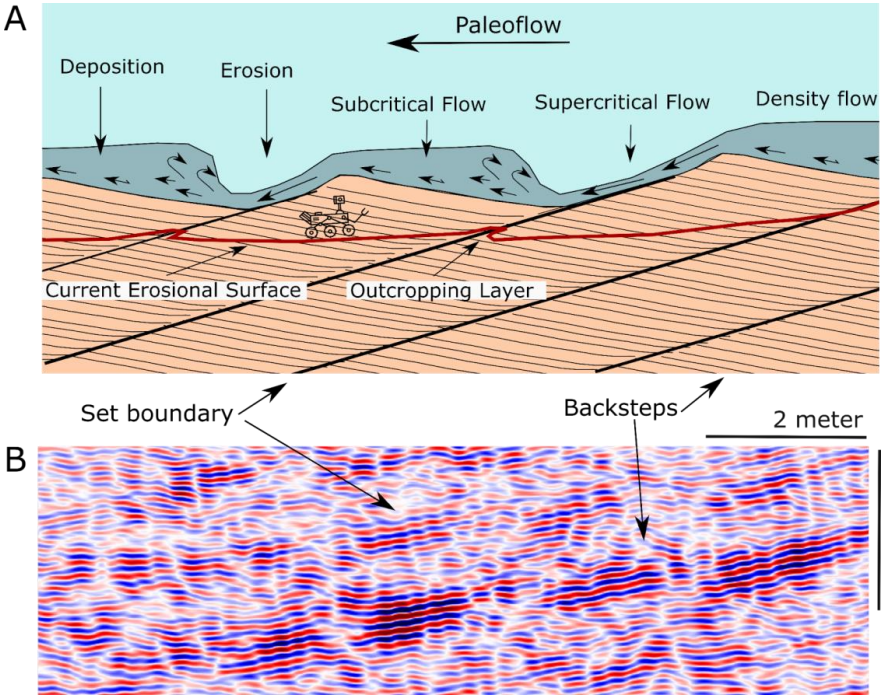

Figure 2: (A) Notional cross-sectional illustration of the formation mechanism for the cyclic step structures observed during the Sol 201-202 traverse. (B) RIMFAX radar image of subsurface cyclic step structures observed at 2-6 meters depth. Figure from Hamran et al. (2022).

The radargram is used as a model to get the large scale geometry similar to the measured RIMFAX data, but drawn layers are a simplified and schematic representation of a cyclic-steps succession. Making a detailed subsurface model based on the reflections in a radargram can be challenging due to a dominance of incoherent and complicated reflection patterns. Nevertheless, interpretation on the radargram should preferably be done on a migrated and depth-converted radargram, in order to correctly represent subsurface geometry. The digitized subsurface model has layering down to ~5 m depth and is presented in Figure 4.

Then the cross-section is exported to file in GOCAD Pline format:

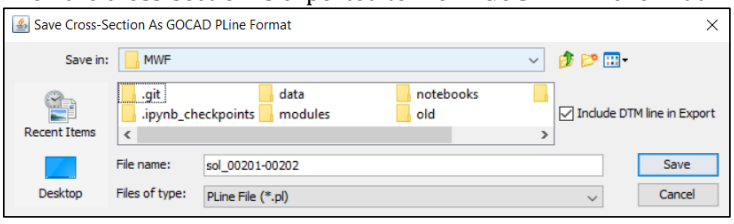

Figure 3: Exporting cross-section from Groundhog.

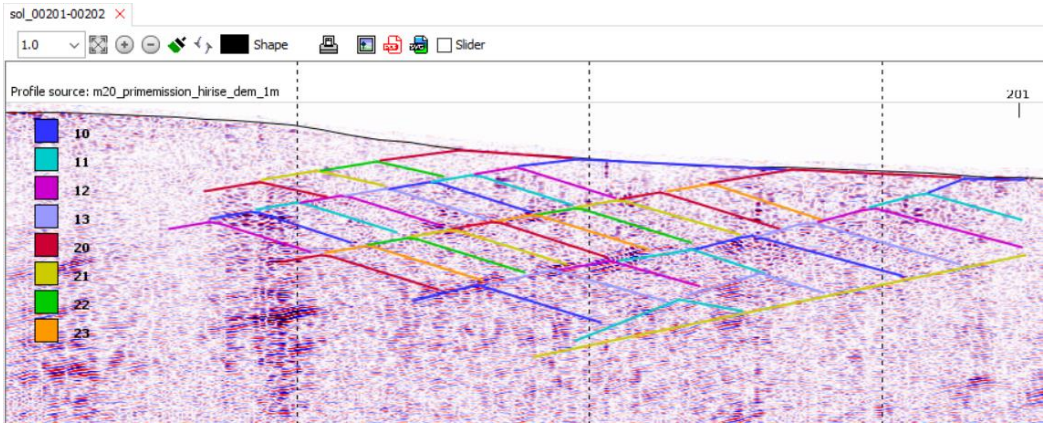

Figure 4: Digitized geological layering along selected part of the traverse, based on schematic model of cyclic steps and reflection geometry in radargram. Digitized lines indicate top horizons.

2.2. Dielectric material file in gprMax

Each geologic unit in the cross-section needs to be related to a material in gprMax, where the dielectric properties are described. This is done through the name of the units set to be a unique integer value. The materials are defined in a text file as described in:
http://docs.gprmax.com/en/latest/input.html#material
http://docs.gprmax.com/en/latest/input.html#geometry-objects-read

An example of material properties for the cross-section, where the average velocity of all layers are 0.1 m/ns (ε'=9), with layers 10-13 and 20-23 are ordered in groups of lower and higher permittivities:

	A	B	C	D	E	F
1	#material:	1	0	1	0	0_nan
2	#material:	1	0	1	0	1_nan
3	#material:	1	0	1	0	2_nan
4	#material:	1	0	1	0	3_nan
5	#material:	1	0	1	0	4_nan
6	#material:	1	0	1	0	5_nan
7	#material:	1	0	1	0	6_nan
8	#material:	1	0	1	0	7_nan
9	#material:	1	0	1	0	8_nan
10	#material:	1	0	1	0	9_nan
11	#material:	8.4	0	1	0	10_A0
12	#material:	8.5	0	1	0	11_A1

	A	B	C	D	E	F
13	#material:	8.6	0	1	0	12_A2
14	#material:	8.7	0	1	0	13_A3
15	#material:	1	0	1	0	14_nan
16	#material:	1	0	1	0	15_nan
17	#material:	1	0	1	0	16_nan
18	#material:	1	0	1	0	17_nan
19	#material:	1	0	1	0	18_nan
20	#material:	1	0	1	0	19_nan
21	#material:	9.3	0	1	0	20_B0
22	#material:	9.4	0	1	0	21_B1
23	#material:	9.5	0	1	0	22_B2
24	#material:	9.6	0	1	0	23_B3

Figure 5: Material properties of each geological unit in cross-section.

Materials can also be defined as complex dielectric models as in Eide et al. (2022), using e.g. Cole-Cole parametrization approximated by a multi-pole Debye formulation (Giannakis et al., 2012).

2.3. Fractal surface roughness

Surface roughness can be applied the top surface of any geologic unit in the model by filling out a configuration file:

#COLLUMNS:	ID	FDIMENSION	WEIGHT_X	WEIGHT_Y	RANGE_LO	RANGE_UP	NAME
	0	1	1	1	0	0	0_nan
	1	1	1	1	0	0	1_nan
	2	1	1	1	0	0	2_nan
	3	1	1	1	0	0	3_nan
	4	1	1	1	0	0	4_nan
	5	1	1	1	0	0	5_nan
	6	1	1	1	0	0	6_nan
	7	1	1	1	0	0	7_nan
	8	1	1	1	0	0	8_nan
	9	1	1	1	0	0	9_nan
	10	2.1	1	1	-0.2	0.2	10_sr
	11	1	1	1	0	0	11_nan
	12	1	1	1	0	0	12_nan

roughsurface_config

Figure 6: Configuration file for assigning surface roughness to layers in cross-section. For example, here layer with ID 10 has been assigned a fractal dimension of 2.1; weighting in x (inline) and y (crossline) directions are 1 and 1; and the maximum vertical displacement is constrained to -0.2 and 0.2 m. The "NAME" column is only for user convenience.

2.4. Scattering inhomogeneities

Scattering inhomogeneities are ellipsoids of varying size placed randomly within the volume of a geological unit. Inhomogeneities can be applied of any unit in the cross-section model by filling out a configuration file:

#COLLUMNS:	ID	ID_INCL1	ID_INCL2	PREC_INCL1	PREC_INCL2	SIZEMAX_INCL1	SIZEMAX_INCL2	NAME
	0	0	0	0	0	0	0	0_nan
	1	1	1	0	0	0	0	1_nan
	2	2	2	0	0	0	0	2_nan
	3	3	3	0	0	0	0	3_nan
	4	4	4	0	0	0	0	4_nan
	5	5	5	0	0	0	0	5_nan
	6	6	6	0	0	0	0	6_nan
	7	7	7	0	0	0	0	7_nan
	8	8	8	0	0	0	0	8_nan
	9	9	9	0	0	0	0	9_nan
	10	11	12	0.1	0.05	0.1	0.2	10_rs_inh
	11	11	11	0	0	0	0	11_nan
	12	12	12	0	0	0	0	12_nan

inhomogeneties_config

Figure 7: Configuration file for assigning scattering inhomogeneities to geologic units in cross-section. For example, here layer with ID 10 has been assigned 10% inhomogeneities from geologic unit 11 and 5% inhomogeneities from geologic unit 12. Max diameter size is set to 0.1 and 0.2 m, respectively. The "NAME" column is only for user convenience.

2.5. Fractal inhomogeneous media

To be implemented.

3. Gridding cross-section into dielectric model

The cross-section can then be read into gprMax by the python module in the input file (.in): http://docs.gprmax.com/en/latest/python_scripting.html#scripting-the-input-file.

However, python scripts for how to read the GOCAD Pline file and corresponding configuration files, are not included in this documentation.

Certain parameters are nevertheless essential during generation of the gprMax input file:

- Start and stop distances along cross-section, defining along track length of total simulation.
- Along track sounding step distance, if not read from shape file.
- Dimensions of subdomain, within where single soundings are calculated (see Section 4).
- Grid increment (Yee cell size) in x, y and z direction.
- DTM used to cap cross-section at the surface. If not given, cross-section topography is used.
- Recording time in ns.
- Antenna height above ground.

Simulations can be done in 2D or 2.5D. For a 2.5D model, each top horizon digitized in the 2D cross-sectional model in Figure 4, the horizon is extrapolated in cross-track direction to create a 2.5D model.

Other specifications relevant for GPR modeling that is not essential or constructing the subsurface model, e.g. antenna model and waveform, are not within the scope if this documentation.

4. Simulating soundings in subdomain along traverse

As the finite-difference time-domain scheme employed in gprMax is computational demanding, each sounding along the rover acquisition line is computed within a subdomain of the cross-section. That is, for each time the gprMax input file is executed, an individual model will be gridded around the specific sounding location. This is illustrated in Figure 8 for three separate soundings over the cross-section subsurface model.

5. Assessing modeling results

Having computed soundings every 0.1 m along the cross-section, a radargram is generated by adding all together side by side. In Figure 9 the result is displayed after having subtracted source effects and ringing as in Eide et al. (2022). In Figure 9 - Figure 11 are the results from a plane subsurface model, subsurface model with surface roughness, and subsurface model with surface roughness and scattering inhomogeneities, respectively.

This is a demonstration of the software workflow, consequently the subsurface model is fairly simplistic, as reflected in the synthetic radargram. However, this is the starting point for assessing the subsurface hypothesis, and –if probable–what the fine detailed structures and properties are, e.g. layering thickness, orientation, dielectric values, amount of surface roughness, and inhomogeneities.

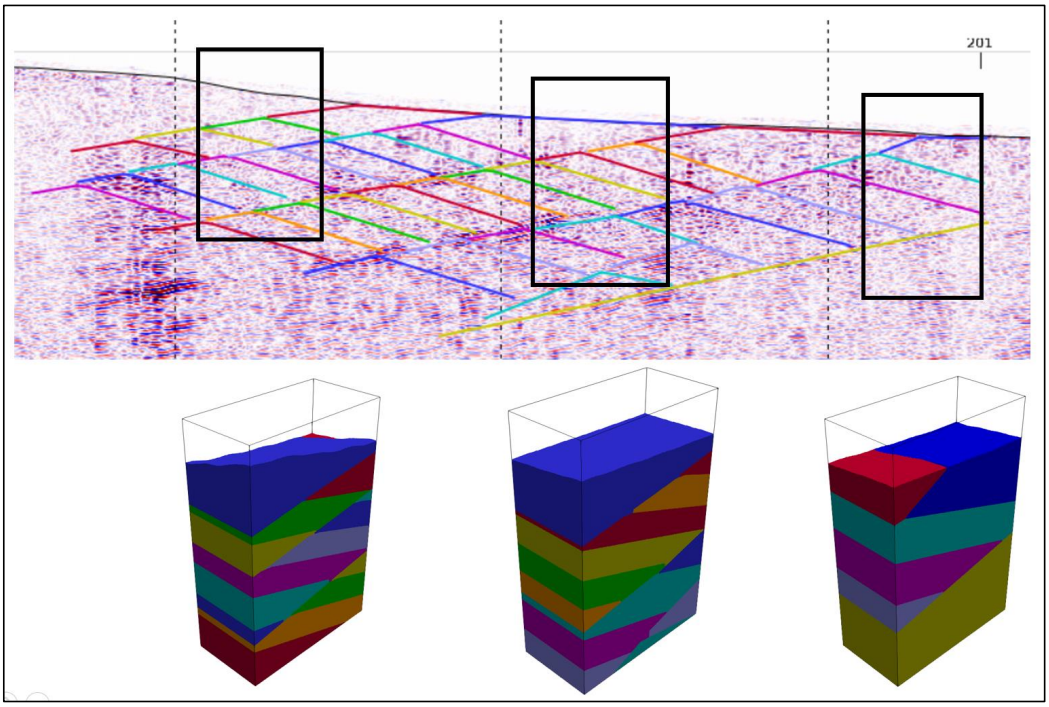

Figure 8: Illustration of subdomain gridding along the cross-section. In this example subdomains have dimensions x=4m, y=2m and z=6m. Along-track is x-direction and cross-track is y-direction. Surface is capped according to DTM.

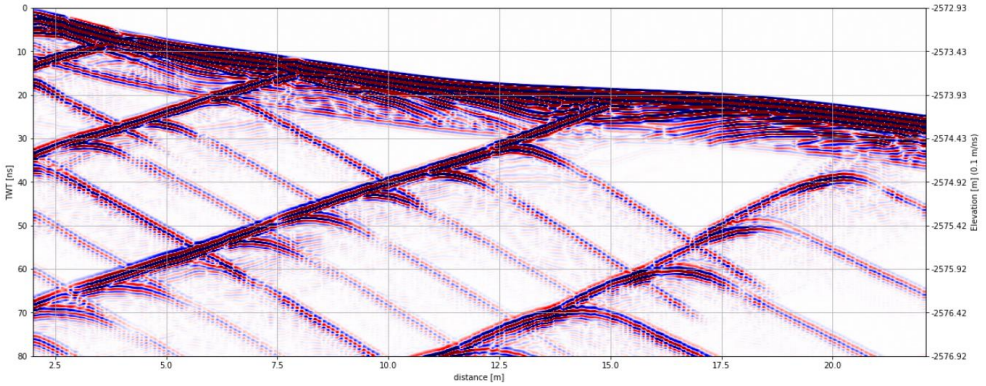

Figure 9: Synthetic radargram from simulation over a plane model.

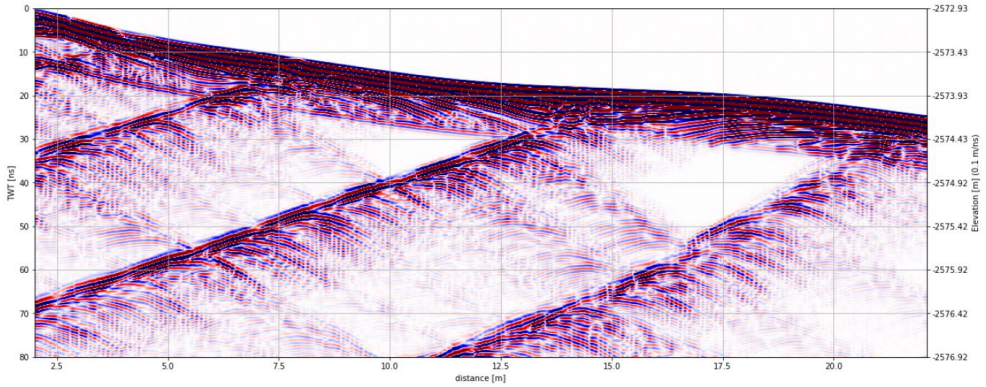

Figure 10: Synthetic radargram from simulation with surface roughness.

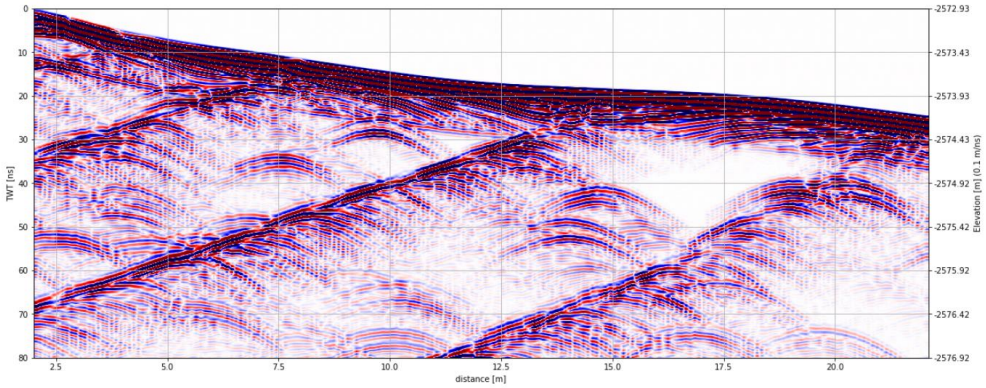

Figure 11: Synthetic radargram from simulation with surface roughness and scattering inhomogeneities.

6. References

Eide, S., Casademont, T., Aardal, Ø. L., & Hamran, S.-E. (2022). Modeling FMCW Radar for Subsurface Analysis. *IEEE Journal of Selected Topics in Applied Earth Observations and Remote Sensing, 15*, 2998-3007.

Eide, S., Hamran, S.-E., Dypvik, H., & Amundsen, H. E. (2021). Ground-penetrating radar modeling across the Jezero crater floor. *IEEE Journal of Selected Topics in Applied Earth Observations and Remote Sensing, 14*, 2484-2493.

Farley, K., Stack, K., Shuster, D., Horgan, B., Hurowitz, J., Tarnas, J., et al. (2022). Aqueously altered igneous rocks sampled on the floor of Jezero crater, Mars. *Science, 377*(6614), eabo2196.

Giannakis, I., Giannopoulos, A., & Davidson, N. (2012, 4-8 June 2012). *Incorporating dispersive electrical properties in FDTD GPR models using a general Cole-Cole dispersion function.* Paper presented at the 2012 14th International Conference on Ground Penetrating Radar (GPR).

Hamran, S.-E., Paige, D. A., Allwood, A., Amundsen, H. E., Berger, T., Brovoll, S., et al. (2022). Ground penetrating radar observations of subsurface structures in the floor of Jezero crater, Mars. *Science Advances, 8*(34), eabp8564.

Hamran, S.-E., Paige, D. A., Amundsen, H. E. F., Berger, T., Brovoll, S., Carter, L., et al. (2020). Radar Imager for Mars' Subsurface Experiment—RIMFAX. *Space Science Reviews, 216*(8), 128. https://doi.org/10.1007/s11214-020-00740-4

Warren, C., Giannopoulos, A., & Giannakis, I. (2016). gprMax: Open source software to simulate electromagnetic wave propagation for Ground Penetrating Radar. *Computer Physics Communications, 209*, 163-170. http://www.sciencedirect.com/science/article/pii/S0010465516302533

Wood, B., Richmond, T., Richardson, J., & Howcroft, J. (2015). BGS Groundhog® desktop Geoscientific Information System external user manual.

Appendix B

RIMFAX Dip Attribute Analysis: Extended Results

Sigurd Eide, Henning Dypvik, Hans Amundsen, David Page, and Svein-Erik Hamran

Extract from poster presentation during *SEG 19th International Conference on Ground Penetrating Radar*, Golden, CO, June 2022.

This appendix includes extended results to the conference proceedings in Paper IV. The results were presented in a poster session during the SEG 19th International Conference on GPR.

RIMFAX dip attribute analysis results:
Unconformity detection and true dip in the Martian subsurface

Sigurd Eide[1] (sigurd.eide@its.uio.no), Henning Dypvik[1], Hans E.F. Amundsen[1], David Page[2], Svein-Erik Hamran[1]
[1]Center for Space Systems and Sensors, Institute of Technology Systems, University of Oslo, Norway [2]University of California, Los Angeles, USA

UiO : University of Oslo